ACHIEVING HUNDREDS-METER RANGES IN LOW POWERED RFID SYSTEMS WITH QUANTUM TUNNELING TAGS

A Dissertation
Presented to
The Academic Faculty

By

Francesco Amato

In Partial Fulfillment
of the Requirements for the Degree
Doctor of Philosophy in the
School of Electrical and Computer Engineering

Georgia Institute of Technology

May 2017

ACHIEVING HUNDREDS-METER RANGES IN LOW POWERED RFID SYSTEMS WITH QUANTUM TUNNELING TAGS

Approved by:

Prof. Gregory D. Durgin, Advisor
School of Electrical and Computer Engineering
Georgia Institute of Technology

Prof. Andrew F. Peterson
School of Electrical and Computer Engineering
Georgia Institute of Technology

Prof. John D. Cressler
School of Electrical and Computer Engineering
Georgia Institute of Technology

Prof. Mary Ann Weitnauer
School of Electrical and Computer Engineering
Georgia Institute of Technology

Prof. Gaetano Marrocco
Dipartimento di Ingegneria Civile e Ingegneria Informatica
University of Roma Tor Vergata

Date Approved: January 11, 2017

In memory of Rodney James Sabatini

ACKNOWLEDGEMENTS

This thesis represents the final destination of a journey started in the United States some years ago.

I want to thank my advisor, Prof. Gregory Durgin for welcoming me into his group and for following me throughout my research path. He patiently allowed me to explore and learn from my mistakes. Thanks to him, I improved day by day my skills as a researcher, as an engineer, and as a mentor.

I am grateful to my committee members Prof. John Cressler, Prof. Gaetano Marrocco, Prof. Andrew Peterson, and Prof. Mary Ann Weitnauer for their time, helpful comments, and valuable feedback.

Many of the results and breakthroughs of this thesis would have not been possible without the support of brilliant colleagues: thanks to Christopher Peterson and Hakki Torun for their help in running many of the experiments in this work. Thanks to Dr. Redwan Noor Sajjad and Dr. Brian Degnan for the interesting conversations on tunnel diodes. Without my colleagues from the Propagation Group, no insightful comments would have ever enriched my thoughts: thanks to those that welcomed me with great enthusiasm to the lab (Blake Marshall, Marcin Morys, Bashir Akbar, Chris Valenta, Albert Lu and Raj Bhattacharjea) and thanks to the new members (Mohammad Al-Hassoun, Cheng Qi, Sang Kyu Kim and Qian Yang) for their friendship and for sharing this time together. Thanks to Jackson and Holly McCormick, Nick Gross, Marc Higginson-Rollins, Nathan Opalinski and Amedeo Bellotti for their friendship and support.

If I could focus and advance in my work it is only thanks to the great ECE staff: thanks to James Steinberg and Kevin Pham, always cheerful and welcoming, to Tasha Torrence, Sharon Pugh and all the staff of the Graduate Affairs Office for their advices and patience. Thanks to Siri Micolte to let me use her apartment to run my transmission experiments. Thank you Daniela Staiculescu for being always on my side.

To all the Teachers and Professors that I encountered throughout my studies, thanks for providing me with the right tools to help me understand and analyze the world around me. Thanks to Joyelle Harris, Jill Auerbach, Julie Ridings, Donna Llewellyn, Diley Hernandez, Analia Rao and Julie Fritz, fantastic mentors in Atlanta. All the hard work that you do for the young generations deserve more than gratitude and admiration.

Thanks to all my friends I started and shared this adventure with: Sean Rodrigues, Jacques Florence, Joshua Mendez, Hansel Enriquez, Giancarlo Nino, and Taoran Le. Things would have been much harder and less fun without all of you!

And last, but not least, thanks to my parents Nicola and Bruna and to my sister Donatella for supporting all my decisions and for making my *goodbyes* sound always like an adventure and never like a burden.

TABLE OF CONTENTS

Acknowledgments v

List of Tables xi

List of Figures xiii

List of Abbreviations and Symbols xix

Chapter 1: Introduction 1

1.1 Document Organization 3

Chapter 2: Enhancing the Backscatter-Radio Link 5

2.1 Background 5

2.2 Backscatter-Radio Link Budget 6

2.2.1 Modulation Factor 8

2.3 Enhancing the Backscatter-Radio Link 10

Chapter 3: Active Loads for Low-powered Backscattering Links 13

3.1 Electronic Devices for Backscattering Applications 13

3.2 Two-terminal Active Devices 14

3.3 Tunnel Diodes and the Tunneling Effect 15

3.3.1 Tunneling Probability and Current 19

3.4 Reflection Amplifiers for Backscattering Applications 20
3.4.1 State-of-the-art 22
3.5 The Quantum Tunneling Reflector 26
3.6 Chapter Conclusions 27

Chapter 4: The Quantum Tunneling Reflector 29

4.1 Oscillators 30
4.2 A Quantum Tunneling Reflector (QTR) - Fabrication 30
4.2.1 Device Characterization 31
4.2.2 Circuit Design 31
4.2.3 Board Assembly 33
4.3 Quantum Tunneling Reflector (QTR) - Testing 34
4.3.1 Experimental Setup 34
4.3.2 Experimental Results 35
4.4 Testing Procedure for QTR Characterization 41
4.5 Modulation Tests 43
4.6 Achievable Wireless Ranges 45
4.7 Chapter Conclusions 47

Chapter 5: Signal-to-Noise Ratio of the Quantum Tunneling Reflector 48

5.1 Oscillations and Locking 49
5.2 Measuring the SNR of the QTR 50
5.2.1 Biasing 51
5.2.2 External Signal Strength 54

5.2.3 Effects of Modulation 55
5.2.4 Effects of an Interfering Signal 58
5.2.5 Power Consumption 60
5.3 Chapter Conclusions 61

Chapter 6: Beyond the limits of Classic Backscattering Communications 63
6.1 Preliminary Backscattering Tests 63
6.2 Mapping the Scattered Electric Field 64
6.3 The Experimental Setup 67
6.3.1 The Microwave Transceiver 68
6.3.2 The Quantum Tunneling Tag - QTT 68
6.3.3 Instrument Calibration 69
6.3.4 The Field Test Campaign 70
6.4 Achieved Ranges and Gains of the Quantum Tunneling Tag 70
6.5 Gain Model Validation and Modulation Errors 76
6.6 A Link Budget Designer Tool 78
6.6.1 Testing Scenarios 81
6.6.2 Long Range Backscattering - Bistatic Configuration 82
6.6.3 Long Range Backscattering - Monostatic Configuration 83
6.7 Considerations on Power Consumption 88
6.8 Chapter Conclusions 89

Chapter 7: Conclusion and future work 90
7.1 Major Contributions 90

7.2 Future Work 92
7.3 Publications and Presentations 92
7.3.1 Journals 93
7.3.2 Book Chapter 93
7.3.3 Conference Papers and Presentations 93
7.3.4 Poster Presentations 95
7.3.5 Master Thesis 95
7.3.6 Technical Reports 95

Appendix A: Content of the Github Repository 97

Appendix B: Magnetron 99

B.1 Magnetron Transmitter for Backscattering Applications 99
B.1.1 The CM358F 101
B.1.2 The Filament Transformer 101
B.1.3 The Magnetron Head 102
B.1.4 The Control Box 102
B.1.5 The Circuit Breaker 103
B.2 Regulatory Considerations 103

References 111

Vita 112

LIST OF TABLES

3.1 Overview of reflection amplifiers available in literature. 24

3.2 Details on reflection amplifier technologies listed in Table 3.1. 25

4.1 Encoded one-byte word. 44

5.1 Variables and constants of a modulated backscatter link 50

5.2 Summary of 5.8 GHz free space link budgets in various basckscattering systems 51

5.3 Bias V_{DC} = 55.0 mV, f_m = 250 kHz 56

5.4 Bias V_{DC} = 57.5 mV, f_m = 250 kHz 56

5.5 Bias V_{DC} = 60.0 mV, f_m = 250 kHz 56

5.6 Bias V_{DC} = 62.5 mV, f_m = 250 kHz 57

5.7 Bias V_{DC} = 65.0 mV, f_m = 250 kHz 57

6.1 Configurations of the Experimental Setups 70

6.2 Field campaign measurements spots. 71

6.3 Measured received powers and gains 75

6.4 Comparing gains: measures *vs* modeling 78

6.5 System variables of a backscattering communication link 81

6.6 IoT scenarios for free space long range backscattering applications 82

6.7 Required system parameters for the scenarios listed in Table 6.6 when using a 5.8 GHz co-located bistatic transceiver 83

6.8 Required system parameters for the scenarios listed in Table 6.6 when using a 5.8 GHz monostatic transceiver 86

B.1 CM358F parameters 102

LIST OF FIGURES

2.1 Conceptual schematic of a bistatic backscatter modulation link 6

2.2 A Smith Chart showing four possible solutions to implement a backscatter-radio link. 10

2.3 Forward and return links of a) 915 MHz and b) 5.8 GHz RFID passive system. P_T = 30 dBm, $G_{tx} = G_{rx}$ = 6 dBi, G_t = 0 dBi, M = -6 dB (0.25). The horizontal lines represent respectively the maximum tag and reader sensitivities ($P_{t_{min}}$ and $P_{R_{min}}$) [14, 24] currently available. 12

3.1 Degenerate semiconductors. 16

3.2 The tunneling effect. 18

3.3 Example I-V characteristic of a tunnel diode. 19

3.4 Equivalent circuit of a reflection amplifier. 21

3.5 State-of-the-art of reflection amplifiers. Comparisons of return gains and required biasing DC powers. An earlier version of this plot is published in [45]. 25

3.6 Data from Table 3.1 show a decreasing power consumption of reflection amplifiers in recent years; tunnel diode-based reflectors lead the trend. . . . 27

3.7 Block diagram of a quantum tunneling RFID tag. 28

4.1 I-V characteristics for an ideal tunnel diode, used for illustration purposes; the measured MBD5057-E28 diode at 300 K; and the model used for simulations. 32

4.2 Circuit schematic of a quantum tunneling reflector (QTR) with an open circuit tuning stub at short distance (ϵ) from the diode; the equivalent circuit of the tunnel diode is highlighted: C_j = 0.03 pF is the internal junction capacitance, C_p = 0.8 pF and L_p = 0.4 nH are the packaging parasitics and r = 0 Ω is the negligible linear resistance; a voltage controlled source, G, models the nonlinear junction resistance through Eq. 4.3. 33

4.3 Microstrip line structure of the fabricated quantum tunneling reflector (QTR): the tuning stub is 100 mils (2.54 mm) long and 10 mils (0.254 mm) wide. Its exposed trace, not covered with silkscreen, can be used for tuning purposes, if necessary. A capacitor C_1 of 1.5 pF has been used as DC block. Two identical boards have been used to test two MBD5057-E28 tunnel diodes (#1 and #2). 34

4.4 Setups used to collect experimental data. a) reflection measurements on VNA E5071B with avg. 16. b) Reflection measurements with circulator, signal generator E8247C and signal analyzer CXA-N9000A. Signal analyzer setup: resolution BW 3 kHz, video BW 100 kHz, avg. 10, span 1 MHz. 35

4.5 S-parameter sweeps for QTRs mounting a) tunnel diode #1 and b) tunnel diode #2 at different biasing levels. RF signal input power P_{in} = -50 dBm. . 37

4.6 S-parameter phase sweeps for the two QTRs when no bias or optimal bias are applied. RF signal input power P_{in} = -50 dBm. 38

4.7 Reflection coefficients Γ (real and imaginary components) of the RF signal output for different biasing voltages (in mV); the unitary circle is highlighted. RF signal input power P_{in} = -50 dBm, RF input frequency: 5.8 GHz. Experiments done with a) tunnel diode #1 and b) tunnel diode #2. . . 39

4.8 Reflection coefficients Γ (real and imaginary components) of the RF signal output for different input frequencies (in GHz) spanning in the 5.8 GHz band (5.725 GHz to 5.875 GHz); the unitary circle is highlighted. RF signal input power P_{in} = -50 dBm. Experiments done with a) tunnel diode #1 biased at 90 mV and b) tunnel diode #2 biased at 110 mV. 40

4.9 QTR gains, G_{QTR}, as function of the RF input power at 5.8 GHz. Tunnel Diode #1: V_{bias} = 90 mV, I_{bias} = 500 μA, P_{bias} = 45 μW. Tunnel Diode #2: V_{bias} = 110 mV, I_{bias} = 354 μA, P_{bias} = 39 μW. The measured gains are compared with simulation results. 41

4.10 Measured impedance of the two reflection amplifiers for variable RF input powers at 5.8 GHz, when optimum biases are applied. 42

4.11 QTR gains, G_{QTR}, as function of input frequency. Tunnel Diode #1: RF input power P_{in} = -75 dBm, V_{bias} = 90 mV. Tunnel Diode #2: RF input power P_{in} = -84 dBm, V_{bias} = 110 mV. 42

4.12 QTR gains, G_{QTR}, as function of the V_{bias} for RF input at 5.8 GHz. Tunnel Diode #1: RF input power P_{in} = -75 dBm; tunnel Diode #2: RF input power P_{in} = -84 dBm. 43

4.13 Comparing modulating and amplifying capabilities of the QTR prototype #1 with a semi-passive tag when a low RF power input (P_{in} = -55 dBm) is injected. Carrier at 5.8 GHz, fundamental frequency at 250 kHz away from it, and harmonics are shown. 44

4.14 Measure of the time-domain base-band signal resulting from the 0xA4 word modulated with Manchester encoding, reflected by QTR #1 and directly sent into the RF receiver. The QTR RF input power is P_{in} = -55 dBm. 45

4.15 RFID link budget analysis: P_T = 30 dBm, $G_{tx} = G_{rx} = G_t$ = 6 dBi, f_{in} = 5.8 GHz. The return gains from Fig. 4.9 have been used as the quantum tunneling reflector gain G_{QTR}. The 6 dB shift between the ideal passive and the semi-passive tags is due to the different modulation factor M; the different slope of the quantum tunneling tag link budget is due to the dependence of G_{QTR} on the RF power level P_t impinging on the tag. At low impinging power levels, the QTT prototype achieves one order of magnitude higher ranges than ideal passive and semi-passive tags. 46

5.1 Experimental setup: signal generator E8247C, signal analyzer CXA-N9000A with noise figure of 75 dB at 3 kHz resolution bandwidth; 100 kHz video bandwidth; center frequency 5.8 GHz and 100 MHz span on 1001 points. Although the noise figure of the signal analyzer is high, it is overshadowed by the noise introduced through biasing of the tunneling reflector. 52

5.2 Effect of biases on the quantum tunneling reflector recorded over a span of 100 MHz around 5.8 GHz when no RF input is applied. 53

5.3 Locking of the quantum tunneling reflector for f_{in} = 5.8 GHz, P_t = -55 dBm, f_m = 250 kHz and V_{DC} = 60.0 mV. 53

5.4 Locking of the quantum tunneling reflector for f_{in} = 5.8 GHz, P_t = -55 dBm, f_m = 250 kHz and V_{DC} = 62.5 mV. 54

5.5 Spectrum of 1 millisecond measurement on the in-phase channel of a 5.8 GHz backscattering transceiver. The transmitter is directly connected to the tunneling reflector. 55

5.6 SNR as function of the external locking signal P_t for different bias voltages. Best SNRs are obtained for input power levels above -65 dBm at bias levels of 60.0 mV and 62.5 mV. 58

5.7 Locking of the quantum tunneling reflector for f_{in} = 5.8 GHz, P_t = -55 dBm, f_m = 5 MHz and V_{DC} = 60.0 mV 59

5.8 Locking of the quantum tunneling reflector for f_{in} = 5.8 GHz, P_t = -55 dBm, f_m = 7 MHz and V_{DC} = 60.0 mV 59

5.9 Effect of an interferer at 5.799 GHz with same amplitude of the main signal: P_t = -61 dBm. 60

5.10 Effect of an interferer at 5.799 GHz and -81 dBm amplitude. 61

6.1 Experimental setup to test the wireless capabilities of a quantum tunneling tag. P_T = -20 dBm, $G_{tx} = G_t$ = 6 dBi, G_{rx} = 12 dBi, G_{amp} = 30 dB, r = 23 m, f_m = 250 kHz. 64

6.2 Signal backscattered by the quantum tunneling RFID tag and observed at the reader ($r = 23$ m). When the tunnel diode is biased with a 250 kHz square wave ($V_{pp} = 69mV$), peaks at 250 kHz away from the carrier frequency are observed. Other frequencies from other surrounding signals are present when the modulation is turned both ON and OFF. 65

6.3 Transceiver [18] and tag configuration used to collect the experimental data. Details are listed in Table 6.1. Data are acquired thought the GNU radio interface, saved as **.bin* files and available at [67]. 67

6.4 Satellite view of the Georgia Tech campus and the Midtown neighborhood in Atlanta, GA showing locations and distances covered during the field measurement campaign conducted and described in this work. 71

6.5 Experimental setup locations to test long distance capabilities of the quantum tunneling tag. a) Van Leer; b) Tech Green; c) parking lot of the Georgia Tech Professional Education (GTPE). 72

6.6 IQ diagrams for the received base-band backscattered signals on Setup I. V_{pp} = 60 mV, f_m = 250 kHz, r = 25 and 45 m. 74

6.7 IQ diagrams for the received base-band backscattered signals on Setup I. V_{pp} = 60 mV, f_m = 250 kHz, r = 100 and 160 m. 74

6.8 IQ diagrams for the received base-band backscattered signals on Setup I. V_{pp} = 60 mV, f_m = 1 MHz, r = 25, 45 and 160 m. 75

6.9 Received signal strengths $\widetilde{P}_r$ as function of distances r, biasing voltages V_{pp} and modulation speeds f_m using Setup I (6 dBm EIRP). Results are compared with an ideal semi-passive link (M = 1 and no quantum tunneling reflector) using the same configurations as in Setup I. 76

6.10 Comparing the measured quantum tunneling reflector gains, $\widetilde{G}_{QTR}$, with the gain model G_{QTR} expressed through Eq. 6.11 (valid for RF power on tag values P_t ranging between -80 dBm and -55 dBm). 77

6.11 IQ diagrams for the received base-band backscattered signals on Setup II. V_{pp} = 60 mV, r = 650 m. a) f_m = 250 kHz; b) f_m = 1 MHz. 79

6.12 IQ diagrams for the received base-band backscattered signals on Setup III. V_{pp} = 60 mV, r = 1200 m. a) f_m = 1 MHz; b) f_m = 1.77 MHz. 80

6.13 Modulation Error Ratios (MER) for each test of the measurement campaign. 81

6.14 Comparing a 5.8 GHz backscattering link of 50 meter radius when an ideal semi-passive (M = 1) and a quantum tunneling tag ($M = G_{QTR}$) are used. Bistatic configuration, free space, and a -110 dBm receiving sensitivity are assumed. 84

6.15 Comparing a 5.8 GHz backscattering link of 700 meter radius when an ideal semi-passive (M = 1) and a quantum tunneling tag ($M = G_{QTR}$) are used. Bistatic configuration, free space, and a -110 dBm receiving sensitivity are assumed. 84

6.16 Comparing a 5.8 GHz backscattering link of 2000 meter radius when an ideal semi-passive (M = 1) and a quantum tunneling tag ($M = G_{QTR}$) are used. Bistatic configuration, free space, and a -110 dBm receiving sensitivity are assumed. 85

6.17 Whole coverage of different scenarios for the bistatic case, assuming free space and a -110 dBm receiving sensitivity. 85

6.18 Comparing a 5.8 GHz backscattering link of 50 meter radius when an ideal semi-passive (M = 1) and a quantum tunneling tag ($M = G_{QTR}$) are used. Monostatic configuration, free space, and a -110 dBm receiving sensitivity are assumed. 86

6.19 Comparing a 5.8 GHz backscattering link of 700 meter radius when an ideal semi-passive (M = 1) and a quantum tunneling tag ($M = G_{QTR}$) are used. Monostatic configuration, free space, and a -110 dBm receiving sensitivity are assumed. 87

6.20 Comparing a 5.8 GHz backscattering link of 2000 meter radius when an ideal semi-passive (M = 1) and a quantum tunneling tag ($M = G_{QTR}$) are used. Monostatic configuration, free space, and a -110 dBm receiving sensitivity are assumed. 87

6.21 Whole coverage of different scenarios for the monostatic case, assuming free space and a -110 dBm receiving sensitivity. 88

B.1 The high power 5.8 GHz magnetron system. 100

B.2 a) the filament transformer and the fast-on connectors; b) the circuit breaker. 104

LIST OF ABBREVIATIONS AND SYMBOLS

$2\Delta f$ Locking range

$\Delta\sigma_{RCS}$ Differential Radar Cross Section

ϵ_r Relative permittivity

Γ^* Conjugate reflection coefficient

$\hbar$ Reduced Planck constant

λ Signal wavelength

$\mathcal{E}$ Electric field

σ_{RCS} Radar Cross Section

$\tan\delta$ Loss tangent

A_s Structural component

E Total Energy

e Average error

E_G Semiconductor band-gap

E_x Energy in the tunneling direction

$E_\perp$ Transverse energy

f Signal frequency

f_C Fermi-Dirac distribution in the conduction band

f_m Modulating frequency

f_V Fermi-Dirac distribution in the valence band

G_t Tag antenna gain

G_{rx} Receive antenna gain

G_{tx} Transmit antenna gain

J^{3D} Tunneling current

M Modulation factor

m_E^* Electron effective mass

m_H^* Hole effective mass

m_R^* Reduced effective mass

P_r Receive power

P_T Transmit power

P_t, P_{in} Power on tag

Q Quality factor

q Electron charge

r Tag to reader distance

T Temperature

T_{WKB}^{3D} Tunnelling probability

V Average received signal

V_I In-phase component of the received voltage

V_Q Quadrature component of the received voltage

V_{bb} base-band received signal

V_{bias} Biasing voltage

V_{DC} DC voltage component

Z_L Load impedance

ADS Advanced Design System

ASK Amplitude Shift Keying

BLE Bluetooth Low Energy

DC Direct Current

EIRP Equivalent Isotropically Radiated Power

FCC Federal Communications Commission

FET Field-Effect Transistor

GTPE Georgia Tech Professional Education

IC Integrated Circuit

IMPATT Impact Ionization Avalanche Transit Time

IoT Internet of Things

JFET Junction gate Field-Effect Transistor

LNA Low Noise Amplifier

MER Modulatin Error Ratio

MESFET MetalSemiconductor Field-Effect Transistor

MISFET MetalInsulator Semiconductor Field-Effect Transistor

MMIC Monolithic Microwave Integrated Circuit

MOSFET MetalOxideSemiconductor Field-Effect Transistor

pHEMT pseudomorphic High Electron Mobility Transistor

PSK Phase Shift Keying

QTR Quantum Tunneling Reflector

QTT Quantum Tunneling Tag

RCS Radar Cross Section

RF Radio Frequency

RFID Radio Frequency IDentification

SNR Signal to Noise Ratio

UHF Ultra High Frequency

VNA Vector Network Analyzer

SUMMARY

Sensor networks, radio equipped drones, and satellites are widely used in many applications such as health care, smart cities and precision agriculture. Nevertheless, the high power costs of communication per distance unit lead to poor technical solutions, particularly in terms of flexibility and efficiency. A future of devices connected through an Internet of Things (IoT) network will require billions of sensors that will affect costs and increase the energy requirements. By 2020 there will be 200 billion connected devices [1] that will use wireless technology to talk to each other and to human operators. Although the total global worth of IoT technology could be as much as 6.2 trillion USD by 2025 [2], energy consumption of these devices is an important technological aspect that needs to be addressed. Currently, a low-powered wireless module used in IoT applications requires 10.8 mW [3] to operate; if powered up by a coin cell battery[1], a single IoT device operating one third of the time will consume more than 40 batteries per year. If those batteries will need to be replaced upon discharge, they will contribute to a volume above 8.800.000 m^3 in electronic waste, filling a space exceeding the volume of 8 Empire State Buildings[2] *per year*.

Both Bluetooth Low Energy (BLE) and Radio Frequency Identification (RFID) devices have drawn attentions among researchers and industry involved in the development of IoT solutions. Although BLE provides a solid infrastructure for the IoT thanks to largely available BLE-capable devices installed in smart phones, tablets and PCs, the Radio Frequency (RF) front-end of a BLE node is complex and its high power consumption (greater than 10 mW [6]) limits portability and require continuous maintenance. Sensors based on RFID communication, on the other hand, require lower orders of magnitude of energy-per-bit for the wireless transfer of information but, despite a simpler RF front-end, their power constraints limit the communications to short ranges.

[1] Coin cell battery capacity: 0.22 Ah, voltage: 3 V, volume: 1 cm^3

[2] Empire State Building Volume: 1.047.723 m^3 [4]

Backscattering communication through RFID nodes is a promising solution to solve the energy burden of the future, but this technology is still limited in rage and cannot compete yet with the wide coverage advantages of BLE, WiFi, cellular and LoRa networks.

This thesis addresses the following question: how can we design a power-stingy backscattering device able to cover an area so wide to enable the use of RFID communications for new applications?

This work presents a highly sensitive 5.8 GHz quantum tunneling RFID tag that achieves backscattering ranges above 1.2 km while consuming biasing powers as low as 20 μW and a radio communication efficiency of 2.9 pJ/bit. This is over 10 times higher than the maximum range of a semi-passive 5.8 GHz RFID link and more than 1000 times lower energy per bit than WiFi (IEEE 802.11ac) [5]. Moreover, this device is characterized by a simple RF front-end and modulation speeds as high as 7 MHz.

This work could lead to a new class of long-range backscattering sensors with power consumption far lower than traditional radios.

CHAPTER 1
INTRODUCTION

Researchers and entrepreneurs often refer to a future with billions of connected devices that will encourage creativity and foster innovation through a network of wireless sensors implementing (among the others) traffic control, factory maintenance, and energy management. Although the number of devices connected to cell phones, portable sensors, and other handled devices is rapidly increasing, the overall energy demands still constitute a disadvantage in terms of power consumption, achievable ranges, portability, maintenance and pollution.

To be connected through an Internet of Things (IoT) network, the ultimate wireless IoT sensor needs to 1) have **low power requirements**; 2) have a **wide coverage area**; and 3) be **inexpensive**. A device enabling communications at long ranges (100 m and beyond) without the need of a power supply will open up countless applications in sensing, telemetry, and personal communications. No longer limited by range, wireless nodes will send data from flying objects (drones) and monitor the sky in real time. Inexpensive sensors on billboards and road signs will send real time data and support self-driving cars. Long-lasting wireless tags equipped on livestock will allow better traceability and subsequent big data processing in precision farming to optimize the whole agricultural process.

There are two main classes of wireless devices: *active nodes* such as WiFi, Bluetooth Low Energy (BLE) and LoRaWAN [6] generate a signal to transmit data to a receiver; *backscatter modulation nodes* such as Radio Frequency IDentification (RFID) simply reflect an impinging signal and modulate data back to a transceiver. Active nodes require a complexity of the design to be equally distributed among all the devices taking part in the communication process; they achieve long communication distances by amplifying the transmitted and received Radio Frequency (RF) signals through power amplifiers and low

noise amplifiers integrated circuits (ICs); the main disadvantage of using these components is the need of biasing powers of several hundreds of mW [7, 8, 9, 10, 11] that would greatly affect the power requirements in a future scenario of pervasive sensors. Active nodes are more expensive and require either a large bulky battery or small batteries that must be replaced or often recharged. On the other hand, both BLE and RFID devices have drawn attention among researchers [12] and industry [13] involved in the development of IoT solutions because they satisfy some of the qualities listed above. RFIDs allow devices to be *extremely simple* and move the complexity towards only one master unit: the transceiver. Although they reduce costs and complexity, they are range-limited with respect to the active ones because the signal has to travel twice. Commercial passive RFID microchips have a maximum sensitivity of only -22.1 dBm [14]; this relatively high value of RF input power necessary to wake up the node circuitry and trigger modulation limits the communication ranges to only few meters. BLE sensors can *cover long communication distances* (30 m [3]), nevertheless, the RF front-end of a BLE node requires mixers and amplifiers mounted on each node, making their costs a disadvantage for the development of a pervasive sensor network. In addition, their overall low energy efficiency, and therefore high power requirements (above 10 mW [3]), limits portability, increases energy consumption, requires constant maintenance, and causes pollution related to a continuous change of batteries.
BLE provides a solid infrastructure for the IoT thanks to largely available BLE-capable devices installed in smart phones, tablets and PCs. RFID sensors, on the other hand, are based on low power backscatter modulation techniques that allow lower orders of magnitude of energy-per-bit for the wireless transfer of information [15].

The question is, how can we design a power-stingy and inexpensive backscattering prototype with a wide coverage area that can be used in IoT applications where both long ranges, pervasiveness and energy autonomy can highly contribute to reduce the costs and increase the efficiency of wireless communications?
Combining the low power consumption and the design simplicity of RFID nodes with the

widespread BLE infrastructure can constitute a valid solution to some of the issues that the deployment of an IoT is facing [16]. From the transceiver point of view, researchers have already shown how a smart phone equipped with BLE modules can be a backscatter receiver without any changes to the hardware, the software or the firmware of the device [17]. The integration of RFID capabilities with BLE-ready devices can be further improved by introducing a Quantum Tunneling Tag (QTT) to boost the range coverage of IoT nodes nowadays limited to tens of meters.

The objective of the proposed research is to design, develop and test the RF front-end of a 5.8 GHz RFID quantum tunneling tag that, by exploiting the quantum tunneling effect of tunnel diodes, achieves high sensitivities and hundreds-meter communication ranges without affecting the design complexity and without consuming more than tens of micro Watts. The aim of this research is to demonstrate how quantum tunneling tags open the door for a new generation of RFID applications by improving the backscatter range and by extending the life cycle of battery-assisted RFID tags. Therefore, this research aims to create a whole new generation of backscattering sensors that disrupt the existing BLE and RFID technologies which have severe range, energy and environmental limitations.

1.1 Document Organization

This research focuses on the realization of a low powered backscattering device exploiting the quantum tunneling effect to amplify the impinging RF signal coming from an RF transceiver at 5.8 GHz. The goal of this work is to show how a backscattering system can achieve high distances while keeping low both the power budget and the design complexity. The document is organized as follows:

- Chapter 2 gives an overview of wireless backscattering systems, such as RFID, and illustrates a possible way to improve the currently limited ranges by using a quantum tunneling reflector (QTR) as the RF front-end of a quantum tunneling tag;

- Chapter 3 provides the state-of-the-art of reflection amplifiers and analyzes some 2-port devices that could be used to design one;

- Chapter 4 illustrates the performance of a designed quantum tunneling reflector based on a tunnel diode and provides preliminary insights of its modulation and amplification capabilities for wireless backscattering links;

- Chapter 5 analyzes the electrical parameters that might both affect the SNR of the QTR and degrade the quality of a wireless link;

- Chapter 6 provides the experimental results of a wireless measurement campaign held around and nearby the Georgia Tech campus to test the long ranges that a quantum tunneling tag (QTT) can achieve when mounting a quantum tunneling reflector (QTR). Considerations on possible use-case scenarios that would benefit from this technology are outlined and a tool to assist a system engineer to design a future long range and low powered backscattering link with quantum tunneling tags is provided. A 10 fold range improvement to a 5.8 GHz backscattering link is achieved when a quantum tunneling tag is used in place of a semi-passive one;

- Conclusions and future work are outlined in Chapter 7.

CHAPTER 2

ENHANCING THE BACKSCATTER-RADIO LINK

This chapter gives an introductory overview on wireless backscattering systems, focuses on the link budget equations and points to the possible improvement of the RF front-end of an RFID tag that would increase the communication ranges without affecting the limited power budget of this technology.

2.1 Background

In RFID systems, an RFID reader (or transceiver) transmits an RF carrier to a tag consisting of an antenna and an integrated circuit (IC). The tag serves only as a transponder that returns a portion of its received power with modulation. Communication between the reader and a tag takes place through a change in the tag's circuit impedance Z_L at the terminals of the tag antenna through proper bias of nonlinear semiconductor devices (Schottky diodes, varactor diodes, PIN diodes, and MOSFETs) [18]. By changing its impedance, the tag antenna is de-tuned causing the radar cross section (RCS) to be modulated. Modulation alters the reflected carrier in amplitude, phase, or both and the receiving portion of the RFID reader (co-located or not with the transmitter) demodulates the return signal reflected from the tag (Fig. 2.1).

Passive tags draw power from the RF energy of the reader signal; *semi-passive tags* are equipped with a battery. Both passive and semi-passive tags are simpler than a BLE node as they do not operate a local high frequency synthesizer, or a mixer, or a power amplifier; therefore they are characterized by a reduced design complexity, low costs and high power savings. Passive RFID tags are challenging because the only power available for communication is the RF power received from the far-field reader that needs to be rectified through energy harvesting techniques. In such a scenario, the low efficiency of the

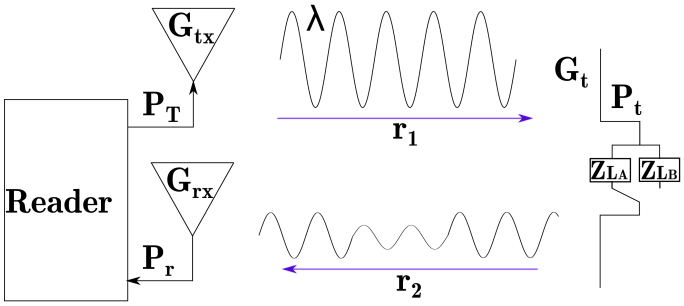

Figure 2.1: Conceptual schematic of a bistatic backscatter modulation link

energy harvesting module and the need of the RF signal to travel back and forth between the reader and the tag limit the communication ranges.

2.2 Backscatter-Radio Link Budget

The communication between a transceiver and a tag (Fig. 2.1) can be modeled as a mono-static or bi-static radar and can therefore be characterized by the radar range equation [19].

A link budget analysis for RFID systems is detailed in [18]. When the tag is located at a distance away from the reader, the power incident on the tag identifies the *power-up link budget*:

$$P_t = P_T G_{tx} G_t \left(\frac{\lambda}{4\pi r_{1_{max}}} \right)^2, \tag{2.1}$$

assuming perfect matching in impedance and polarization, no fade margin, and line of sight between the reader and the tag. P_t is the tag sensitivity corresponding to the minimum power on tag necessary to power-up its IC logic, P_T is the power transmitted by the transceiver; G_{tx} is the load-matched, free-space gain of the transmitter antenna; G_t is the load-matched, free-space gain of the tag antenna; λ is the carrier-frequency wavelength; and $r_{1_{max}}$ is the maximum achievable forward reader-to-tag distance. The *power-up link budget* is limited by the minimum power signal strength required for the tag to power up.

After powering-up, a sufficient amount of power must be sent back from the tag to the reader to transfer information. In a *bistatic* link, where two separate antennas are used at the reader respectively for transmission and reception, the amount of backscatter power

received by the reader is defined by the *backscatter link budget*:

$$P_{r_{min}} = P_T G_{tx} G_{rx} G_t^2 \left(\frac{\lambda}{4\pi}\right)^4 \left(\frac{1}{r_{1_{max}} r_{2_{max}}}\right)^4 M, \tag{2.2}$$

where M is the backscatter modulation factor, G_{rx} is the load-matched, free-space gain of the transmitter antenna and $r_{2_{max}}$ is the maximum achievable backward tag-to-reader distance. In a *monostatic* configuration, one single transceiver antenna can be used for both transmitting and receiving ($G_{tx} = G_{rx}$; $r_{1_{max}} = r_{2_{max}} = r_{max}$). The *backscatter link budget* is limited by the reader sensitivity; $P_{r_{min}}$ identifies the minimum received signal strength necessary to detect the backscattered power. Backscatter radio differs from conventional radar in that the signal transmitted from the reader is used to power the RF tag and that the RF tag intentionally communicates information back to the reader. Equations 2.1 and 2.2 are also identified as the *forward link* and the *return link*.

Up until now, tags have affected the overall system performance by limiting the forward link because of the high sensitivity requirements of their IC. While semi-passive tags are **return link limited** with recent results in the research literature showing range increases up to 21.25 m at UHF band (915 MHz) [15], passive RFID systems are currently **limited in the forward link**. Nevertheless, the sensitivity of tag ICs has been improved over the years from -8 dBm (1997) [20] to -22.1 dBm (2014) [21, 14], suggesting that the return link might become the weakest link in passive RFID communications as well.

U.S. regulations limit the maximum transmitted power P_T to 1 W and the maximum equivalent isotropic radiated power (EIRP) [22] to 4 W (36 dBm) [23] at microwave frequencies (915 MHz and 5.8 GHz). Nevertheless a designer can act on the following parameters to enhance the communication range of an RFID channel:

- $P_{r_{min}}$: an improved reader sensitivity can detect RF signals with lower power strength. Current RFID readers have a sensitivity of -105 dBm [24].

- G_{rx}: in a bistatic configuration, the receiving and transmitting antennas are separated

and the receiving gain, G_{rx}, can be increased as much as desired being only limited by the size and the portability of the RFID receiver.

- G_t: the gain of the tag antenna is only limited by the tag footprint and the maximum EIRP allowed.

- M: the backscatter modulation factor affects the RCS of a transponder. A higher RCS allows more RF power to be reflected by the tag.

2.2.1 Modulation Factor

As discussed in Sec. 2.1, an RF tag modulates the signal backscattered from its antenna by switching the load impedance between two or more states. Typically, a binary modulation scheme is used and the amount of modulated-backscatter power is described by the modulation factor M defined as [25]:

$$M = \frac{1}{4} \left| \Gamma_A - \Gamma_B \right|^2 \tag{2.3}$$

with the reflection coefficients defined as [26]:

$$\Gamma_{A,B} = \frac{Z_{L_{A,B}} - Z_{ant}^*}{Z_{L_{A,B}} + Z_{ant}} \tag{2.4}$$

with $Z_{L_{A,B}}$ being the input impedance of the RF port of the tag IC and Z_{ant} the input impedance of the tag antenna.

The power backscattered from an RF tag can also be characterized using tag's effective radar cross section; the RCS σ_{RCS} can be written in terms of load-dependent *antenna component* and load-independent *structural component*:

$$\sigma_{RCS} = \frac{\lambda^2}{4\pi} G_t^2 \left| A_s - \Gamma_{A,B} \right|^2, \tag{2.5}$$

with A_s a complex term representing the structural component and $\Gamma_{A,B}$ the antenna component. Since the backscattered signal is proportional to the difference between modulation states, the differential RCS [27] is defined as:

$$\Delta\sigma_{RCS} = \frac{\lambda^2 G_t^2}{4\pi} \left|\Gamma_A - \Gamma_B\right|^2 \tag{2.6}$$

which depends only on the antenna loads and not on the structural component of the RCS.

The objective of backscattering applications is to maximize the tag's modulation factor (or differential RCS) while still absorbing enough power to turn on the tag's IC. The choice of the modulation factor presents a trade-off in design parameters. Semi-passive tags, as they have less power constraints to power-up the IC, can switch their load between an open ($Z_{L_A} = \infty$, $\Gamma_A = 1$) and a short ($Z_{L_B} = 0$, $\Gamma_B = -1$); resulting in a maximum achievable modulation factor $M = 1$ that maximizes the power scattered back to the reader and minimize the power coupled into the RF tag. A passive RFID tag can switch its loads between a short impedance ($Z_{L_A} = 0$, $\Gamma_A = -1$) and an impedance matched to the antenna ($Z_{L_B} = Z^*_{ant}$, $\Gamma_B = 0$); resulting in an optimum modulation factor $M = 0.25$ that balances the power backscattered and absorbed by the IC of the tag. In this case, the short load can be easily obtained with a field-effect transistor (FET). Amplitude shift-keying (ASK) is achieved by switching between the load and the short. Phase-shift keying (PSK) is achieved by modulating the reactive component of the chip impedance. This allows a constant power to be supplied to the transponder IC regardless of the modulation state. Researchers in [15] have challenged the assumptions that backscatter communications only happen through magnitude change of the differential RCS and suggested a new paradigm using vector backscatter signaling. In this work we suggest to go beyond the use of passive loads and amplify the backscattered signal through micro-power biases. A graphical overview of the described modulation factor's (M) design parameters is shown in Fig. 2.2.

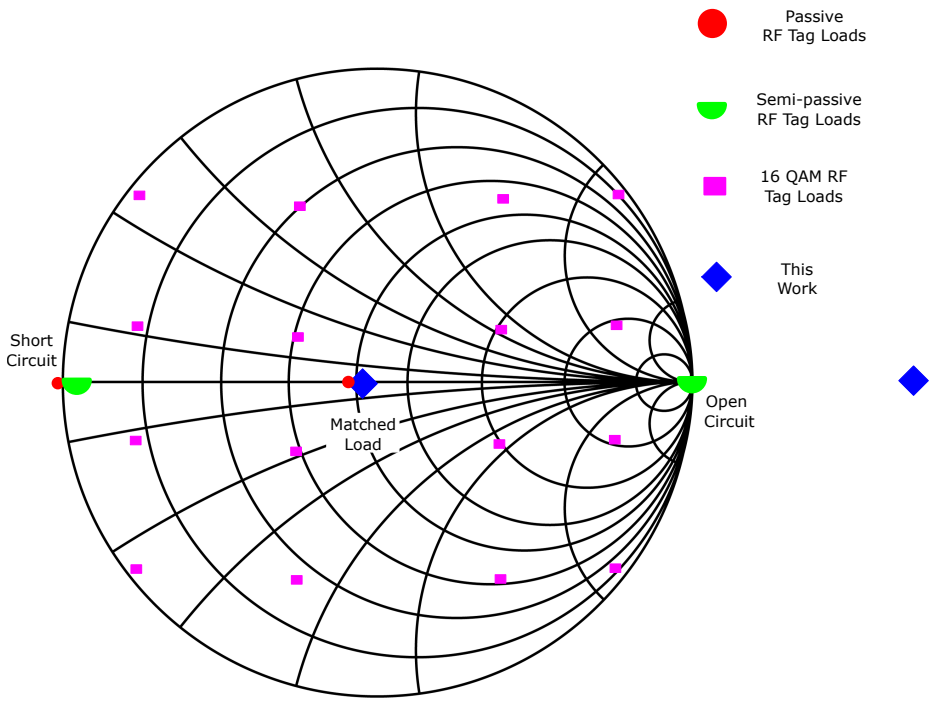

Figure 2.2: A Smith Chart showing four possible solutions to implement a backscatter-radio link.

2.3 Enhancing the Backscatter-Radio Link

In Fig. 2.3a, the link budgets of UHF (915 MHz) and microwave (5.8 GHz) backscattering systems are computed by combining Eq. 2.1 with Eq. 2.2 and by assuming a reader with sensitivities $P_{r_{min}}$ of -84.4 dBm (for monostatic configuration) and -105 dBm (for bistatic configuration) [24]. Ideal passive transponders have a modulation factor M = 0.25 with IC sensitivity P_t = -22.1 dBm [14][1]; therefore, they need to be at a maximum free space distance r = 42 m (at 915 MHz) or r = 6.6 m (at 5.8 GHz) from a transceiver in co-located bistatic configuration to receive an RF signal of power P_r sufficiently high to be detected. The increasing sensitivity of tag ICs will eventually make the transceiver the weakest node in this communication scenario. Semi-passive tags (M = 1) are already limited in the return link.

By combining Eq. (2.1) and Eq. (2.2), it is possible to highlight the relationship be-

[1]The tag and reader sensitivities here cited apply for UHF devices. Same sensitivities have been assumed for the 5.8 GHz case.

tween the modulation factor M and the sensitivity of a transceiver when a transponder is at the maximum possible distance from it [20]:

$$P_{r_{min}}(M) = \frac{MP_t^2}{P_T}. \tag{2.7}$$

By fixing the maximum transmitted power P_T to 1 W (30 dBm), the minimum received power at the reader $P_{r_{min}}$ is function of the modulation factor M and the minimum power P_t on the tag necessary to activate its IC. Higher power levels, $P_{r_{min}}$, will be received from transponders requiring high values of impinging power, P_t, or bigger modulation factors, M.

Since increasing P_t in Eq. 2.7 reduces the maximum achievable distance, the backscatter-radio link can be enhanced by modifying the RF front-end of a tag transponder so that the modulation factor M and the RCS are improved. In [28] and [29], it has been suggested the use of **reflection amplifiers** equipped with active loads. Reflection amplifiers are characterized by a **negative resistance** that, at the cost of a certain amount of biasing power, can amplify the backscattered RF signal, by displaying an $M > 1$, and therefore, increase the communication range of a backscattering system.

This work will focus on the design and test of a tunnel diode-based reflection amplifier and on the wireless tests used to demonstrate that backscattering ranges above 100 m at 5.8 GHz are achievable for extremely low biasing powers.

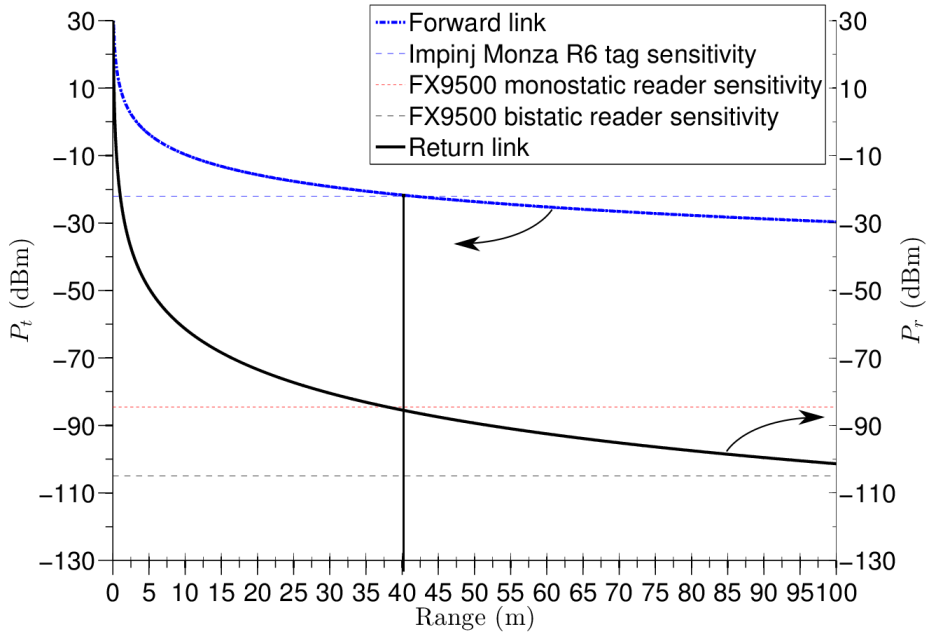

(a)

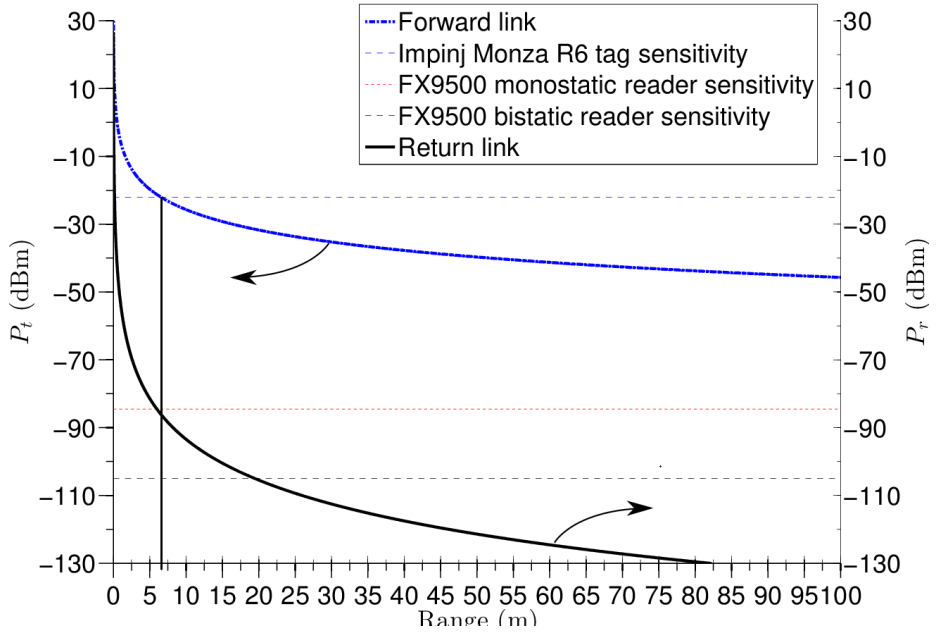

(b)

Figure 2.3: Forward and return links of a) 915 MHz and b) 5.8 GHz RFID passive system. P_T = 30 dBm, $G_{tx} = G_{rx}$ = 6 dBi, G_t = 0 dBi, M = -6 dB (0.25). The horizontal lines represent respectively the maximum tag and reader sensitivities ($P_{t_{min}}$ and $P_{R_{min}}$) [14, 24] currently available.

CHAPTER 3

ACTIVE LOADS FOR LOW-POWERED BACKSCATTERING LINKS

This chapter introduces the electronic devices that have been used or could be used to enhance low-powered backscattering links and focuses on the quantum tunneling effect. The chapter ends with a thorough state-of-the-art on reflection amplifiers available in the research literature. A comparison of their performances in terms of gains and power consumptions is shown together with the variation of the power requirements undergone throughout the years.

Contributions of this chapter:

- an overview of electronic devices used to design reflection amplifiers;
- a state-of-the-art of reflection amplifiers.

3.1 Electronic Devices for Backscattering Applications

Negative resistance can be achieved by a number of solid-state devices when properly biased: *Gunn diodes*; *impact ionization avalanche transit time* devices (IMPATT); *tunnel diodes*; and *transistors*. While transistors (under different configurations) are nowadays more common and used from DC to millimeter-wave frequencies, Gunn, IMPATT and tunnel diodes are **two-terminal devices** with the advantage, over transistors, of having simple biasing circuits.

After the invention of the transistor in 1948, many variations where developed and three major kinds of field-effect transistors can be now identified [30]: 1) the JFET (junction field-effect transistor) in which charge carries, electrons or holes, flow from the source to the drain; 2) the MOSFET (metal-oxide-semiconductor FET), a special case of the MISFET (metal-insulator-semiconductor), that uses oxide as an insulator between the metal

and the semiconductor; and 3) the MESFET (metal-semiconductor FET) that has become the dominant microwave solid-state device employed in monolithic microwave integrated circuits (MMIC) technology.

Transistors are commonly used in backscattering applications: the antenna of the transponder has its terminals connected in series to a capacitance and a transistor. By switching the transistor on and off, the antenna is de-tuned by the capacitive load causing the RCS to be modulated. The reflected portion of the carrier signal is impressed with an envelope (altering amplitude, phase or both) carrying binary data.

3.2 Two-terminal Active Devices

All the two-terminal devices have the common property of displaying a natural negative resistance when properly biased. The physical phenomena that make this possible are different and here briefly described:

- the **impact-ionization and transit-time effects** take place in the IMPATT diodes. The concept of the IMPATT diode was first proposed by Read in 1958 for a diode structure (n^+pip^+) now known as a Read diode [31]. The Read diode can be divided into two regions: the **avalanche region** (inside the n layer), where the impact ionization occurs and electrons and holes are generated, and the **drift region**, where the carriers drift at the saturation velocity. A breakdown voltage, together with an RF signal, applied to the diode causes avalanche breakdown; due to the time delay in the avalanche and drift processes, there is a phase shift between the applied RF voltage and the generated current. If the phase shift is greater than 90^o, the negative resistance is created. In 1965, the IMPATT effect was also observed in a pn diode [32].

- the **transferred electron effect** generates a negative resistance in Gunn diodes. It was discovered for the first time in 1963 by J. B. Gunn [33]. The existence of a

negative resistance is often called the Ridley-Watkins-Hilsum mechanism from the names of those that first explained it [34, 35]. In an n-type Gunn diode (n^+nn^+), the negative resistance is attributed to the two-valley band structure: a high-mobility lower conduction band (lower valley) is separated by a low-mobility upper conduction band (higher valley). At room temperature, the electrons are in the lower conduction band; when low voltage is applied, the current increases linearly. Higher voltages move some electrons from the low valley to the higher valley and, since the electron mobility in the higher valley is smaller than that in the low valley, current decreases. While all electrons have moved from the low valley to the higher valley, a linear increase of current proportional to the applied voltage starts again. The decrease of current as an effect of increased voltage gives the Gunn diode its natural negative resistance.

- the **quantum tunneling effect** will be the focus of section 3.3; it was first observed in 1958 by Leo Esaki and Brian Josephson [36].

Gunn diodes require high bias voltages to display a negative resistance region and the IMPATT diodes need to be biased with a voltage level equal to the voltage breakdown (2 V or above). Moreover, IMPATT diodes have 10 dB higher AM noise than Gunn diodes. On the other hand, tunnel diodes, by exploiting the quantum tunneling effect, require very low biasing voltages (0.12 V) that can be beneficial for RFID applications and any other applications with a limited availability of DC power.

3.3 Tunnel Diodes and the Tunneling Effect

A tunnel diode (also know as an Esaki diode) is the first manufactured semiconductor where quantum tunneling was observed. After its discovery [36, 37], the physics of tunnel diodes has been extensively discussed [38].

As with other semiconductors, a tunnel diode simply consists of a pn junction with a

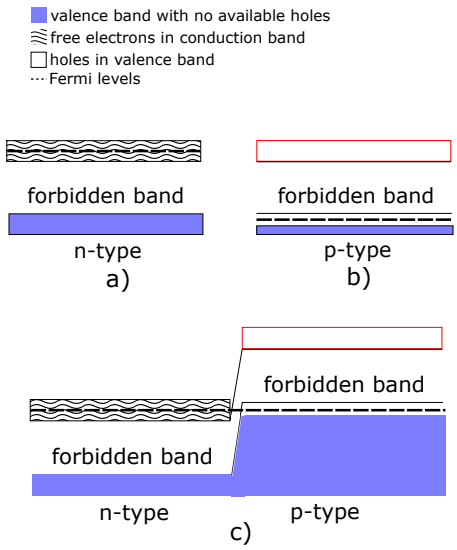

Figure 3.1: Degenerate semiconductors.

high concentration of donors and acceptors (p^+n^+). By heavily doping an n-type semiconductor (e.g. $10^{19}\ \frac{charges}{cm^3}$), the high amount of donor impurities results in states in the bottom of the conduction band completely occupied by electrons. This degenerate n-type semiconductor has the Fermi level moved up in the conduction band (Fig. 3.1a). Similarly, in degenerate p-type semiconductors, the top of the valence band is completely free of electrons and the Fermi level is moved inside the valence band (Fig. 3.1b) [39]. When a pn junction is formed, an extremely thin junction voltage barrier is created as a result of keeping the continuity of the Fermi level (Fig. 3.1c).

Normally the electrons on the two sides of a pn junction are isolated because their energy is not sufficient to surmount the potential barrier. If the junction is thin enough, quantum mechanics states that there is a finite probability of tunneling for electrons in the n-type region to the empty states of the valence band in the p-type region when an external biasing voltage is applied [39]. By applying a reverse bias to a tunnel diode, quantum tunneling takes place (Fig. 3.2a): the electrons in the valence band of the p-type semiconductor can see unoccupied states of equal energy in the conduction band on the other side of the forbidden region and tunnel from one side of the junction to the other. If the reverse bias is increased, the supply of electrons able to tunnel increases without limit.

At zero bias, no electrons can see empty states and no tunneling occurs (Fig. 3.2b). By applying a low forward voltage, some electrons in the conduction band are now opposite the holes in the valence band and a forward current is observed (Fig. 3.2c). Tunneling charges produce a sharp increase of current with a slight variation of voltage up to a maximum current i_1 (Fig. 3.2f). Increasing the bias, fewer and fewer electrons can see empty states to which they can tunnel (Fig. 3.2d), quantum tunneling fades and current decreases to i_2 (Fig. 3.2f). Current remains small until minority carrier injection takes place giving rise to the exponential characteristic of a common diode (Fig. 3.2e).

Because of the shape of its I-V curve, a tunnel diode can find different uses [40]. For large biases (region III in Fig. 4.1), it behaves like a Schottky diode and can be used in mixer applications; at zero bias (region I), a heterostructure backward tunnel diode can be used for energy harvesting applications [41]. Finally, the decreasing current as effect of the increasing bias in region II gives to the tunnel diode a natural negative differential resistance $-R$ that can be used to design a reflection amplifier whose low biasing power can be of great advantage for backscattering systems whose power budget is typically very low. The biasing voltage necessary to trigger a negative resistance in the tunnel diode could be further reduced by changing the doping of the junctions: with lower doping, the initial overlap between conduction and valence bands can be reduced and the peak current will take place at lower biases. However, currents will be reduced and the values of achievable $-R$ will be affected.

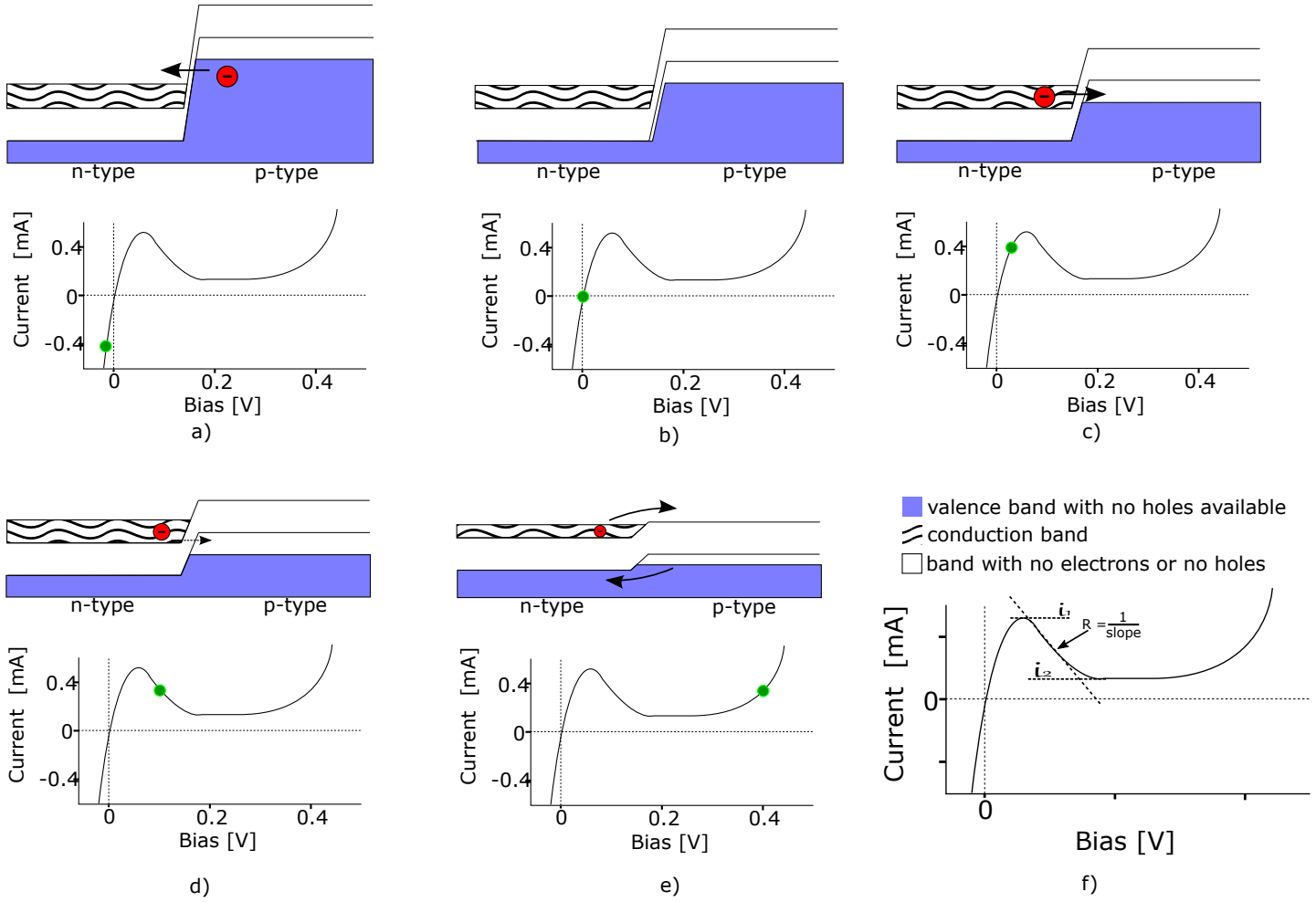

Figure 3.2: The tunneling effect.

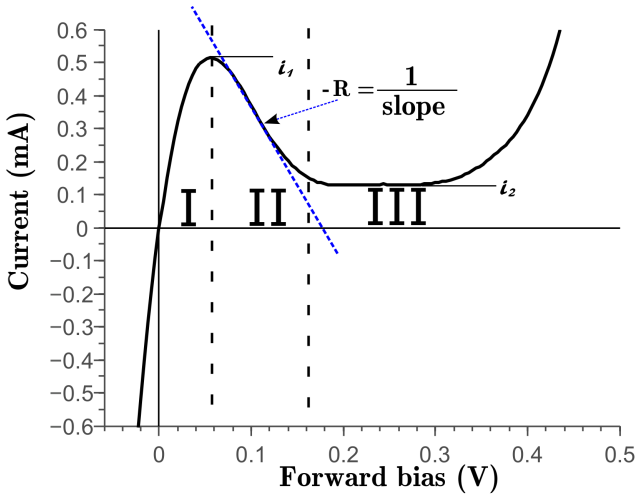

Figure 3.3: Example I-V characteristic of a tunnel diode.

3.3.1 Tunneling Probability and Current

Tunneling current is determined by integrating the product of charge flux and the tunneling probability from the energy states on the p^+ side to those on the n^+ side [42]. The tunneling probability is calculated by applying the Wentzel-Kramers-Brillouin (WKB) approximation [43] to the triangular potential of the p^+n^+ junction.

The tunneling process through the forbidden gap of the electrons in the valence band of the p^+ side into the conduction band of the n^+ side can be approximated by a particle penetrating a triangular potential barrier, of height E_G (the semiconductor band-gap) and slope $q\mathcal{E}$, with $\mathcal{E}$ being the electric field and q being the electron charge [42]. For bulk direct semiconductors, the total energy can be divided into two parts $E = E_x + E_\perp$, where $E_x = \frac{\hbar^2 k_x^2}{2m_R^*}$ corresponds to the energy in the tunneling direction and $E_\perp = \frac{\hbar^2(k_y^2+k_z^2)}{2m_R^*}$ is the transverse energy which is conserved during the tunneling process, $\hbar$ is the reduced Planck constant, and the reduced effective mass $m_R^* = \left(\frac{1}{m_R^*} + \frac{1}{m_H^*}\right)^{-1}$ averages both the electron m_E^* and hole m_H^* effective masses.

The tunneling probability is calculated using the WKB approximation [43]:

$$T_{WKB}^{3D} = \exp\left(-\frac{4\sqrt{2m_R^*}(E_G + E_\perp)^{3/2}}{3q\hbar\mathcal{E}}\right) \approx \exp\left(-\frac{4\sqrt{2m_R^*}E_G^{3/2}}{3q\hbar\mathcal{E}}\right)\exp\left(-\frac{E_\perp}{\bar{E}}\right), \tag{3.1}$$

with $\bar{E} = \frac{q\hbar\mathcal{E}}{2\sqrt{2m_R^* E_G}}$. The larger is $\bar{E}$, the less is the degradation of tunneling probability by carriers with transverse energy. Therefore, the effect on tunneling by transverse states is minimized by high electric field, small effective mass, and narrow bandgap.

The tunneling current in then calculated by integrating the product of the charge flux and the tunneling probability between the p^+ and the n^+ sides. To simplify the calculation, the Fermi-Dirac distributions f_V and f_C at the valence and conduction bands are assumed so that $f_V - f_C \approx 1$, giving:

$$J^{3D} = \frac{\sqrt{2m_R^*}q^3\mathcal{E}V_R}{8\pi^2\hbar^2 E_G^{1/2}}\exp\left(-\frac{4\sqrt{2m_R^*}E_G^{3/2}}{3q\mathcal{E}\hbar}\right) \tag{3.2}$$

Eq. 3.2 suggests that narrower band-gap materials with smaller effective mass can achieve tunneling current densities approaching that of a high-performance MOSFET. For the same electric field, Ge tunneling is more than two orders of magnitude greater than Si, while InAs and InSb are about three orders of magnitude higher.

3.4 Reflection Amplifiers for Backscattering Applications

Reflection amplifiers are characterized by a negative load impedance Z_L that, at the cost of a certain amount of biasing power, can reflect and amplify an impinging RF signal.

In two-terminal devices such as Gunn diodes, IMPATT diodes and tunnel diodes, the impedance is function of frequency (f), DC bias (V_{bias}), RF input power (P_t) and temper-

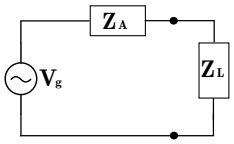

Figure 3.4: Equivalent circuit of a reflection amplifier.

ature (T) [30]

$$Z_L = Z_L(f, V_{bias}, P_t, T) \tag{3.3}$$

A general reflection amplifier circuit is shown in Fig. 3.4, with Z_L being the two-terminal device and $Z_A(f_0)$ being the antenna (or the circuit) impedance at the desired frequency f_0:

$$Z_A(f_0) = R_A(f_0) + jX_A(f_0) \tag{3.4}$$

When the following conditions are met:

$$X_A(f_0) + X_L(f_0, V_{bias}, P_t, T) = 0 \tag{3.5}$$

that is, when $X_A = X_L^*$, and

$$Z_L(f_0, V_{bias}, P_t, T) = -R_L + jX_L, R_L > 0 \tag{3.6}$$

then, Z_L has a negative resistance and:

$$|\Gamma|^2 = \left|\frac{Z_L - Z_A^*}{Z_L + Z_A}\right|^2 = \left|\frac{-R_L - R_A}{-R_L + R_A}\right|^2 = \left|\frac{R_A + R_L}{R_A - R_L}\right|^2 > 1 \tag{3.7}$$

meaning that a negative RF power $-I^2R_L$ is generated from the DC power supply and added to the RF power already available at the end of the circuit. Clearly, any amount of gain can be obtained by the proper choice of R_A; moreover, when $R_A = R_L$, the gain becomes infinite and the device oscillates. Therefore, for stable application, $R_A \neq R_L$.

When connected to a matched antenna of impedance Z_A, the reflection amplifier gives a modulation factor M with magnitude greater than 1; this results in an amplified reflected signal that can increase the ranges achievable by backscatter modulation systems.

3.4.1 State-of-the-art

As described in Sec. 2.2.1, backscatter modulation can be implemented through amplitude shift keying (ASK) to enable communication between an RFID tag and a reader. ASK is achieved by varying the complex RCS of an RFID antenna. The RCS depends on the reflection coefficient at the interface between the antenna and the input impedance of an RFID transponder; therefore, switching the input impedance among two passive loads, e.g. open and short, allows to change the RCS and hence, to modulate the backscattered signal.

In some recent papers, researchers have challenged the idea of using passive loads by suggesting the use of active reflection amplifiers: [44, 45, 46, 47, 48, 49, 50, 51, 52, 53, 54, 55, 56, 57]. Reflection amplifiers increase the RCS of an RFID transponder and can improve both the downlink and uplink range of an RFID system. Differently from an active system that needs a significant amount of power for its RF front-end and constant maintenance, an RFID equipped with a reflection amplifier can improve the communication range while keeping low both the energy requirements and the complexity of the circuitry.

Researchers from National Chiao Tung University proposed a reflection amplifier using a pseudomorphic heterojunction pHEMT (NE32584c). In their paper [55], the design of a reflection amplifier for an RFID transponder is presented; key to this design is an RF load impedance at the terminal of the tag antenna that exhibits a negative value at the desired frequency. To obtain the desired RF load impedance, a biasing voltage is applied to the drain of the transistor and a high-impedance choke isolates it from the radio wave impinging at the gate. Moreover, a microstrip line and an open stub microstrip have been connected respectively to the source and the drain of the transistor. By controlling the lengths of the microstrips, the RF load impedance exhibits a negative value for specific

frequencies. The authors crafted two RFID transponders: a two-element array connected to two microstrip reflection amplifiers and a passive four-element array. When biased with the appropriate amount of voltage, the former topology showed a backscattering field level 4.5 dB higher than the latter at a center frequency of 6.04 GHz.

Advantages and disadvantages of using reflection amplifiers with RFID transponders have been highlighted in [54]. At K band (18 - 27 GHz), tuning at the wanted frequency can be difficult as parasitic components can produce a 2-3 GHz shift from the center frequency and an additional frequency shift (750 MHz) is observed when varying the biasing voltage level. The authors measured a maximum gain of 14 dB at 21.2 GHz using a total biasing power of 209.3 mW. Moreover, the return gain is completely absent outside the main band resulting in no amplification of unwanted signals. Amplitude modulation as well as phase modulation can be performed with transponders equipped with a reflection amplifier load: the amplitude of the return link signal can be modulated by simply turning on and off the biasing voltage of the load and a change in phase can be triggered by varying the bias level.

The idea of tuning the biasing voltage on and off to implement amplitude modulation is further explored in [53]. To demonstrate this concept, the authors paired the reflection amplifier with a patch antenna to receive an impinging sinusoidal carrier. With the reflection amplifier biased to produce 7 dB gain at the carrier frequency, a 10 kHz drain modulation voltage was applied and the reflected modulated signal was measured on a spectrum analyzer. Comparisons of the envelope signal received with and without the presence of the modulation voltage demonstrates that ASK is possible using a reflection amplifier. Moreover, the device is sensitive to impinging signals ranging between -50 and -75 dBm. The authors also report that a slight change in the original design contributes to increase the signal to noise ratio at the expenses of a higher biasing voltage.

Chan implemented a full-duplex communication to improve both the return link and the forward link capabilities of an RFID tag [49]. The author incorporated a transmission amplification capability into a reflection amplifier: the transmission amplifier transmits and

amplifies a received forward link signal. Simultaneously, the reflection amplifier modulates, reflects and amplifies the signal for the return link data stream. A 13 dB return gain and a 10 dB forward gain at 5.25 GHz for a total DC power consumption of 2 mW have been reported.

Several researchers have built upon these early results suggesting different types of FET-based reflection amplifiers [48, 49, 50, 51, 52, 53, 54, 55]. Table 3.1 gives an overview of the results reported in the research literature and shows, through the gain-per-bias-power ratio, how much gain (in dB) is added to the reflected RF signal per units of μW. Fig. 3.5 focuses the attention on both the achieved gains and the power requirements: gains as high as 31.5 dB have been reported for biasing power requirements falling in the range between 0.12 mW and 330 mW. Most of the research results here highlighted have tested the potential of reflection amplifiers built with off-the-shelf components. The design of reflection amplifier with two-terminal devices was outlined in [58] and a Josephson junction exploiting the tunneling effect using superconductors at cryogenic temperatures [46] has shown a very high sensitivity, high gain and low power consumption.

Table 3.1: Overview of reflection amplifiers available in literature.

Reference	Year	Device Type	Part number	Substrate	DC Bias Power (mW)	Gain (dB)	Bias Volt. (V)	Bias Curr. (mA)	RF Input (dBm)	Freq. (GHz)
[59]	2016	tunnel diode	MBD5057-E28	Ge	0.045	40	0.09	0.5	-75	5.8
					0.039	29	0.11	0.354	-84	
[44]	2015				0.029	41.4	0.069	0.418	-92	
[45]					0.045	34.37	0.08	0.566	-70	5.45
[48]	2014	bipolar trans.	BFT25A	Si	0.325	10.2	0.755	0.431	-50	0.920
[49]	2013		BFP405		2	13	2.5	0.8	-55	5.25
[52]		MESFET	CFY30	GaAs	18	10.2	3	6	-	4.5
[46]		Josephson junc.	-	-	-	30	-	0.054	-145	2.7
[47]	2012	MOSFET			0.120	22.3	0.8	-	-71.9	4
[50]	2011	pHEMT	NE32584C		6.3	11.48	0.7	9	-	5.8
[53]	2008	pHEMT	-	GaAs	209.3	14	2.3	91	-75	21.2
[54]	2006		CGY2134UH		330	14	2.2	-	-45	21.2
[55]	2003		NE32584C		-	8.1	-	-	-	6.26
[56]	1991	MESFET	NE71083		-	12	-	-	-	9
[57]	1979	FET	-		2000	16	4	500	-	13
[51]	1972	avalanche diode	-	-	12.75	31.5	85	0.150	-15	7.4

Table 3.2: Details on reflection amplifier technologies listed in Table 3.1.

Reference	Technology	Device name	Substrate	Junction type
[44] [45]	Tunnel Diode	MBD5057-E28	Ge	p^+n^+
[46]	Josephson Junction	-	-	pn
[47]	MOSFET			-
[48]	Bipolar transistor	BFT25A	Silicon	npn
[49]		BFP405		
[50]	pHEMT	NE32584C	GaAs	-
[51]	Avalanche diode	-	-	p^+nn^+
[52]	MESFET	CFY30	GaAs	-
[53]	pHEMT	-		
[54]		CGY2134UH		
[55]		NE32584C		
[56]	MESFET	NE71083		
[57]	FET	NE		

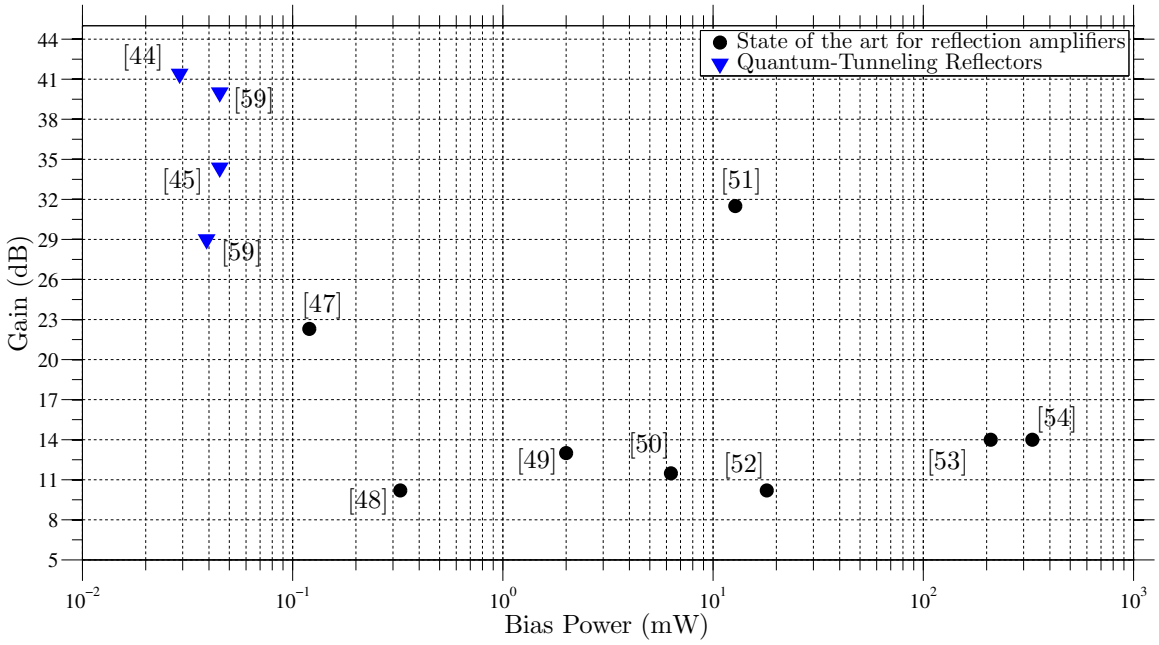

Figure 3.5: State-of-the-art of reflection amplifiers. Comparisons of return gains and required biasing DC powers. An earlier version of this plot is published in [45].

Future trends

With these papers, some authors have suggested that reflection amplifiers can play a key role in extending the communication range of semi-passive RFID transponders. The gain provided by these devices can promote the use of backscatter modulation beyond the short range of current passive and semi-passive RFID systems. A new class of transponders can also be envisioned. While a semi-passive RFID tag has an incorporated battery to power its circuitry, this new class will use highly sensitive wireless harvesting modules to both modulate the return link signal through the reflection amplifier and provide power to the digital section of the RFID chip. Meanwhile, new low power and long range semi-passive RFID tags exploiting the tunneling effect can already be developed. The low power requirements of the reflection amplifier will guarantee a greater longevity of the tag if compared with that of a traditional semi-passive transponder and longer communication ranges will be achieved: at 21 GHz, a return link range of 2 m has been estimated by [54] for an incoming signal level of -45 dBm, while a measured return link range of 25 m for 0.5 W transmit power located 8.3 m from the receiver at 5.25 GHz has been estimated in [49]. A manufactured ad-hoc FET-based reflection amplifier with high gain and low power consumption is reported in [47] suggesting promising results for ad-hoc quantum tunneling devices.

3.5 The Quantum Tunneling Reflector

The data reported in Table 3.1 and Fig. 3.5 are compared against the gains and the low bias power requirements achieved in this work where tunnel diodes have been used to manufacture a reflection amplifier. The 5.8 GHz tunnel diode-based prototypes exhibit 27 dB more gain and 10 dB lower power consumption than state-of-the-art CMOS-based reflection amplifiers. They show reflection gains as high as 40 dB for a total biasing power consumption of lass than 45 μW.

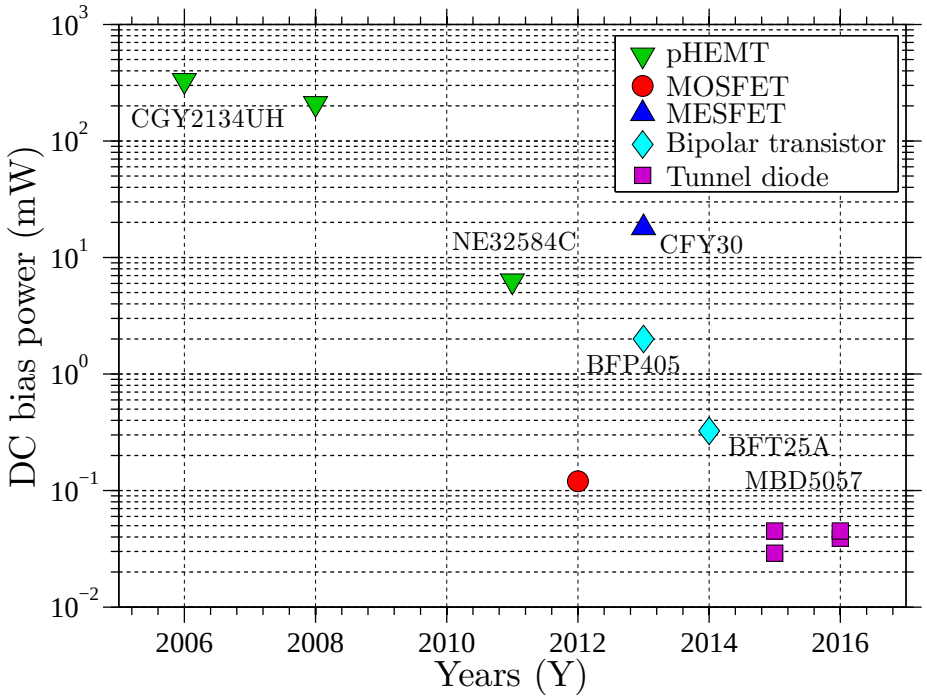

Figure 3.6: Data from Table 3.1 show a decreasing power consumption of reflection amplifiers in recent years; tunnel diode-based reflectors lead the trend.

As shown in Fig. 3.6, the results obtained with this work have advanced the performances of other reflection amplifier solutions appearing in the research literature. The power consumption of reflection amplifiers has been decreasing during the recent years and tunnel diode-based reflection amplifiers can be a natural step towards less power-hungry electronics since a quantum tunneling reflection amplifier drastically reduces the amount of required power for the RF front-end of an RFID tag.

The achieved high gains (up to 40 dB) and the low biasing power requirements (less than 45 μW) suggested the fabrication of a quantum tunneling RFID tag capable of amplifying the backscattered signal by applying a proper modulating bias voltage (Fig. 3.7).

3.6 Chapter Conclusions

In this chapter, the state-of-the-art of reflection amplifiers available in the research literature has been described. These data were used to understand what performances have been

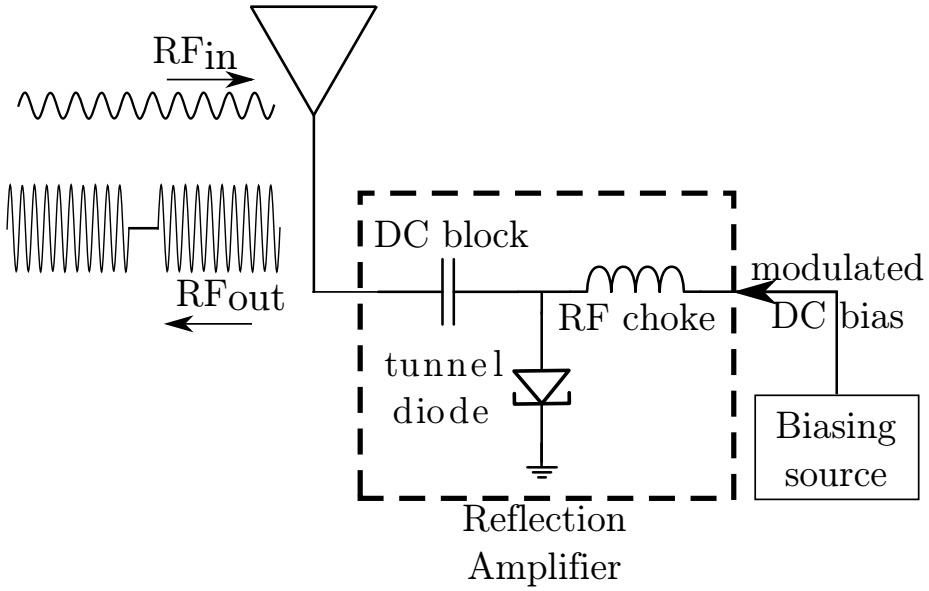

Figure 3.7: Block diagram of a quantum tunneling RFID tag.

achieved so far and how lower power consumptions and simpler designs can be obtained by using a 2-port device.

Among the 2-port devices, a tunnel diode is suggested to develop long range and low powered backscattering tags.

CHAPTER 4
THE QUANTUM TUNNELING REFLECTOR

In this chapter, after an introduction to the theory of reflection amplifiers, a mathematical model of a tunnel diode is presented and the circuit model of a quantum tunneling reflector (QTR) is shown, simulated, fabricated and tested. Experimental results of two quantum tunneling reflectors exhibit 27 dB more gain and 10 dB lower power consumption than state-of-the-art CMOS-based reflection amplifiers

Contributions of this chapter:

- characterization of tunnel diode MDB5057-E28;
- definition of a circuit model for a QTR at 5.8 GHz;
- simulation and realization of two QTR prototypes;
- experimental results characterizing the performances of the two prototypes;
- achieved reflection gains of 40 dB and 29 dB for a total biasing power consumption of 45 μW and 39 μW respectively for impinging power levels as low as -84 dBm;
- a testing procedure for the characterization of a QTR;
- a test on the modulation capabilities of the QTR;
- an estimate of the achievable ranges of a backscattering communications system using a quantum tunneling tag (QTT).

4.1 Oscillators

A reflection amplifier is based on the concept of an oscillator that, when properly biased, *locks* at the frequency of the input signal. Through *injection locking*, an external signal onto the oscillator affects both its instantaneous amplitude and frequency. The occurrence of locking depends on 1) the oscillator circuit parameters; 2) the amplitude of the external signal; and 3) the locking range 2Δf [60]. The locking range is the maximum difference between the resonant frequency of the oscillator and the injected signal frequency at which locking occurs [30]:

$$\frac{2\Delta f}{f} = \frac{2}{Q}\sqrt{\frac{P_{in}}{P_0}} \tag{4.1}$$

with P_0 being the locked power. Eq. 4.1 is a function of the external signal amplitude P_{in}, the oscillator frequency f, and the quality factor Q. In general, the greater the amplitude of the locking signal the greater will be the locking range; high oscillator frequencies and circuits with low Q also result in large locking ranges [61]. If G is the gain of the reflection amplifier, we can rewrite Eq. 4.1 as

$$\Delta f = \frac{f_{in}}{Q\sqrt{G}} \tag{4.2}$$

Thus, a reflection amplifier can lock onto a broader range of input frequencies Δf if the circuit Q-factor and/or the amplifier gain is reduced.

4.2 A Quantum Tunneling Reflector (QTR) - Fabrication

The low biasing requirements and the natural negative differential resistance of a tunnel diode make this device a good candidate to realize a reflection amplifier with high reflective gains and low power consumption. A prototype has been fabricated and tested in laboratory using the off-the-shelf tunnel diode MBD5057-E28 [62]. The device operates up to 18 GHz, has a peak-to-valley current ratio of 2.5, and is fabricated using rapid thermal

diffusion on Germanium substrate.

4.2.1 Device Characterization

The I-V characteristic (Fig. 4.1) of the chosen tunnel diode has been measured at room temperature (300 K) using a DC power supply to bias the device, mounted on a PCB, and an HP 34401A precision digital multimeter to measure the current. The device under test shows a non-uniform negative differential resistance region in the voltage range spanning between 70 mV and 280 mV due to an inconsistent doping profile in the tunnel diode. This results. This results in two separated negative differential resistance intervals: from 70 mV to 160 mV ($|-R|$ = 465 Ω) and from 210 mV to 280 mV ($|-R|$ = 426 Ω). In the region between 160 mV and 210 mV there is little or no negative differential resistance so no significant RF amplification of an impinging signal is expected. For this particular device model, the reduced span of uniform negative differential resistance region limits amplification to only low power RF signals. Although low power levels are typically encountered in backscattering communications, a more uniform characteristic curve can extend the results obtained in this work to higher input power levels.

4.2.2 Circuit Design

In order to use a tunnel diode as reflection amplifier, the following criteria needs to be met [58]: bias the tunnel diode in the negative differential resistance region of its characteristic curve; present the transmission line with a suitable negative resistance at the center frequency f_{in}; reduce Γ to acceptable limits at frequencies away from f_{in}; and maintain stability. Keysight Advanced Design System (ADS) has been used to simulate and design the reflection amplifier matched at 50 Ω for low impinging power levels. The Harmonic Balance method has been used in ADS; after running the momentum simulation of the designed microstrip line, a momentum model has been created and imported into a new schematic where it has been connected to the lumped circuit components (DC-block capac-

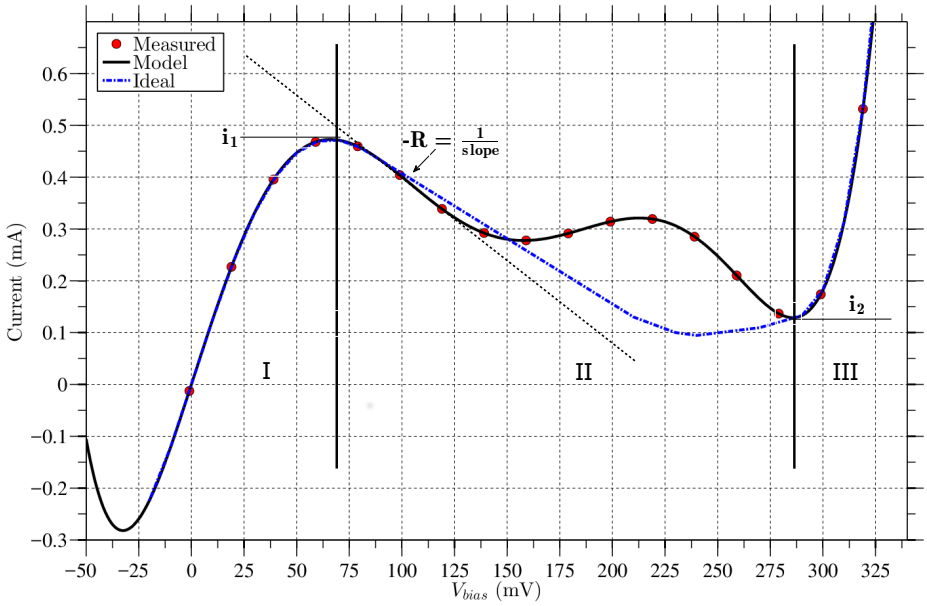

Figure 4.1: I-V characteristics for an ideal tunnel diode, used for illustration purposes; the measured MBD5057-E28 diode at 300 K; and the model used for simulations.

itor, tunnel diode model, biasing power supply and RF input signal). A circulator, together with voltage and current probes, have been inserted into the simulation to measure the RF input and output powers and calculate the return gains.

The circuit schematic, together with the tunnel diode MBD5057-E28 equivalent circuit, are shown in Fig. 4.2: an external power supply biases the tunnel diode at the desired voltage V_{bias} to amplify the RF signal input injected through a source with impedance Z_A; an inductor L_1 separates the biasing network from the input RF section while a capacitor, C_1, is used as DC-block, finally, an inductor, at short distance ϵ from the tunnel diode, compensates the undesired internal capacitance of the device. The small signal equivalent circuit of the diode is also highlighted: L_p = 0.4 nH and C_p = 0.8 pF account for the packaging parasitics; C_j = 0.03 pF represents the internal junction capacitance considered constant for the low-powers used in this work; the nonlinear junction resistance is modeled

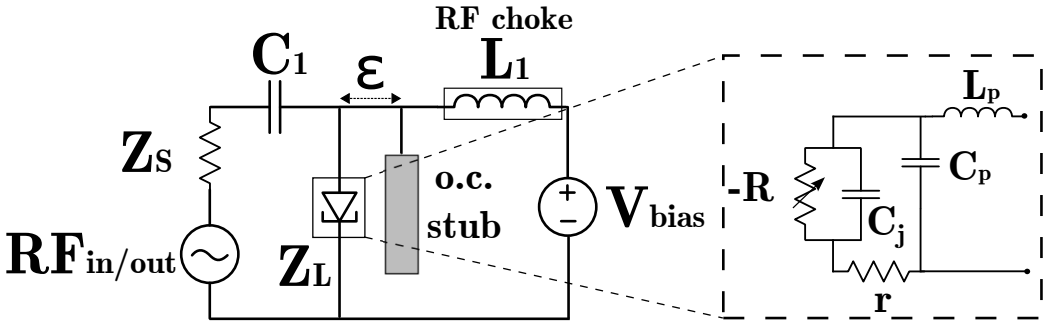

Figure 4.2: Circuit schematic of a quantum tunneling reflector (QTR) with an open circuit tuning stub at short distance (ϵ) from the diode; the equivalent circuit of the tunnel diode is highlighted: C_j = 0.03 pF is the internal junction capacitance, C_p = 0.8 pF and L_p = 0.4 nH are the packaging parasitics and r = 0 Ω is the negligible linear resistance; a voltage controlled source, G, models the nonlinear junction resistance through Eq. 4.3.

through a voltage controlled source defined by:

$$I(V_{bias}) = 0.0126V_{bias} + 0.0068V_{bias}^2 - 2.6201V_{bias}^3 + \\ +24.3383V_{bias}^4 - 84.2936V_{bias}^5 + 101.8188V_{bias}^6, \tag{4.3}$$

with V_{bias} being the applied biasing voltage. The series linear resistance r is considered negligible as it is much smaller than the junction resistance. As shown in Fig. 4.1, the model is valid in the biasing range of interest (0 to 300 mV).

4.2.3 Board Assembly

The quantum tunneling reflector (QTR) has been realized on a 4-layer board [63] to take advantage of the reduced thickness between the top and the first inner layer. The first inner layer (0.7 mils of copper) has been used as a ground plane for a microstrip line. The top layer with 1.4 mils (0.035 mm) of copper is separated from the ground plane by a 6.7 mils (0.17 mm) FR408 substrate [64]. The substrate has a relative permittivity $\epsilon_r = 3.66$ and loss tangent $\tan\delta = 0.0127$ at 5 GHz. Via holes with 13 mils (0.033 mm) diameter and square pads with 15 mils (0.038 mm) side have been used. The realized board (Fig. 4.3) uses a radial stub acting as the inductor L_1 to separate the biasing network from the rest of the circuit and a tuning stub. This stub allows to fine tune the quantum tunneling

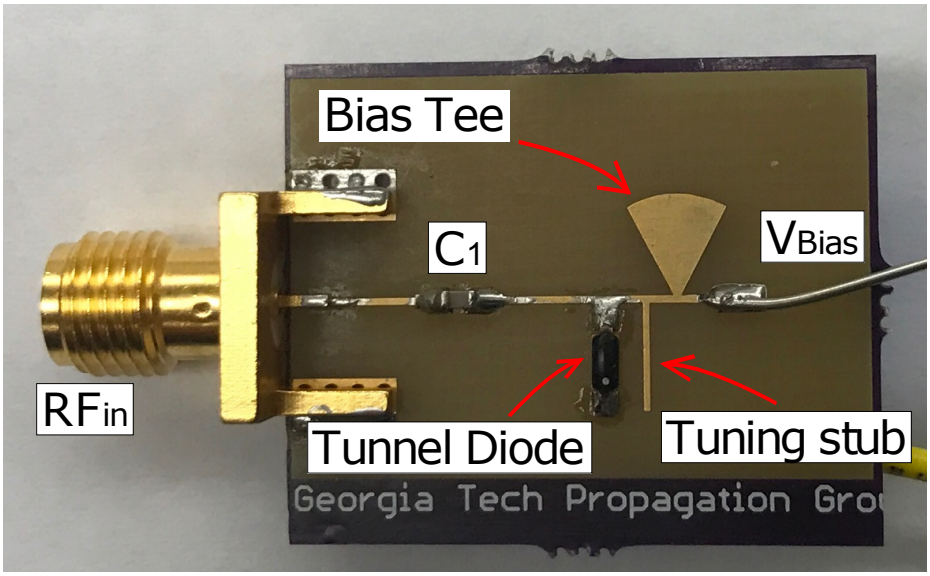

Figure 4.3: Microstrip line structure of the fabricated quantum tunneling reflector (QTR): the tuning stub is 100 mils (2.54 mm) long and 10 mils (0.254 mm) wide. Its exposed trace, not covered with silkscreen, can be used for tuning purposes, if necessary. A capacitor C_1 of 1.5 pF has been used as DC block. Two identical boards have been used to test two MBD5057-E28 tunnel diodes (#1 and #2).

reflector at the desired center frequency f_{in} of 5.8 GHz, if necessary. Two tunnel diodes (#1 and #2) have been mounted on two identical boards; Johanson Technology S603DS 0603 capacitors have been used for DC blocking. The tunnel diode devices have long leads that need to be cut to assemble the QTR. Cuts of different length, together with the $\pm$0.10 pF tolerance of the capacitors, have shown a slightly different performances of the fabricated QTR prototypes.

4.3 Quantum Tunneling Reflector (QTR) - Testing

4.3.1 Experimental Setup

Setups for measuring the refleced output of the QTR amplifiers are shown in Fig. 4.4. In both setups, an ammeter is used to record the average DC current drawn by the two fabricated QTRs during measurements. In setup (a), a vector network analyzer measures the s_{11} parameters of the QTRs. In setup b), an RF spectrum analyzer records the reflected

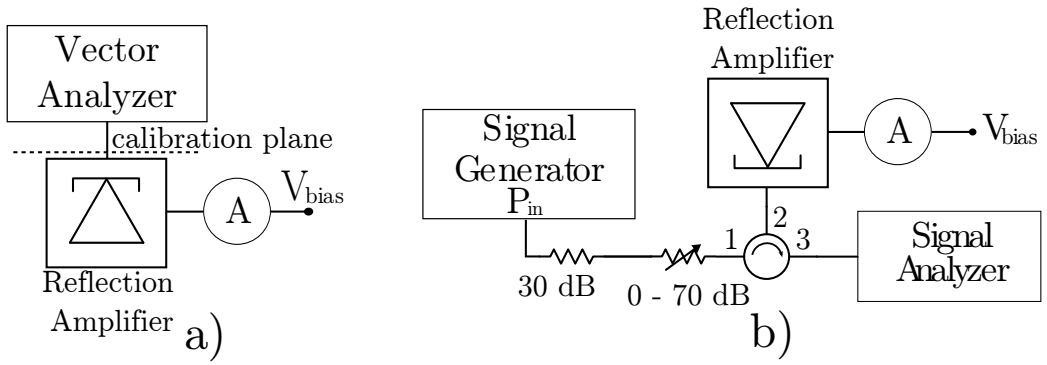

Figure 4.4: Setups used to collect experimental data. a) reflection measurements on VNA E5071B with avg. 16. b) Reflection measurements with circulator, signal generator E8247C and signal analyzer CXA-N9000A. Signal analyzer setup: resolution BW 3 kHz, video BW 100 kHz, avg. 10, span 1 MHz.

and amplified RF output signals generated by the device under test and verifies that the QTR is not spontaneously emitting active frequencies outside the targeted band. Step attenuators have been used to attenuate the RF input signal impinging on the reflection amplifier and prevent harmonics. Attenuations introduced by each additional RF component (cables and circulator) have been carefully measured and removed from the collected data.

4.3.2 Experimental Results

- Experiments on VNA E5071B: The one port S-parameter data, $|s_{11}|$, have been collected using the measurement setup shown in Fig. 4.4a with the calibration plane located at the SMA input port of the QTR. Experimental results show that the fabricated reflection amplifiers can be used in backscatter communications for both phase and amplitude modulations by varying the biasing voltage over time. The results obtained for different biasing voltages are shown in Fig. 4.5a and 4.5b for tunnel diode #1 and #2, respectively. When the biasing voltage is off, neither amplification nor oscillations of the QTRs occur within the frequency band. When the biasing voltage forces the tunnel diode into the negative differential resistance region, the prototypes display high reflection gains for an RF input signal at about 5.8 GHz. In Fig. 4.5 it is highlighted the absence of oscillations and how reflection gains exist

only around the center frequency while they are absent outside the main band, hence preventing unwanted signal amplification. As expected by the I-V characteristic of the tunnel diodes under test (Fig. 4.1), both the prototypes show a high gain for two separate biasing voltages: 1) at 90 and 270 mV for the prototype mounting tunnel diode #1 and 2) at 110 and 280 mV for the prototype with tunnel diode #2. There is no amplification for biases around 180 mV.

The effect of biasing on the s_{11} phase is shown in Fig. 4.6. A drastic change is evident when the biasing voltage is switched from 0 to 90 mV for tunnel diode #1 and from 0 to 110 mV for tunnel diode #2. The QTR mounting tunnel diode #1, at 5.8 GHz, has a phase of -69° for V_{bias} = 90 mV; the QTR with tunnel diode #2 has a phase of 37° when V_{bias} = 110 mV at 5.8 GHz. Finally, both the devices have a phase of 80° when no bias is applied.

The changes in amplitude and phase of the QTR reflection coefficients Γ have also been considered. The collected data points are compared with the unitary black circle typically used on Smith Charts. The effects of the biasing voltages on the reflected signals are shown in Fig. 4.7: high values of Γ occur at biasing voltages ranging in the two negative differential resistance regions of the tunnel diodes. The coverage of the 5.8 GHz band (5.725 to 5.875 GHz) is shown in Fig. 4.8: the maximum values of Γ are obtained at the central frequency of 5.8 GHz and they slowly decay when the frequency approaches the band limits.

- Experiments on signal generator E8247C: a useful way to test the QTRs consists in connecting the devices to a circulator to effectively separate the input from the output powers; the measurement setup shown in Fig. 4.4b has been used to record the data reported in Fig. 4.9, 4.11 and 4.12.

  The sensitivity of the manufactured prototypes to different levels of input power is shown in Fig. 4.9. The highest return gains (40 dB and 29 dB) are obtained for

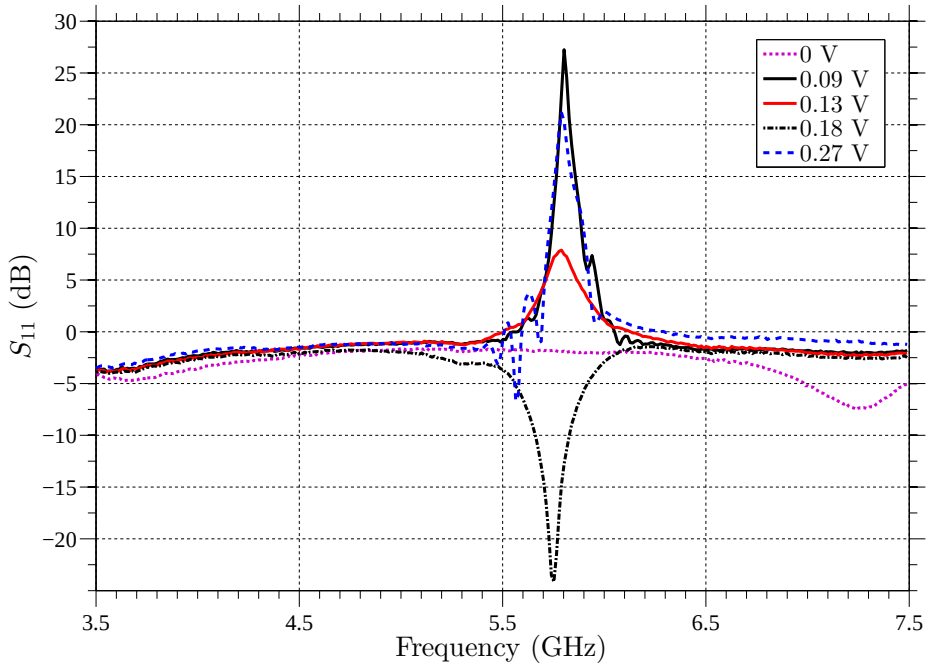

(a)

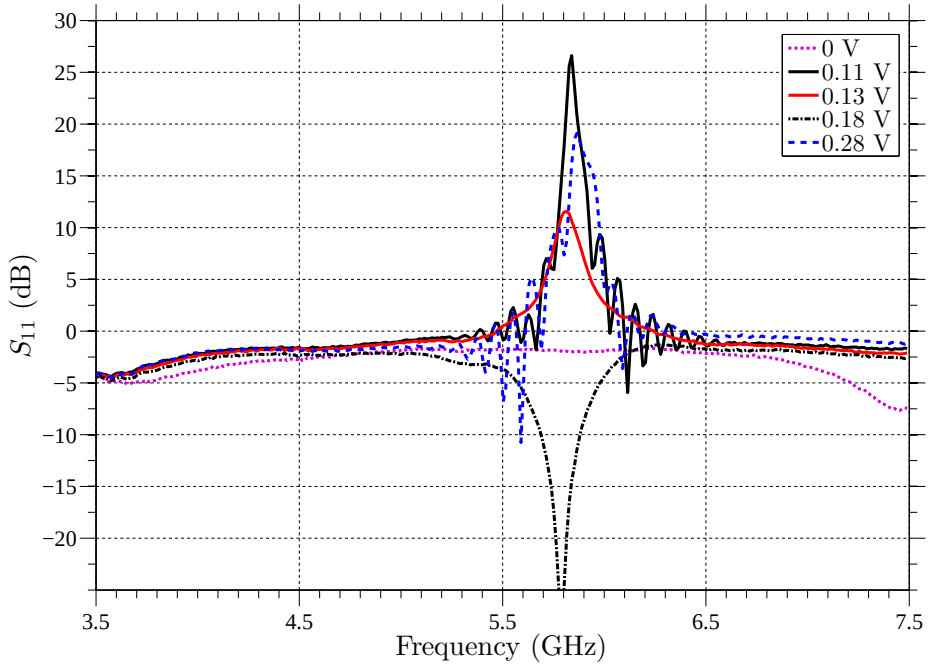

(b)

Figure 4.5: S-parameter sweeps for QTRs mounting a) tunnel diode #1 and b) tunnel diode #2 at different biasing levels. RF signal input power P_{in} = -50 dBm.

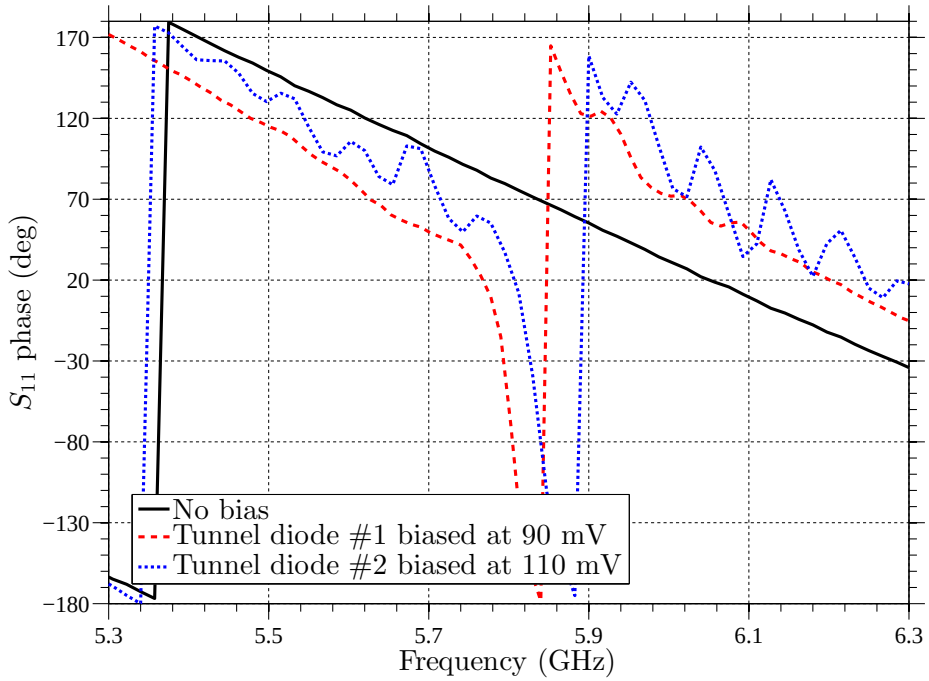

Figure 4.6: S-parameter phase sweeps for the two QTRs when no bias or optimal bias are applied. RF signal input power P_{in} = -50 dBm.

RF input powers of -75 dBm and -84 dBm respectively. The tunnel diodes have been biased at 90 mV and 110 mV and currents of 500 μA and 354 μA have been measured for total biasing powers of 45 μW and 39 μW. The experimental results agree with the simulations performed in ADS, but follow the simulations for devices matched at two different input power levels even though two identical boards have been used with two MBD5057-E28 tunnel diodes. The causes can be likely identified in a non-uniform soldering of components on the prototypes. Both simulations and experiments show a non uniform trend of the return gains; in fact, as summarized in Eq. 3.6 and shown in Fig. 4.10, the tunnel diode impedance Z_L depends, among other variables, on the input power level P_{in}: the higher the power levels the higher is the mismatch and the lower are the return gains.

In Fig. 4.11, the bandwidths of the QTRs are shown: at frequencies away from the 5.8 GHz band, no amplifications are observed, preventing the device from amplifying unwanted signals. Finally, in Fig. 4.12, the effects of the biasing voltage on the

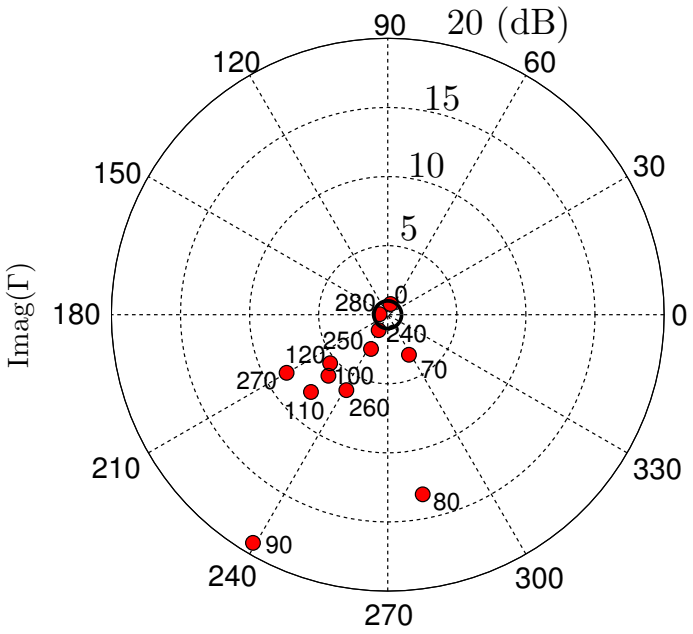

(a)

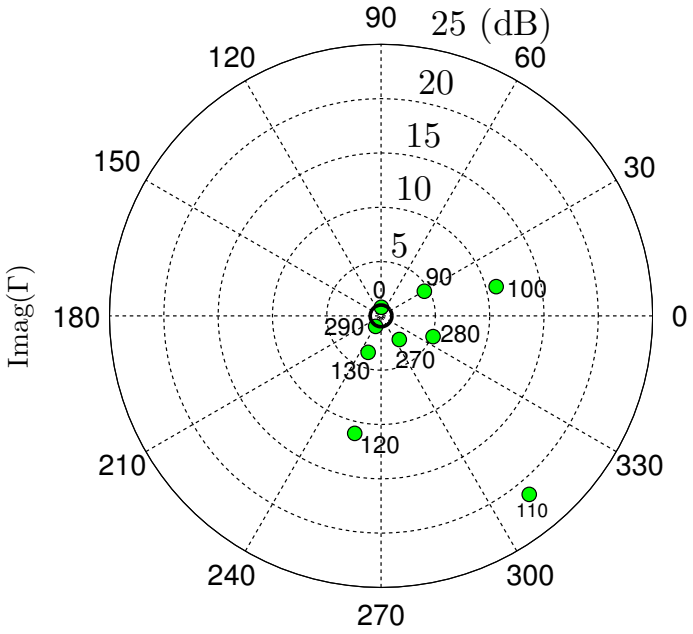

(b)

Figure 4.7: Reflection coefficients Γ (real and imaginary components) of the RF signal output for different biasing voltages (in mV); the unitary circle is highlighted. RF signal input power P_{in} = -50 dBm, RF input frequency: 5.8 GHz. Experiments done with a) tunnel diode #1 and b) tunnel diode #2.

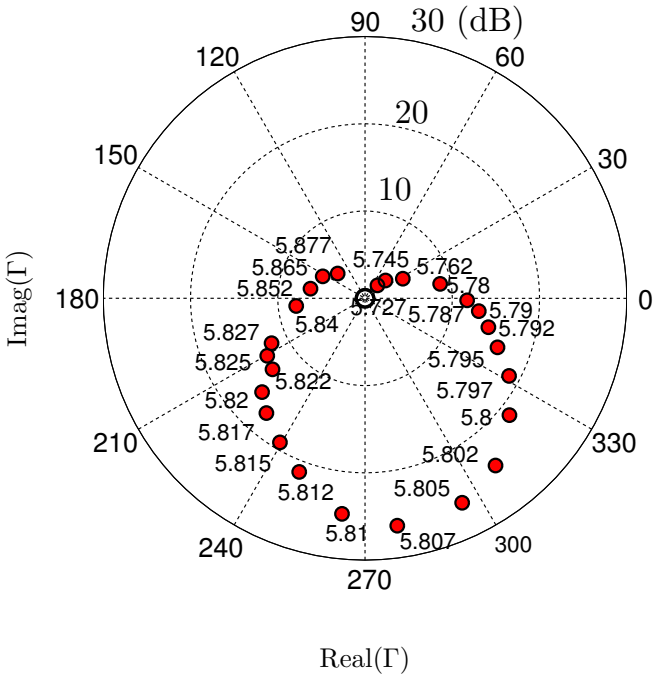

(a)

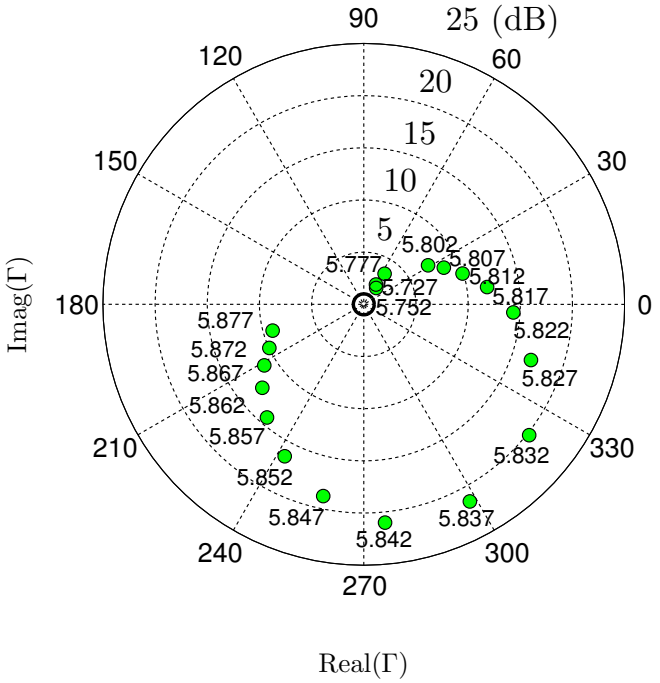

(b)

Figure 4.8: Reflection coefficients Γ (real and imaginary components) of the RF signal output for different input frequencies (in GHz) spanning in the 5.8 GHz band (5.725 GHz to 5.875 GHz); the unitary circle is highlighted. RF signal input power P_{in} = -50 dBm. Experiments done with a) tunnel diode #1 biased at 90 mV and b) tunnel diode #2 biased at 110 mV.

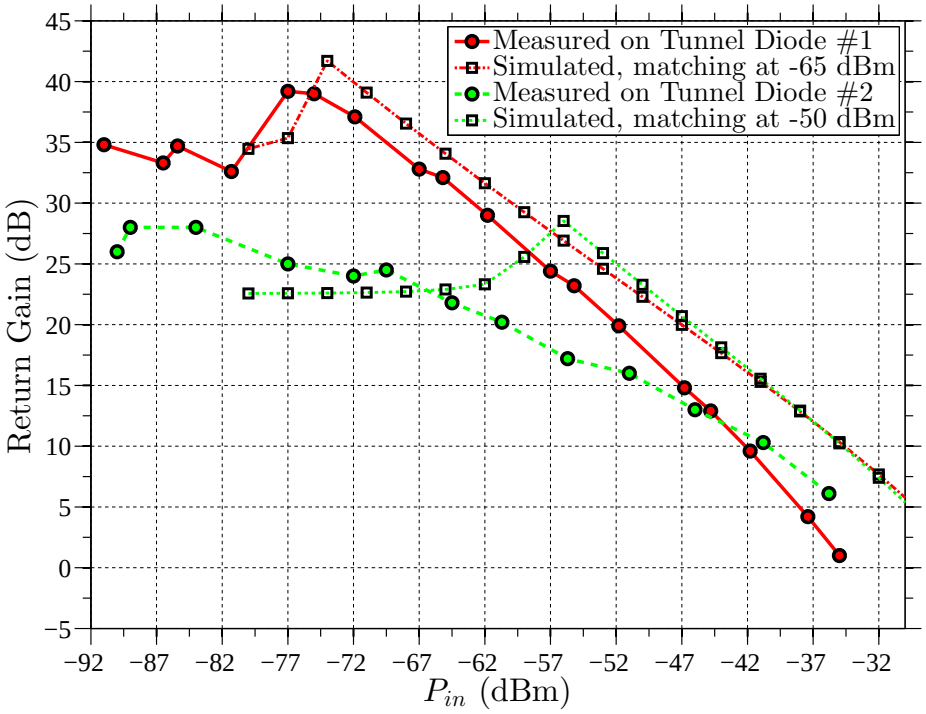

Figure 4.9: QTR gains, G_{QTR}, as function of the RF input power at 5.8 GHz. Tunnel Diode #1: V_{bias} = 90 mV, I_{bias} = 500 μA, P_{bias} = 45 μW. Tunnel Diode #2: V_{bias} = 110 mV, I_{bias} = 354 μA, P_{bias} = 39 μW. The measured gains are compared with simulation results.

output gains have been highlighted for both the amplifiers when a 5.8 GHz input signal is applied at optimum power levels (-75 dBm and -84 dBm respectively). As expected by the tunnel diode measured characteristic curve (Fig. 4.1), two peak gains are observed at two different voltage intervals. Differently from Fig. 4.5, gains are observed in the biasing range from 160 to 210 mV; an explanation of these results can be found in the use of different RF input powers P_{in} in the two experimental setups.

4.4 Testing Procedure for QTR Characterization

The experiments described in the previous section suggest a procedure to characterize a fabricated quantum tunneling reflector:

- Upon fabrication, a reflection amplifier is first tested on a VNA (Fig. 4.4a). The VNA is used to verify that amplifications occur at the desired central frequency f_{in}

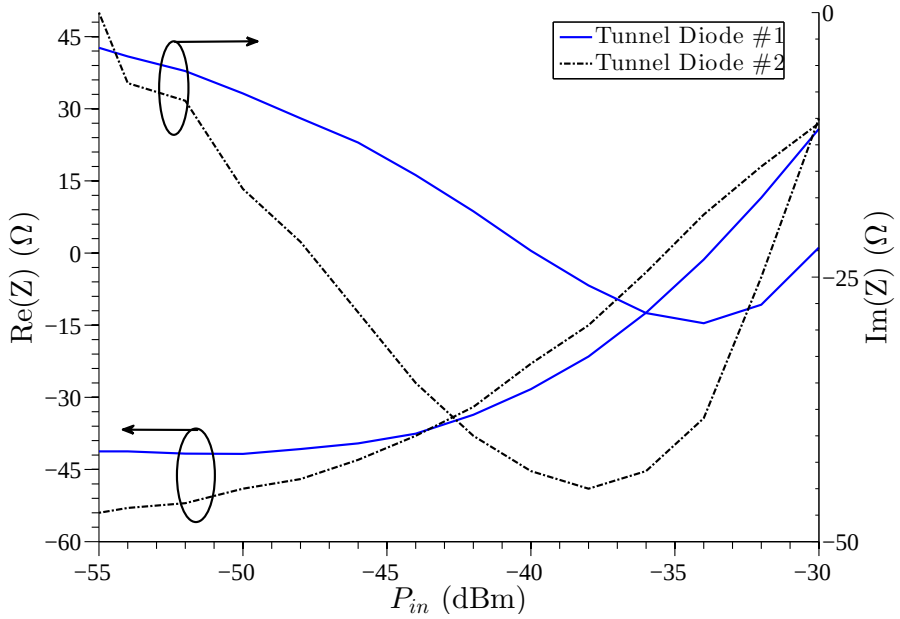

Figure 4.10: Measured impedance of the two reflection amplifiers for variable RF input powers at 5.8 GHz, when optimum biases are applied.

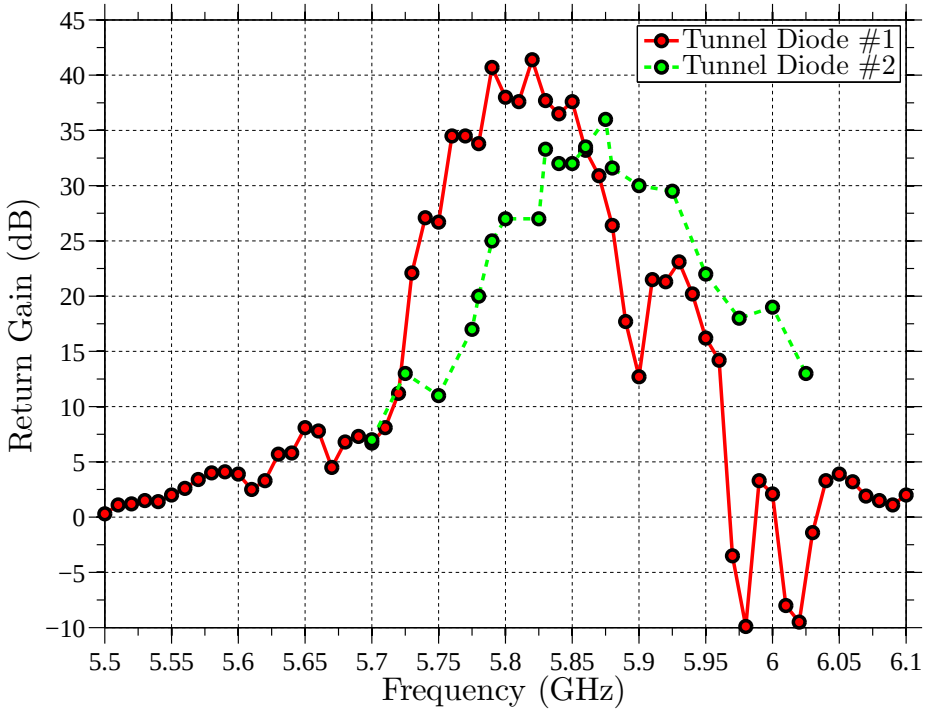

Figure 4.11: QTR gains, G_{QTR}, as function of input frequency. Tunnel Diode #1: RF input power P_{in} = -75 dBm, V_{bias} = 90 mV. Tunnel Diode #2: RF input power P_{in} = -84 dBm, V_{bias} = 110 mV.

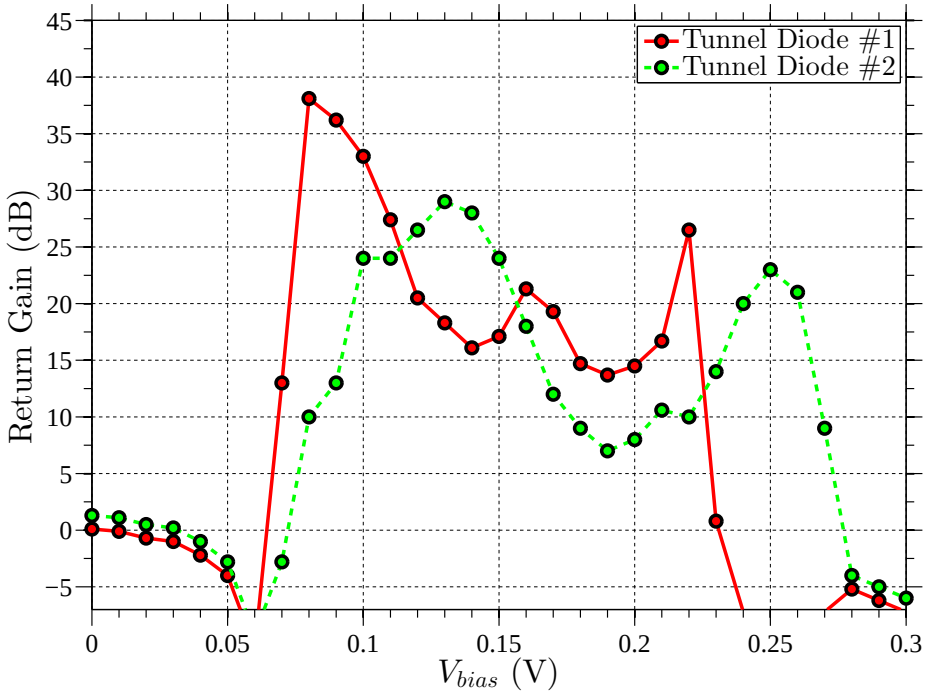

Figure 4.12: QTR gains, G_{QTR}, as function of the V_{bias} for RF input at 5.8 GHz. Tunnel Diode #1: RF input power P_{in} = -75 dBm; tunnel Diode #2: RF input power P_{in} = -84 dBm.

and that no amplification takes place outside the defined bandwidth (Fig. 4.5);

- An optimal biasing voltage providing the highest return gain is identified;
- Using a signal generator (Fig. 4.4b), a test is held to verify that the identified biasing voltage provides the maximum return gain at the central frequency f_{in} (Fig. 4.12);
- Return gains G_{QTR} are measured for different strengths of RF input power P_{in} so that a characteristic curve of the QTR can be traced (Fig 4.9).

4.5 Modulation Tests

As modulation with the realized quantum tunneling reflectors takes place by biasing on and off the tunnel diode, a wave generator has been used as the biasing source for the setup shown in Fig. 4.4b. By using a 250 kHz square wave as biasing source for tunnel diode #1, a -55 dBm RF input has been injected into the reflector and its output measured

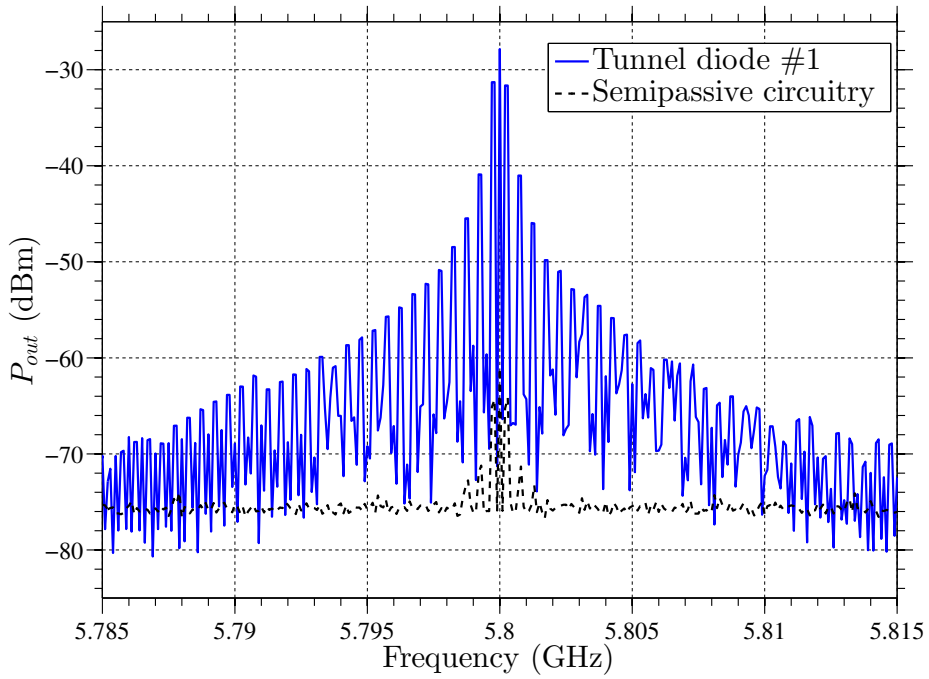

Figure 4.13: Comparing modulating and amplifying capabilities of the QTR prototype #1 with a semi-passive tag when a low RF power input (P_{in} = -55 dBm) is injected. Carrier at 5.8 GHz, fundamental frequency at 250 kHz away from it, and harmonics are shown.

on the signal analyzer; an RF input power of same intensity has been injected into the circuitry of a semi-passive tag and the output has been recorded; Fig. 4.13 compares the outputs and highlights the great benefits of using a QTR over a semi-passive tag: high sensitivities and high return gains. Additionally, a one-byte word (0xA4) has been coded using Manchester encoding (10011001 01100101b) and reproduced by the wave generator to bias tunnel diode #1 receiving an RF input power P_{in} of -55 dBm. The reflected signal has been demodulated in the time domain; the obtained results are illustrated in Fig. 4.14 and compared with an ideal waveform.

Table 4.1: Encoded one-byte word.

Hex word	binary sequence	Manchester encoding
0xA4	1010 0100	10011001 01100101

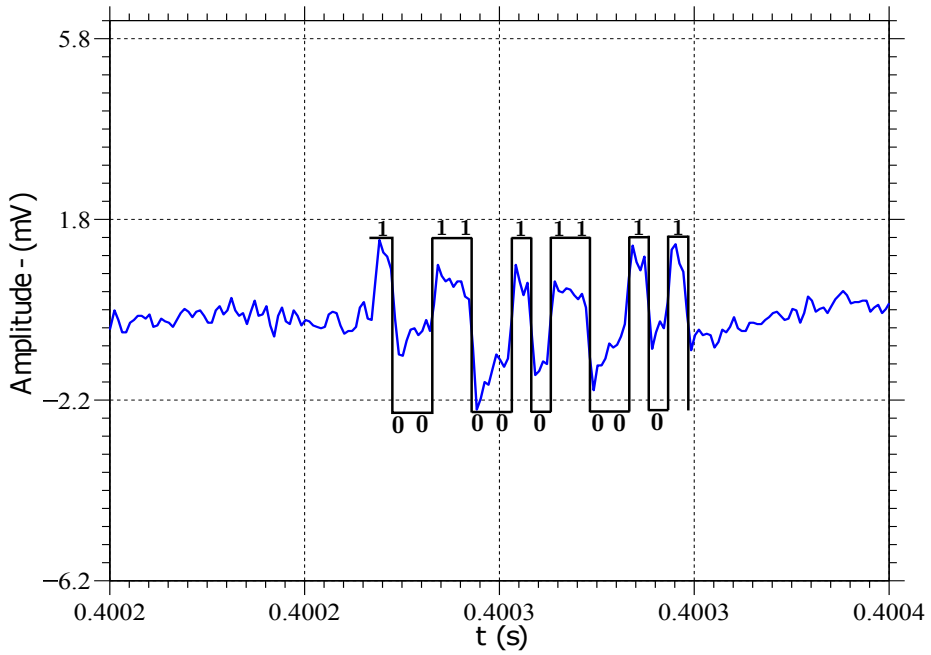

Figure 4.14: Measure of the time-domain base-band signal resulting from the 0xA4 word modulated with Manchester encoding, reflected by QTR #1 and directly sent into the RF receiver. The QTR RF input power is P_{in} = -55 dBm.

4.6 Achievable Wireless Ranges

Using the experimental data in Fig. 4.9 of tunnel diode #1 as the modulating factor $M_{|dB} = G_{QTR}$, the achievable ranges of a 5.8 GHz quantum tunneling tag (QTT) have been computed through Eq. 2.2. A QTT is a backscattering transponder consisting of a tag antenna and a quantum tunneling reflector. The results are shown in Fig. 4.15 and compared with the achievable ranges of ideal passive and semi-passive tags when transmitting a 36 dBm CW (EIRP): at high distances, the QTT provides a factor of 10 range improvement to the RFID link while keeping the bias power one order of magnitude lower than other reported reflection amplifiers. Passive tags have a maximum sensitivity of -22.1 dBm [14] that corresponds to a maximum return link range of 6.6 m at 5.8 GHz; on the other hand, QTTs, by being sensitive to RF input signals as low as -85 dBm and by providing amplification to the impinging RF carrier, can reach a theoretical backward link of 9 km (assuming the link parameters listed in Fig. 4.15 are used).

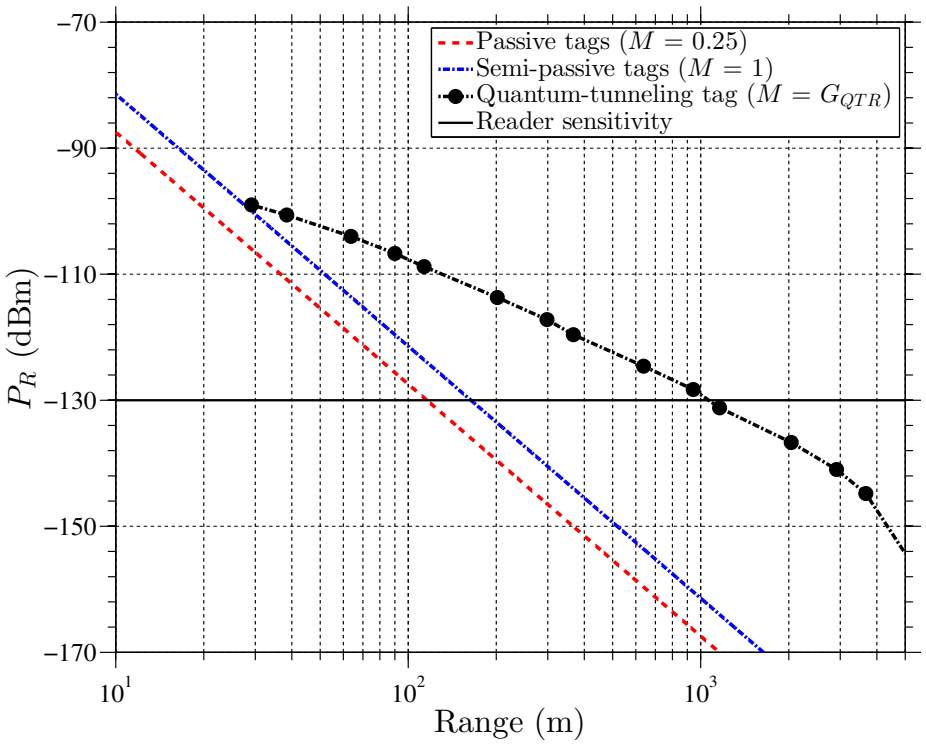

Figure 4.15: RFID link budget analysis: P_T = 30 dBm, $G_{tx} = G_{rx} = G_t$ = 6 dBi, f_{in} = 5.8 GHz. The return gains from Fig. 4.9 have been used as the quantum tunneling reflector gain G_{QTR}. The 6 dB shift between the ideal passive and the semi-passive tags is due to the different modulation factor M; the different slope of the quantum tunneling tag link budget is due to the dependence of G_{QTR} on the RF power level P_t impinging on the tag. At low impinging power levels, the QTT prototype achieves one order of magnitude higher ranges than ideal passive and semi-passive tags.

4.7 Chapter Conclusions

A properly biased tunnel diode displays a natural negative impedance that can be exploited to fabricate low power reflection amplifiers. By adequately separating the applied DC bias from the impinging RF signals through a DC block and an RF choke, it is possible to backscatter, modulate (both in amplitude and phase) and amplify extremely weak radio signals [59]. The fabricated prototypes showed gains up to 40 dB in the frequency range between 5.725 GHz and 5.875 GHz for impinging power levels as low as -84 dBm and for biasing powers below 45 μW. These results suggest that a tunnel diode-based reflection amplifier can be a valid solution to increase the range of backscattering applications (e.g.: RFID) where low biasing power levels are usually available or preferred.

CHAPTER 5

SIGNAL-TO-NOISE RATIO OF THE QUANTUM TUNNELING REFLECTOR

This chapter shows how a QTR achieves high signal-to-noise ratios (SRNs) when properly locked to a 5.8 GHz external signal.

A QTR amplifies, reflects, and modulates both the RF carrier and the incident noise, which causes a degradation of the SNR that could result in a weak communication link. This phenomenon is similar to the excess noise experienced in a non-regenerative RF repeater transponder of satellite communications. This chapter documents the SNRs of the a tunnel reflector and shows how the prototype achieves high values when properly locked to a 5.8 GHz external input [65]. The QTR prototype mounts tunnel diode model MBD1057-E28X [62] and it can receive, amplify and modulate impinging power levels as low as -85 dBm.

Following the general considerations on the injection locking properties of an oscillator discussed in Sec. 4.1, a study on the SNR of the quantum tunneling reflector prototype is conducted; evidence is provided on how the QTR is affected by 1) the biasing voltages; 2) the RF input signal strength; and 3) the presence of a nearby interference. Achievable modulation speeds and total energy consumption are also reported. Despite the non-linearity of tunnel diodes, the measured SNRs show a linear trend for increasing impinging powers P_t. When properly locked, a reduction of the noise floor occurs causing an increase in the SNR level. Locking is affected by the applied bias voltage and by the external RF signal strength impinging on the device. Gains as high as 25 dB and SNRs above 50 dB have been recorded for biasing voltage of 60.0 mV and input signal strengths below -50 dBm. The prototype can modulate the RF carrier to frequencies as high at 7 MHz, while nearby interference is negligible when the interfering signal is at least 10 MHz away from the main carrier. Finally, the low biasing requirements and the achieved high modulation

speeds result in an energy consumption of only 2.9 pJ/bit.

Contributions of this chapter: a study on the SNR of a QTR has been conducted. In particular, the analysis demonstrates how the SNR of a QTR depends on:

- biasing voltage levels
- RF input signal strengths
- modulation frequencies
- presence of interfering signals

5.1 Oscillations and Locking

A backscattering system is characterized by the radar equation 2.2 [18]; in Table 5.2, the typical link equations discussed in Sec. 2.1 are listed together with the ranges achievable when the values in Table 5.1 are used[1]. A key role is played by the modulation factor M: optimal values of M are 0.5 (-3 dB) and 1 (0 dB) respectively for passive nodes, where part of the impinging RF power is used to power up the circuit logic, and semi-passive nodes, where the circuit logic is powered by a local battery. A properly biased QTR acts as a locking oscillator that can amplify and reflect an impinging external signal. Furthermore, a switching biasing source adds modulation to the reflected signal and generates a modulation factor M greater than one, making the quantum tunneling reflector a valid device to enhance the performances of low powered backscattering communications. In Table 5.1 it is shown how, even when moderate gains of the QTR are considered, the achievable ranges can be four times longer than those of an ideal semi-passive tag: consider a transceiver with a receiving sensitivity of -105 dBm [24], transmitting a 36 dBm signal at 5.8 GHz, and placed at the center of a wireless network. While conventional semi-passive backscattering nodes equipped with omnidirectional antenna dipoles cover an area of maximum 25 meters

[1]The minimum impinging power requirement of P_t = -22.1 dBm applies for UHF tags. In this discussion, it is assumed that the same requirement of P_t applies to 5.8 GHz passive RFID tags.

Table 5.1: Variables and constants of a modulated backscatter link

VAR	Description	Value		
c	Speed of light	$3{\cdot}10^8\ m/s$		
f_{in}	Frequency	5.8 GHz		
λ	Wavelength	5.17 cm		
P_T	Transmitted power	30 dBm		
G_{tx}	Transmitting antenna gain	6 dBi		
G_{rx}	Receiving antenna gain	6 dBi		
G_t	Node antenna gain	2.15 dBi		
P_r	Transceiver sensitivity	-105 dBm [24]		
		Passive	Semi-passive	QTT
P_t	Power on node	-22.1 [14] dBm	-	-55 dBm
M	Modulation factor	-3 dB	0 dB	25 dB

in radius, quantum tunneling reflector nodes, equipped with the same dipole antenna, can modulate, reflect and amplify by 25 dB[2] an impinging RF signal of -55 dBm, outlining a covering area of 105 meters in radius. Nevertheless, if the external signal impinging onto the QTR is too weak, the device does not lock properly and the resulting noise decreases the SNR and affects the quality of the wireless communication link.

5.2 Measuring the SNR of the QTR

As detailed in Sec. 4.1, a properly biased reflector *locks* at the frequency of the RF input signal. The locking range is the maximum difference between the resonant frequency of the oscillator and the injected signal frequency at witch locking occurs:

$$\frac{2\Delta f}{f} = \frac{2}{Q}\sqrt{\frac{P_t}{P_0}} \tag{5.1}$$

with P_0 being the locked power of the RF output. Eq. 5.1 is a function of the external signal amplitude P_t injected onto the device, the oscillator frequency f, and the quality factor Q. Thus, a quantum tunneling reflector can lock onto a broad range of input frequencies Δf.

[2] A conservative gain of 25 dB has been here chosen although higher gains are possible.

Table 5.2: Summary of 5.8 GHz free space link budgets in various basckscattering systems

Forward link $r_f = \frac{\lambda}{4\pi}\sqrt{\frac{P_{tx}}{P_t}G_{tx}G_t}$
Return link $r_r = \frac{\lambda}{4\pi}\sqrt{\frac{P_t}{P_r}G_{rx}G_tM}$
Backscattering link $r_b = \frac{\lambda}{4\pi}G_t\sqrt[4]{\frac{P_T}{P_r}G_{tx}G_{rx}M}$
Max achievable distance $r = \min(r_f, r_r, r_b)$
Range in passive RFID systems $r = r_f$ = 4.2 m
Range in semi-passive RFID systems $r = r_b$ = 25 m
Range in RFID systems with TR $r = r_r$ = 105 m

The experimental setup shown in Fig. 5.1 has been used to investigate what effects 1) the biasing voltages; 2) the external signal strength; and 3) the modulation speed have on the behavior of the QTR: a modulating square wave of amplitude V_{DC} and frequency f_m biases the reflector while a variable attenuator simulates the effect of distances between a transceiver and a quantum tunneling tag (QTT) by modifying the strength of an external 5.8 GHz RF signal P_t injected onto the reflector through a signal generator.

In the following section the causes of proper locking will be outlined and the effects of modulation and interferers shown. The proper locking of the QTR depends on how far the input frequency f_{in} is from the locking range $2\Delta f$ and how weak the locking signal is.

5.2.1 Biasing

When only a biasing voltage and no RF signal is applied on the QTR, the oscillating frequency of the device changes according to the applied DC voltage V_{DC}. As shown in Fig. 5.2, different biasing levels trigger a slightly different oscillating frequency f and the 5.8

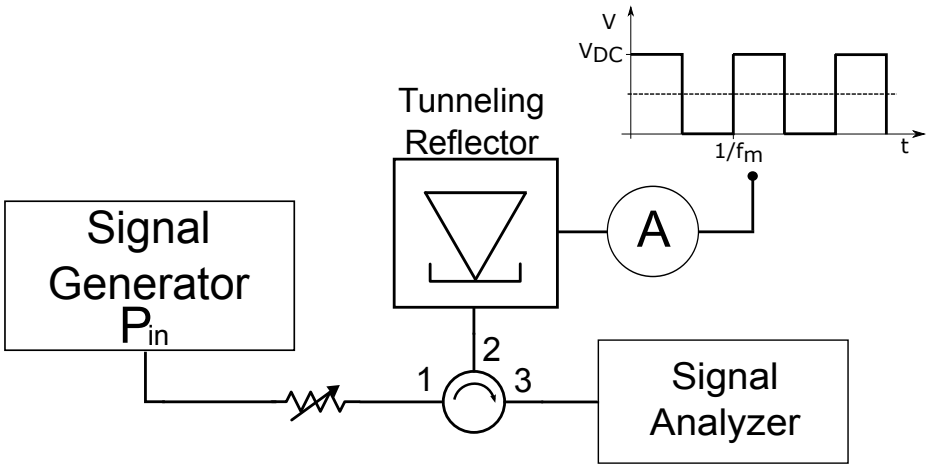

Figure 5.1: Experimental setup: signal generator E8247C, signal analyzer CXA-N9000A with noise figure of 75 dB at 3 kHz resolution bandwidth; 100 kHz video bandwidth; center frequency 5.8 GHz and 100 MHz span on 1001 points. Although the noise figure of the signal analyzer is high, it is overshadowed by the noise introduced through biasing of the tunneling reflector.

GHz tone is excited for V_{DC} = 60.0 mV. Therefore, an input carrier at f_{in} = 5.8 GHz locks the reflector at this frequency if a biasing voltage V_{DC} = 60.0 mV is used.

By biasing the device with a square wave of amplitude $V_{DC} = 60$ mV and frequency f_m = 250 kHz, the 5.8 GHz input carrier is modulated, reflected and amplified. In Fig. 5.3 it is shown how a 5.8 GHz RF carrier of P_t = -55 dBm in strength is reflected, amplified and modulated at 250 kHz and the output power, P_{out}, is compared with the output generated by the device when a constant V_{DC} bias at 60.0 mV and no RF input are applied.

The importance of proper bias voltage V_{DC} on the effect of the SNR is highlighted in Fig. 5.4 where a V_{DC} of 62.5 mV affects the proper locking at the desired frequency. In this case, as the injection carrier is outside the locking range, the SNR degrades although modulation and amplification still take place. Finally, the effects of biasing on the SNR have also been recorded on a backscattering transceiver. The curves in Fig. 5.5 show the measured power spectrum from the in-phase channel respectively when 1) no bias; 2) *constant bias* (V_{DC} = 60.0 mV); and 3) *modulating bias* (V_{DC} = 60.0 mV, f_m = 250 kHz) are applied on the QTR for an external signal strength P_t = -65 dBm. The measurements are based on a time-window of 1 millisecond and a sampling rate of 10 $MSamples/s$.

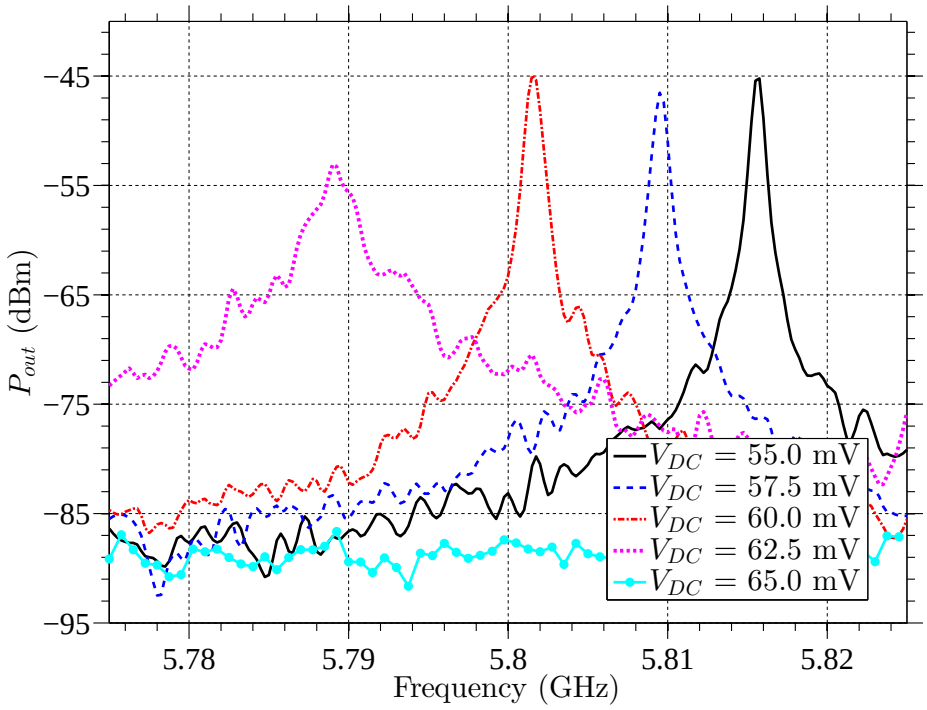

Figure 5.2: Effect of biases on the quantum tunneling reflector recorded over a span of 100 MHz around 5.8 GHz when no RF input is applied.

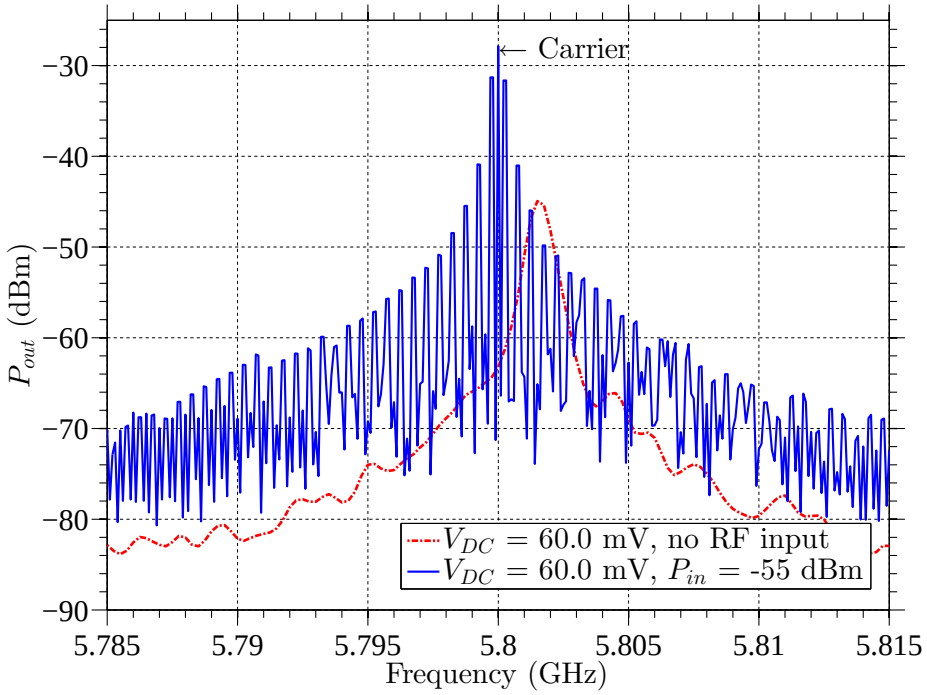

Figure 5.3: Locking of the quantum tunneling reflector for f_{in} = 5.8 GHz, P_t = -55 dBm, f_m = 250 kHz and V_{DC} = 60.0 mV.

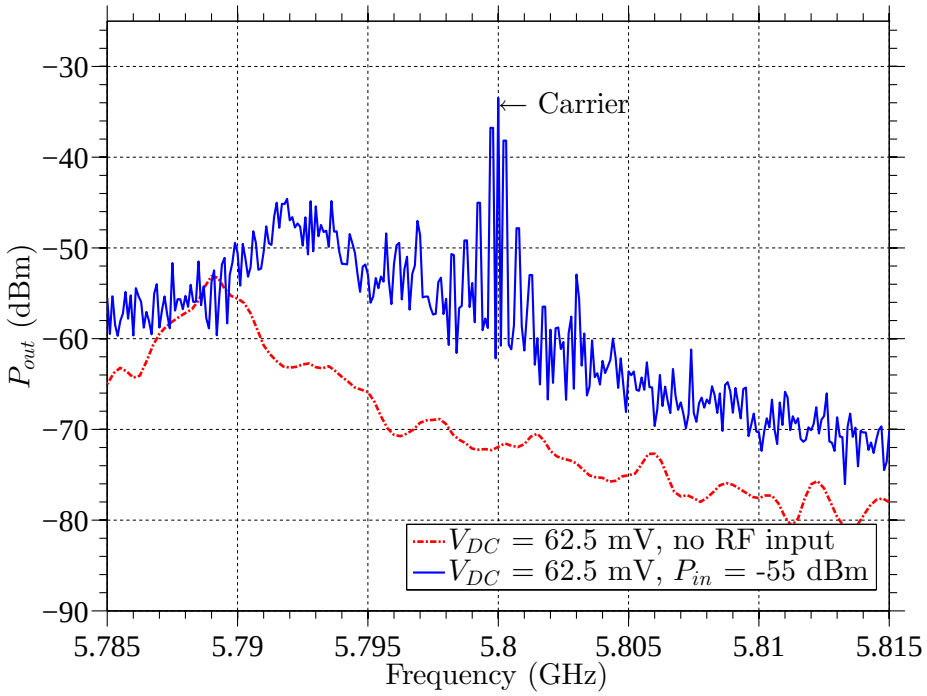

Figure 5.4: Locking of the quantum tunneling reflector for f_{in} = 5.8 GHz, P_t = -55 dBm, f_m = 250 kHz and V_{DC} = 62.5 mV.

The transceiver used to collect the data has a high-pass cut-off frequency of 20 kHz and a low-pass cut-off of 2 MHz. While a *constant bias* voltage and no RF input carrier cause the noise floor to rise by several dB, an injected external input onto the QTR, on which a *modulating bias* is applied, slightly reduces the noise floor level as the effect of locking and the carrier signal is reflected, amplified and modulated.

5.2.2 External Signal Strength

Applying the adequate biasing voltage in a quantum tunneling reflector is necessary for having both a high gain and a proper locking without noise; nevertheless, locking, and therefore noise levels, also depends on the strength of the external signal [60]. In the experimental setup in Fig. 5.1, the variable attenuator has been used to adjust the RF signal strength impinging on the quantum tunneling reflector and the output P_{out} together with the noise floor levels on the signal analyzer have been recorded. Tables 5.3 to 5.7 report the measured tunneling reflector output signals P_{out}, its noise floor and the SNR when external

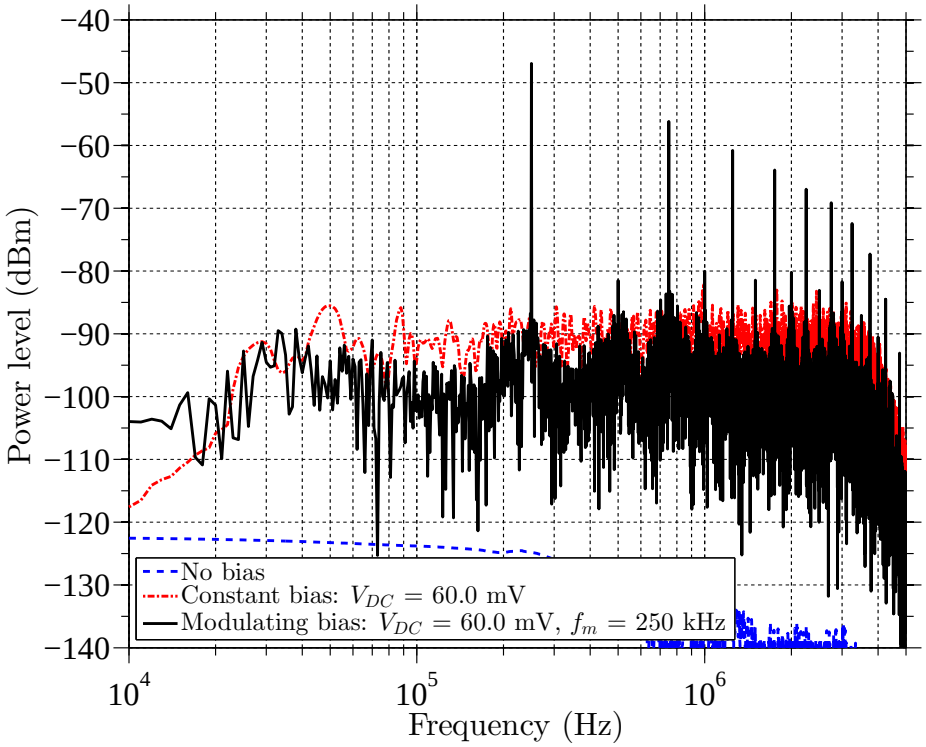

Figure 5.5: Spectrum of 1 millisecond measurement on the in-phase channel of a 5.8 GHz backscattering transceiver. The transmitter is directly connected to the tunneling reflector.

5.8 GHz signals P_t of different strength are applied. Each table lists data obtained for a specific bias level V_{DC} (spanning from 55.0 mV to 65.0 mV, with a step of 2.25 mV) used to generate a square wave with f_m = 250 kHz. Fig. 5.6 gives more insight to these results: despite the non linearity of the quantum tunneling reflector, the relationship between SNRs and the injected signal strength P_t is linear. Moreover, the power levels ranging between -65 dBm and -50 dBm provide SNRs above 40 dB where both modulation gains and reduced noise floor levels take place; SNRs of 10 dB are possible for lower injection signals (P_t = -85 dBm).

5.2.3 Effects of Modulation

By fixing both the 5.8 GHz input signal strength P_t at -55 dBm and the biasing square wave amplitude at 60.0 mV of the experimental setup, the modulating frequency f_m has been changed to identify the locking window of the quantum tunneling reflector. Once locked,

Table 5.3: Bias V_{DC} = 55.0 mV, f_m = 250 kHz

P_t (dBm)	P_{out} (dBm)	Noise Floor (dBm)	SNR (dB)
-50	-46.7	-79.5	32.8
-55	-53.8	-92.7	38.9
-60	-57.1	-89.5	32.4
-65	-64.2	-96.2	32
-70	-66.1	-89.7	23.6
-75	-74.4	-95	20.6
-80	-79.5	-94.8	15.3
-85	-80.5	-94.5	14

Table 5.4: Bias V_{DC} = 57.5 mV, f_m = 250 kHz

P_t (dBm)	P_{out} (dBm)	Noise Floor (dBm)	SNR (dB)
-50	-40.2	-87.1	46.9
-55	-48.2	- 79.3	31.1
-60	-54.7	-87.1	32.4
-65	-62.7	-96.7	34
-70	-62.2	-89.7	27.5
-75	-72.4	-96.3	23.9
-80	-71.4	-89.7	18.3
-85	-82.4	-95.39	13

Table 5.5: Bias V_{DC} = 60.0 mV, f_m = 250 kHz

P_t (dBm)	P_{out} (dBm)	Noise Floor (dBm)	SNR (dB)
-50	-31.4	-89.2	57.8
-55	-31.4	-82	50.6
-60	-47.9	-85.2	37.3
-65	-40.7	-69.9	28.9
-70	-54	-81.7	27.7
-75	-56.4	-77.2	20.8
-80	-62.1	-83.5	21.4
-85	-73	-84.1	11.1

Table 5.6: Bias V_{DC} = 62.5 mV, f_m = 250 kHz

P_t (dBm)	P_{out} (dBm)	Noise Floor (dBm)	SNR (dB)
-50	-32	-85	53
-55	-32.3	-80.1	47.8
-60	-32.6	-67.9	35.4
-65	-39.2	-69.4	30.2
-70	-46.4	-72.4	26
-75	-51.2	-72.2	21
-80	-54.7	-72	17.3
-85	-60	-72.5	12.5

Table 5.7: Bias V_{DC} = 65.0 mV, f_m = 250 kHz

P_t (dBm)	P_{out} (dBm)	Noise Floor (dBm)	SNR (dB)
-50	-47.4	-91.7	44.3
-55	-52.5	-92.7	40.2
-60	-56.3	-92.8	36.5
-65	-60.5	-94	33.5
-70	-65.7	-95.7	30
-75	-67.6	-94.3	26.7
-80	-73.6	-95.1	21.5
-85	-75.6	-94.5	18.9

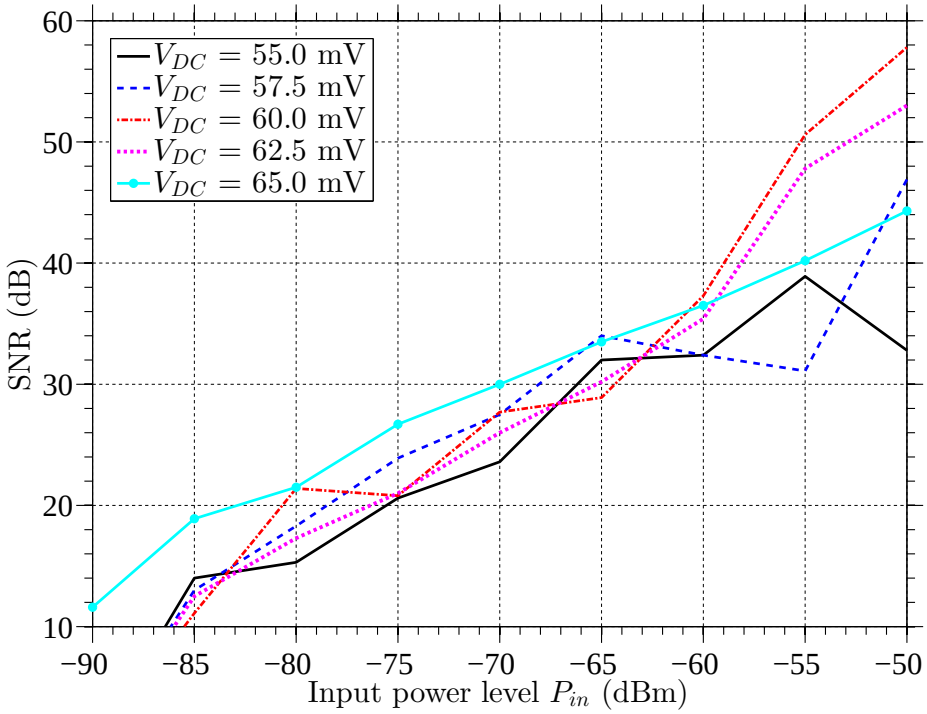

Figure 5.6: SNR as function of the external locking signal P_t for different bias voltages. Best SNRs are obtained for input power levels above -65 dBm at bias levels of 60.0 mV and 62.5 mV.

the tunneling reflector can modulate an external carrier at modulating frequencies ranging from 250 kHz and up to 7 MHz with no, or little, degradation of the SNR. Fig. 5.7 and Fig. 5.8 show the capability of the device to reflect, amplify and modulate an external 5.8 GHz carrier with amplitude P_t = -55 dBm at modulation frequencies of 5 MHz and 7 MHz respectively. A locking window of 14 MHz has been therefore measured; corresponding to a maximum modulating speed of 7 MHz.

5.2.4 Effects of an Interfering Signal

By adding a second signal generator in the experimental setup of Fig. 5.1 and combining the two signals through a combiner, it was possible to study the effects of an interferer whose frequency falls within the locking range. As the quantum tunneling reflector can amplify and modulate any input signal falling in its locking range, an interferer close to the RF input carrier can affect the communication performance. As shown in Fig. 5.9,

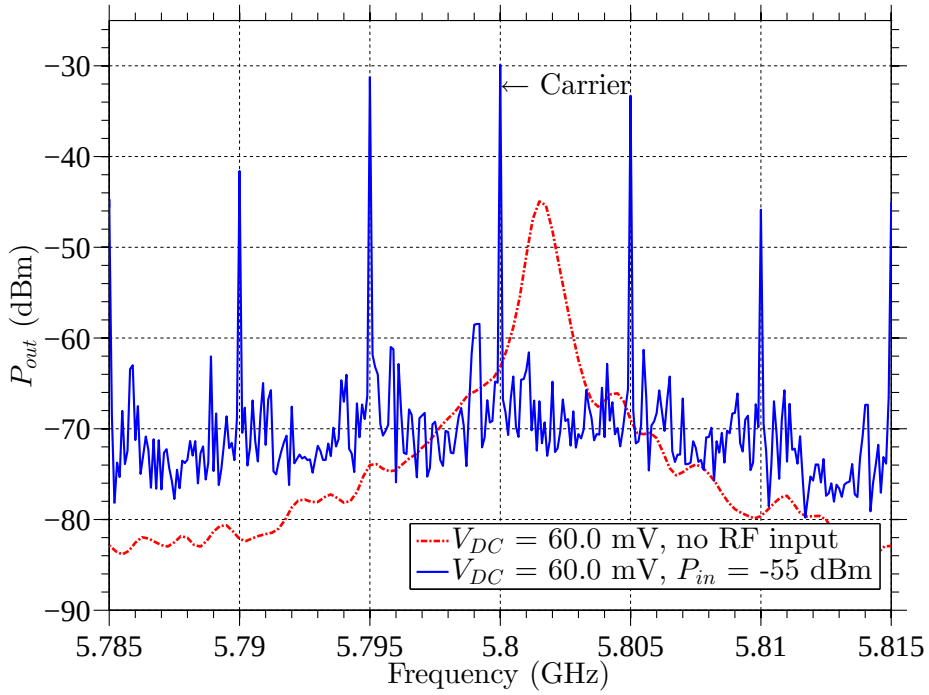

Figure 5.7: Locking of the quantum tunneling reflector for f_{in} = 5.8 GHz, P_t = -55 dBm, f_m = 5 MHz and V_{DC} = 60.0 mV

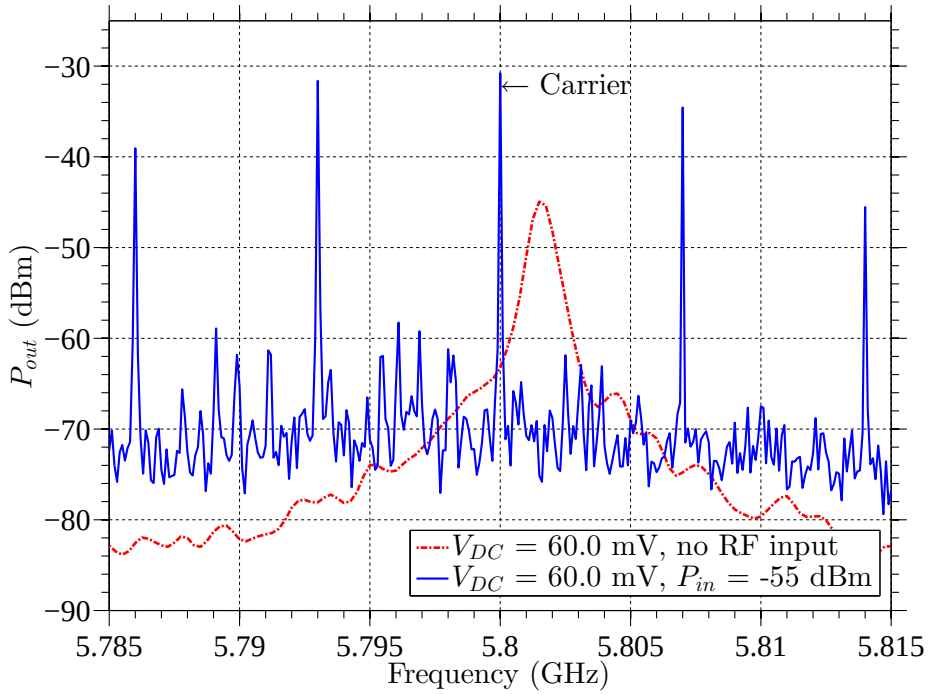

Figure 5.8: Locking of the quantum tunneling reflector for f_{in} = 5.8 GHz, P_t = -55 dBm, f_m = 7 MHz and V_{DC} = 60.0 mV

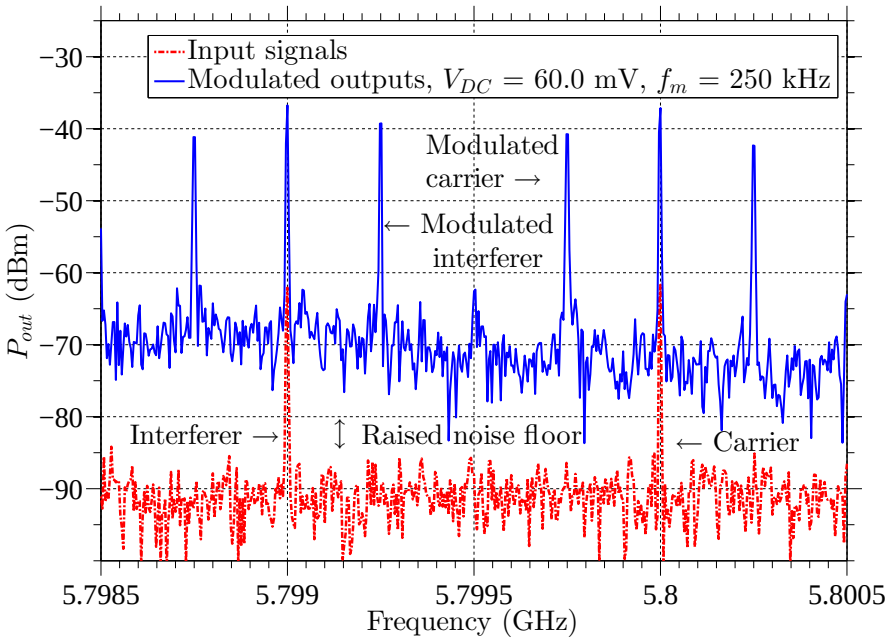

Figure 5.9: Effect of an interferer at 5.799 GHz with same amplitude of the main signal: P_t = -61 dBm.

when an interfering frequency (5.799 GHz) is in close proximity to the carrier frequency (5.8 GHz) and both have the same signal strength (-60 dBm), the interferer is amplified as much as the main carrier causing a possible degradation of the communication link. When the interfering signal is weaker (-82 dBm) than the main carrier (-61 dBm), degradation of the link is alleviated as shown in Fig. 5.10. Within the 14 MHz locking window, both the RF interferer and the main RF carrier can be amplified with the same gains, while less or no amplification is observed when an interfering signal is 100 MHz or 1 GHz away from the main carrier.

5.2.5 Power Consumption

The low energy per bit consumed by the quantum tunneling reflector has also been estimated. The square wave used to bias and modulate data at 5.8 GHz has a DC optimal voltage of 60.0 mV at which corresponds a driving current of 340 μA (20.4 μW) and a

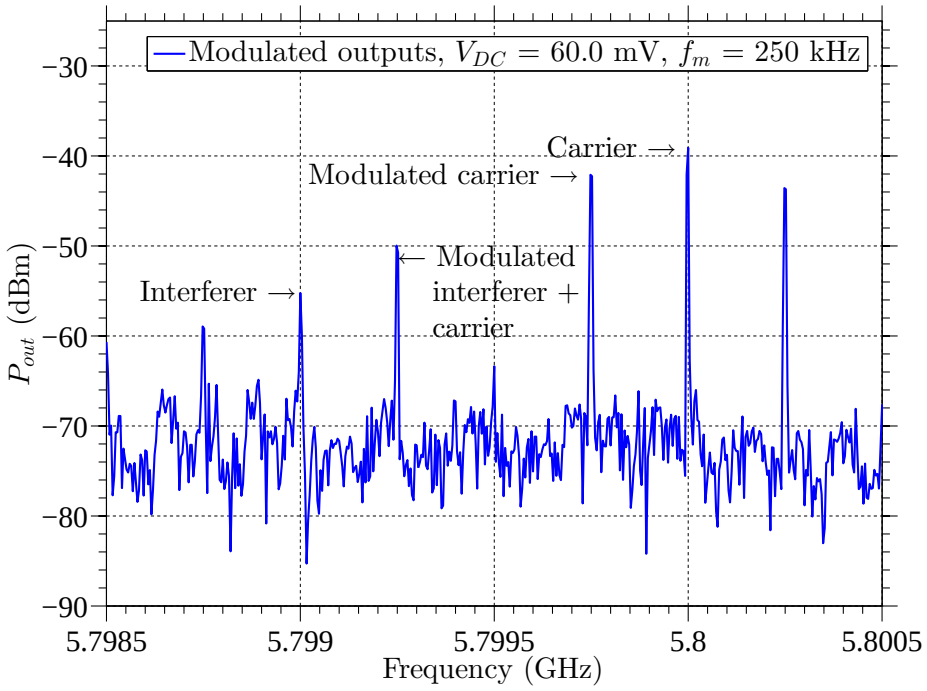

Figure 5.10: Effect of an interferer at 5.799 GHz and -81 dBm amplitude.

modulating frequency f_m as high as 7 MHz. Thus, the total energy consumed per bit is:

$$E = \frac{V_{DC} I_{DC}}{f_m} \tag{5.2}$$

corresponding to a value of 2.9 pJ/bit. The calculated energy per bit of this prototype is much lower than the energy consumption of the transmitter section of the ATMEL SAMB11 BLE chipset whose active transmitting current of 3 mA and voltage of 3.6 V reported in the manufacturer data sheet [3] corresponds to an energy per bit of 10.8 nJ.

5.3 Chapter Conclusions

This chapter explored the benefits, in terms of SNR, of using a quantum tunneling reflector for backscattering applications and investigated the effects of biasing, RF input signal strength, modulation speeds and interferers. The experimental data have shown that a QTR, when properly biased, improves the SNR of a 5.8 GHz modulated backscatter link providing a valid solution for low powered and long range backscattering devices.

High gains and high SNRs (above 50 dB) have been observed for input power levels below -50 dBm and up to -85 dBm. Moreover, modulation frequencies, f_m, up to 7 MHz have been reported. Locking the quantum tunneling reflector to the external RF input signal requires an appropriate bias voltage (V_{DC} = 60.0 mV and current I_{DC} = 340 μA), for a total biasing power P_{DC} = 20.4 μW corresponding to only 2.9 pJ/bit.

CHAPTER 6

BEYOND THE LIMITS OF CLASSIC BACKSCATTERING COMMUNICATIONS

In the previous chapters, the qualities of a quantum tunneling reflector were outlined. Tests on the QTR showed outstanding modulations and amplification capabilities that could revolutionize backscattering communications by achieving long communication ranges with low power consumptions. In this chapter, the results of a field test campaign are shown and discussed.

Contributions of this chapter:

- demonstration, for the first time, of a working long range low powered wireless quantum tunneling tag (QTT);
- modeling of the QTT gain;
- development of a tool to assist system engineers in designing a long range backscattering communication link based on QTTs;
- identified (and designed) scenarios that would benefit from a long range backscattering system;
- collection of experimental results made publicly available for the research community.

6.1 Preliminary Backscattering Tests

A preliminary wireless test was held to verify the long range potential of a backscattering device based on the quantum tunneling effect. A quantum tunneling tag (QTT) was assembled by connecting the quantum tunneling reflector (QTR) to a 5.8 GHz patch antenna of G_t = 6 dBi gain. Differently from a typical backscattering device, the QTT uses a biasing

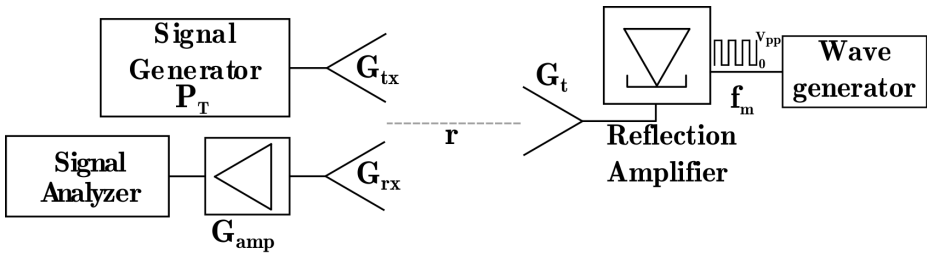

Figure 6.1: Experimental setup to test the wireless capabilities of a quantum tunneling tag. P_T = -20 dBm, G_{tx} = G_t = 6 dBi, G_{rx} = 12 dBi, G_{amp} = 30 dB, r = 23 m, f_m = 250 kHz.

source to modulate the backscattered signal by turning on and off the quantum reflector. The tag was properly biased with a modulating square wave of frequency f_m = 250 kHz and peak voltage V_{pp} as shown in Fig. 6.1. A transceiver was assembled to transmit a 5.8 GHz CW and to receive the backscatter signals: it consists of a signal generator, a transmitting patch antenna with gain G_{tx} = 6 dBi, and a receiving antenna, G_{rx} = 12 dBi connected to a signal analyzer through a 30 dB amplifier.

The transceiver sends a 5.8 GHz CW of -14 dBm EIRP towards the QTT located 23 meters away. The tag detects the attenuated impinging RF signal (P_t = -83 dBm) and backscatters it upon amplification. Despite the expected received power of P_R = -110 dBm, a backscattered signal of -78 dBm appeared at the receiving section of the reader when the modulating biasing voltage was turned on (Fig. 6.2). This results in a 32 dB gain added to the modulated backscattered signal by the quantum tunneling reflector.

These preliminary encouraging results suggested further investigations to verify the backscattering capabilities of the QTT when long ranges are involved. Hence, a new experimental setup was assembled and a field test campaign involving distances up to 1.2 km was held [66].

6.2 Mapping the Scattered Electric Field

An electric signal in the time-domain can be defined as:

$$x(t) = a\cos 2\pi ft - b\sin 2\pi ft \tag{6.1}$$

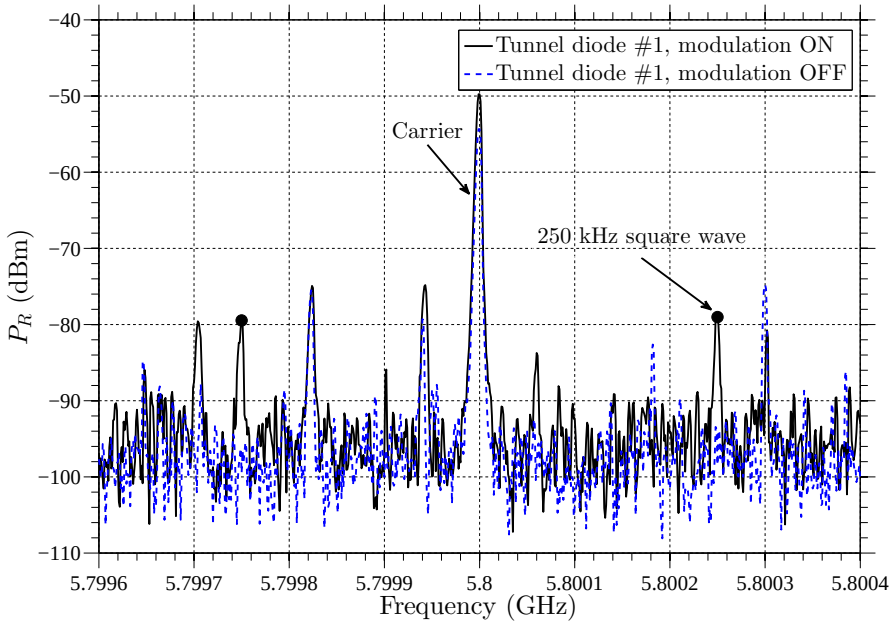

Figure 6.2: Signal backscattered by the quantum tunneling RFID tag and observed at the reader ($r = 23$ m). When the tunnel diode is biased with a 250 kHz square wave ($V_{pp} = 69mV$), peaks at 250 kHz away from the carrier frequency are observed. Other frequencies from other surrounding signals are present when the modulation is turned both ON and OFF.

for a given carrier frequency f, with $\cos()$ and $\sin()$ serving as the in-phase (I) and the quadrature (Q) basis functions respectively. The combination of these basis functions forms the IQ plane and can be used to graphically represent the signal backscattered from an RFID tag towards a receiver.

As shown in Eq. 2.3 in Chapter 2, the modulated, time-varying, backscattered signal of a backscattering node depends on the difference between the reflection coefficients of each impedance state. When a direct-conversion receiver is used (in a static channel), the electromagnetic fields scattered from the transponder antenna back to the receiver are converted to a DC signal while the time-varying signal from the backscattering node oscillates at the modulation rate f_m. The base-band signal at any given time is:

$$V_{bb} = V_{DC} + V, \tag{6.2}$$

where V_{bb} is the received signal in base-band, V_{DC} is the received DC component, and $V = V_I + jV_Q$ is the time-varying signal. The desired, modulated-backscatter signal can be therefore extracted from the total received signal by blocking V_{DC} with a series capacitor.

Since environmental and transceiver noise affect the quality of the wireless link, V can be measured as the average of N bursts received over a period of time:

$$V = \frac{\sum_{n=1}^{N} (V_{I,n} + jV_{Q,n})}{N}, \tag{6.3}$$

with V being the average of all the received V_n vectors ($V_n = V_{I,n} + jV_{Q,n}$). The amplitude of the received symbol V is

$$|V| = \frac{\sum_{n=1}^{N} |V_{I,n} + jV_{Q,n}|}{N} = \frac{\sum_{n=1}^{N} \sqrt{V_{I,n}^2 + V_{Q,n}^2}}{N}. \tag{6.4}$$

The **measured** received power, in dBm, is proportional to the measured voltage V as:

$$\widetilde{P}_r = 10log_{10}\left(\frac{|V|^2}{2R}\right) + 30 \tag{6.5}$$

with R = 50 Ω being the receiver impedance, and $\widetilde{P}_r$ being the measured received power. The symbol $\sim$ will be here used to designate **measured** values (received powers or gains) and to distinguish them from the values calculated through equations.

To measure the signal-to-noise ratio of the backscattering link, the modulation error ratio (MER) was used. It is defined, in dB, as:

$$MER = 10\log_{10}\frac{|V|^2}{|e|^2} \tag{6.6}$$

with $|V|$ being the average of the received symbol as expressed in Eq. 6.4 and $|e|$ being the

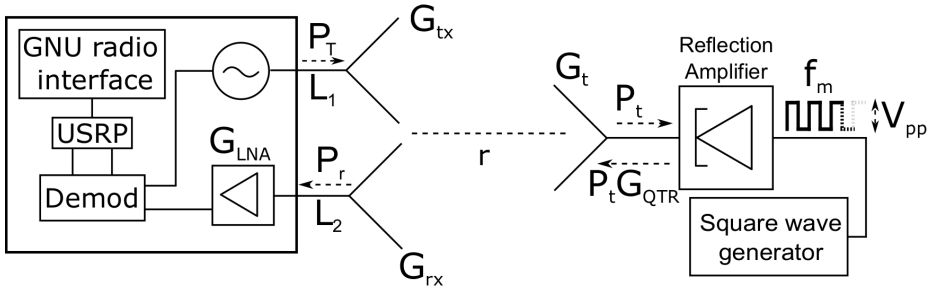

Figure 6.3: Transceiver [18] and tag configuration used to collect the experimental data. Details are listed in Table 6.1. Data are acquired thought the GNU radio interface, saved as **.bin* files and available at [67].

average error magnitude defined as:

$$|e| = \sum_{n=1}^{N} e_n = \frac{1}{N} \sum_{n=1}^{N} \sqrt{(V_I - V_{I,n})^2 + (V_Q - V_{Q,n})^2}. \tag{6.7}$$

By replacing Eq. 6.4 and 6.7 in Eq. 6.6:

$$MER = 20 \log_{10} \left(\frac{\sqrt{V_{I,n}^2 + V_{Q,n}^2}}{\sum_{n=1}^{N} \sqrt{(V_I - V_{I,n})^2 + (V_Q - V_{Q,n})^2}} \right), \tag{6.8}$$

where V_I and V_Q are the in-phase and quadrature average components of the received, demodulated symbol; $V_{I,n}$ and $V_{Q,n}$ are the quadrature components of the received, demodulated n-th symbol and N is the total number or received symbols.

6.3 The Experimental Setup

To test the long range backscattering capabilities of a quantum tunneling tag, the experimental setup in Fig. 6.3 was used. It consists of a 5.8 GHz transceiver and a QTT. The tag was placed at different distances r from the transceiver and backscattering data were collected and post-processed.

6.3.1 The Microwave Transceiver

The fabrication of the 5.8 GHz microwave transceiver available at the Propagation Group Laboratory is documented in [68]. Its transmitting section generates a 5.8 GHz CW of power P_T and it is connected to an antenna of gain G_{tx}. Its receiving section has a high-pass cut-off frequency of 20 kHz and a low-pass cut-off of 2 MHz. The receiver amplifies the backscattered power P_r through an LNA and demodulates the data through a commercially available open-source universal software radio platform (USRP) [69] designed for RF and microwave applications from DC to 6 GHz.

The USRP uses GNU radio free software development tool kit. The flexibility of the platform allows engineers to develop a customized receiver algorithm and communication protocol. The objective of the algorithm is to collect the received backscattered signals.

The receiver samples the data from the ADCs of the USRP and post-process them to extract the necessary information as documented in [70]. The data is recorded at 10 Msps, resulting in a Nyquist frequency of 5 MHz. The base-band data, V_{bb} are filtered and sampled by the analog to digital converter (ADC) and contain the backscattered data $V_{I,n}$ and $V_{Q,n}$ from the QTT. The raw data are stored on a binary **.bin* file which can be read and processed using either MATLAB or GNU Radio.

6.3.2 The Quantum Tunneling Tag - QTT

The QTT consists of a quantum tunneling reflector (QTR) connected to a tag antenna of gain G_t and a waveform generator used to modulate, amplify and backscatter the impinging CW through a biasing square wave of tunable voltage amplitude V_{pp} and frequency f_m. The QTT switches between two states at a constant rate; the square wave can be represented as a Fourier series whose fundamental frequency is f_m and has harmonics at integer multiples of this frequency. Since there is a direct correlation between the amplitude and phase of the square wave and the amplitude and phase of the fundamental frequency sinusoid, it is sufficient to perform matched filtering for the received signal with this sinusoid.

Provided the sample of data is long enough (many periods of the fundamental frequency), matched filtering with a sinusoid is equivalent to finding the Discrete Fourier Transform (DFT) of the received signal at the frequency of interest. In the digital domain, this can be performed efficiently using an FFT, or better yet, a Goertzel filter. The Goertzel filter efficiently computes the DFT at a single frequency of interest. Goertzel filtering is performed on the in-phase (I) and quadrature (Q) channels separately. The magnitude of the signal is then given by Eq. 6.4.

6.3.3 Instrument Calibration

Since V of Eq. 6.3 corresponds to the average voltage measured at the USRP output port, a calibration procedure has been held to retrieve the power $\widetilde{P}_r$ (in dBm) received at the antenna terminals. The calibration procedure identifies the added gains G (in dB) that needs to be removed to measure the correct amount of power $\widetilde{P}_r$ at the antenna terminals. Eq. 6.5 is therefore modified in the following:

$$\widetilde{P}_r = 10log_{10}\left(\frac{|V|^2}{2R}\right) + 30 - G, \tag{6.9}$$

with G being the calibration factor measured during the calibration procedure, and R = 50 Ω being the receiver impedance.

Once the received power is both measured through Eq. 6.9 ($\widetilde{P}_r$), and estimated through the link budget equation 2.2[1] (P_r), the gain $\widetilde{G}_{QTR}$ can also be measured:

$$\widetilde{G}_{QTR} = 10log_{10}\frac{\widetilde{P}_r}{P_r} \tag{6.10}$$

[1] In Eq. 2.2, it is assumed that no gain is added by the QTT (M = 1).

6.3.4 The Field Test Campaign

Tests were conducted by varying the distances r between the transceiver and the QTT; for each distance, different biases voltages V_{pp} were tested for two or more modulation speeds f_m. For this work, three different experimental setups were used; Setup I is characterized by a CW with P_T of only 0 dBm (1 mW) and an EIRP of 6 dBm (4 mW). It was used to test the QTT backscattering capabilities for distances r between 25 m and 160 m. Setup II and III, both transmitting CW of 22 dBm (158 mW) and EIRP of 28 dBm (0.63 W), were used to test the QTT when located at 650 m and 1.2 km respectively.

An overview of the parameters characterizing the three setups is shown in Table 6.1. All the *.bin* files collected during the measurement campaign are made publicly available at the Github repository [67][2] for scrutiny and free use by other researchers (See Appendix A).

Table 6.1: Configurations of the Experimental Setups

	Setup I	Setup II	Setup III
P_T (dBm)	0	22	22
G_{tx} (dBi)	6		
G_{rx} (dBi)	24		
G_t (dBi)	6		24
G (dB)	15	30	30
L_1 (dB)	1.2		
L_2 (dB)	0.9		

6.4 Achieved Ranges and Gains of the Quantum Tunneling Tag

The preliminary experimental results of Sec. 6.1 and the foreseen results of Fig. 4.15 allowed to plan a measurement campaign aimed to experimentally verify the capabilities of a QTT in terms of achievable ranges. Fig. 6.4 and Table 6.2 summarize and show the distances involved during the testing phase.

[2] currently a private repository, it will become public upon acceptance of submitted papers

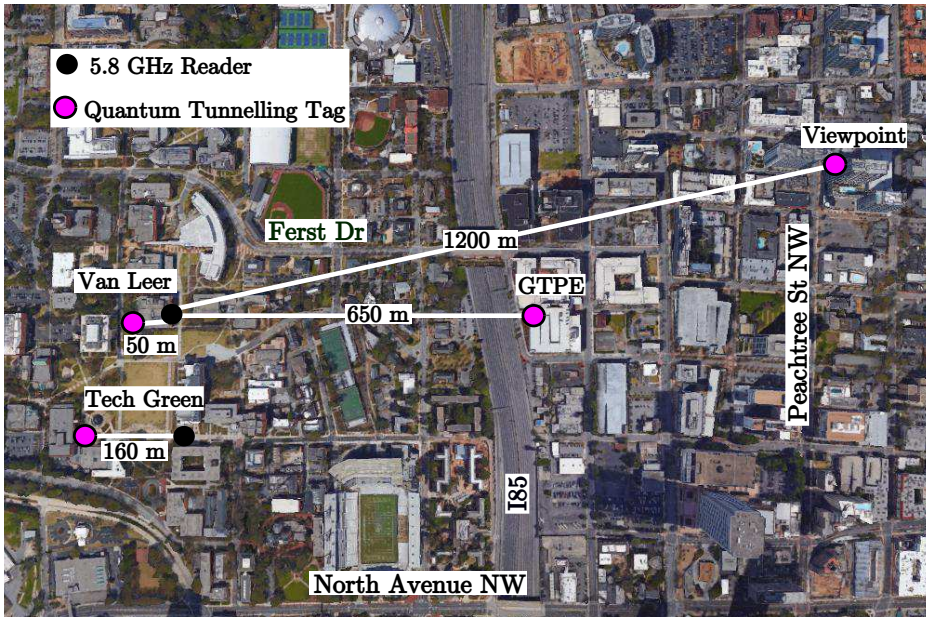

Figure 6.4: Satellite view of the Georgia Tech campus and the Midtown neighborhood in Atlanta, GA showing locations and distances covered during the field measurement campaign conducted and described in this work.

Table 6.2: Field campaign measurements spots.

Locations	Distance (m)
Van Leer, roof top (Fig. 6.5a)	25 to 50
Tech Green (Fig. 6.5b)	70 to 160
GTPE, parking lot (Fig. 6.5c)	650
Viewpoint, Midtown	1200

(a)

(b)

(c)

Figure 6.5: Experimental setup locations to test long distance capabilities of the quantum tunneling tag. a) Van Leer; b) Tech Green; c) parking lot of the Georgia Tech Professional Education (GTPE).

Setup I, characterized by a transmitting power P_T of only 0 dBm and a total EIRP of 6 dBm, was used to test the QTT communication capabilities up to 160 m. At the *Van Leer* site, the QTT was placed at distances r ranging from 25 m to 50 m; while on the *Tech Green* site, it was placed at distances r of 70 m, 100 m and 160 m. For each distance r, the QTT was modulated with different bias voltages V_{pp} (from 60 mV to 68 mV) and at the modulating speeds f_m of 250 kHz and 1 MHz respectively. The fixed transceiver collected and stored the data backscattered by the QTT. For each test, the demodulated complex data $V_n = V_{I,n} + jV_{Q,n}$ were stored as *.bin* files and post-processed in MATLAB to calculate the average value $|V|$ (Eq. 6.3) and the received power $\widetilde{P}_r$ (Eq. 6.9).

Figs. 6.6, 6.7 and 6.8 display the symbol constellations on the IQ plots when the QTT is located at different distances r from the transceiver and modulates at 250 kHz and 1 MHz respectively. The transceiver noise level is also shown. It is important to highlight that the acquisition algorithm used for these measurements was developed for different purposes [70] where one half plane of the plotted IQ diagrams was added for illustration purposes by mirroring the other half. For this work, we have focused our attention on only one half of the IQ plane and the calibration procedure mentioned in Sec. 6.3.3 has been used to compensate for the missing half.

The collected *.bin* files were processed to retrieve, through Eq. 6.9, the effective measured powers $\widetilde{P}_r$ at the ends of the receiving antenna. Their values are shown in Fig. 6.9 for different biases V_{pp} at 250 kHz and 1 MHz and compared with the received power P_r that would have been backscattered by an ideal semi-passive RFID tag (M = 1) not equipped with any QTR. It is evident that the quantum tunneling tag performs particularly well when it is far away from the transmitter allowing communications at distances nowadays not yet possible for a backscattering technology. Better gains are observed for biasing voltages as low as 60 mV at which corresponds a current of 340 μA. The values in Table 6.3 highlight, for some of the involved distances, the differences between the expected received power P_r when no QTT is used, and the effective measured power $\widetilde{P}_r$ whose high values are due to

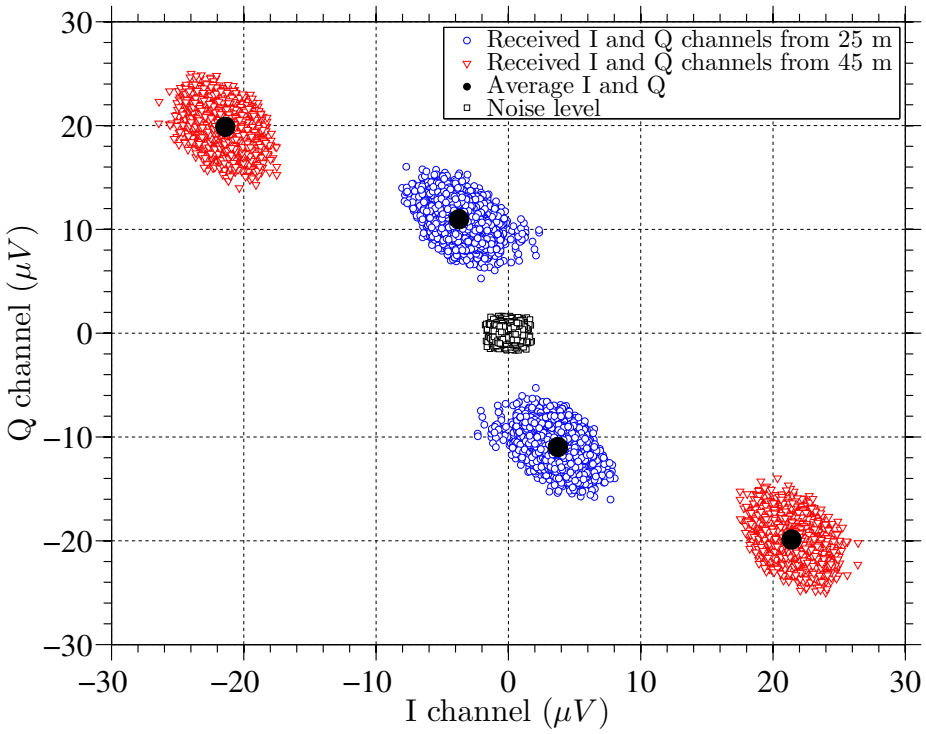

Figure 6.6: IQ diagrams for the received base-band backscattered signals on Setup I. V_{pp} = 60 mV, f_m = 250 kHz, r = 25 and 45 m.

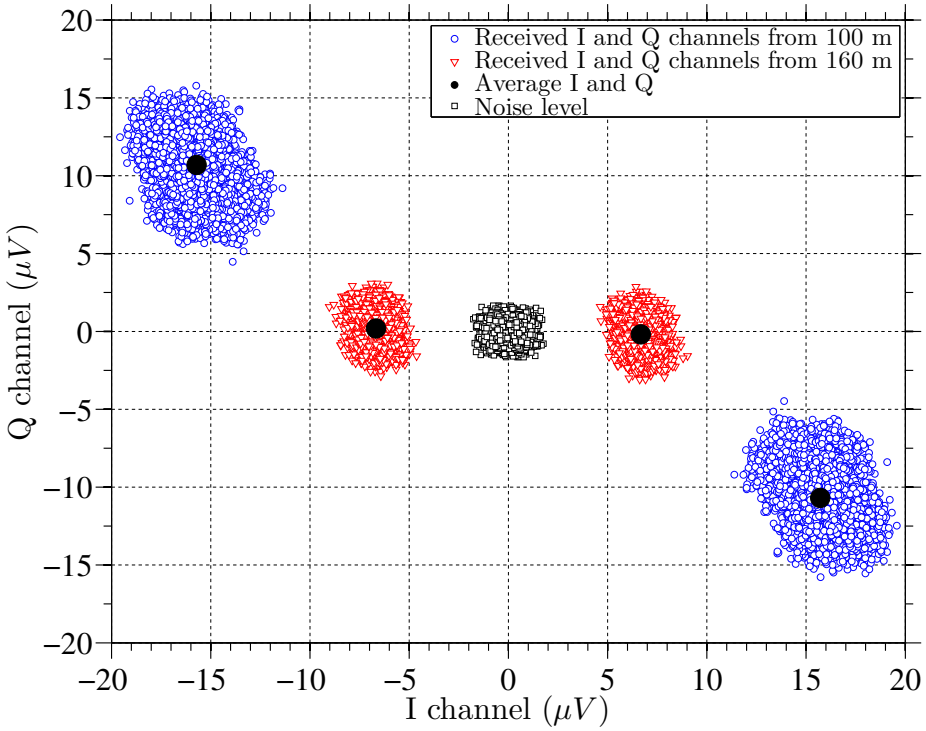

Figure 6.7: IQ diagrams for the received base-band backscattered signals on Setup I. V_{pp} = 60 mV, f_m = 250 kHz, r = 100 and 160 m.

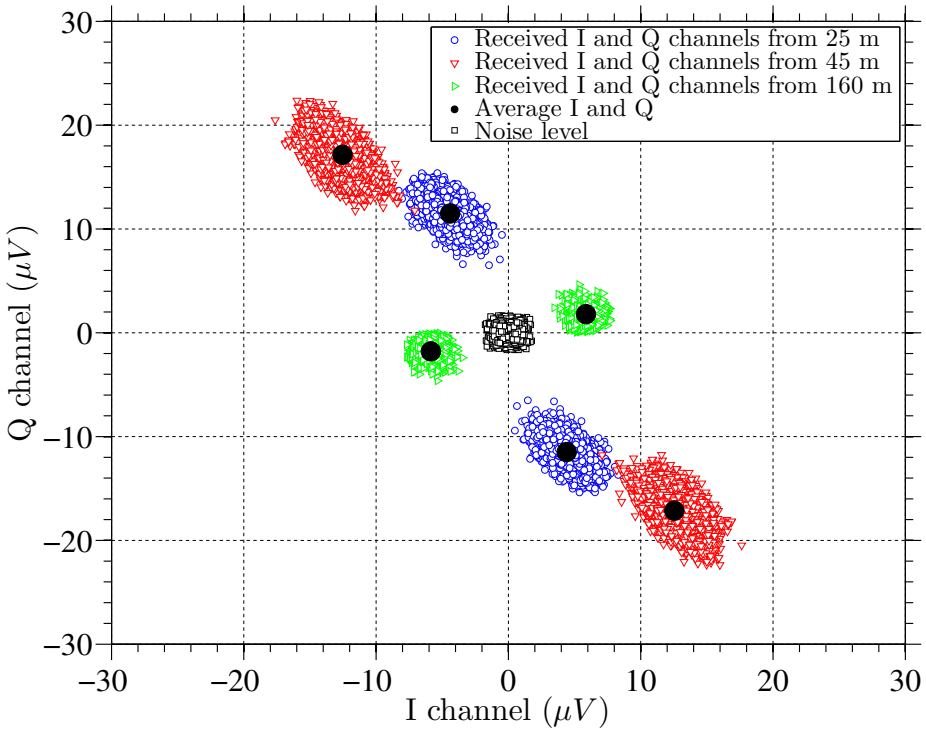

Figure 6.8: IQ diagrams for the received base-band backscattered signals on Setup I. V_{pp} = 60 mV, f_m = 1 MHz, r = 25, 45 and 160 m.

the gains $\widetilde{G}_{QTR}$.

Table 6.3: Measured received powers and gains

	Distance (m)					
	35	50	70	100	160	
P_t (dBm)	-67.8	-70.9	-73.8	-76.9	-81	
P_r (dBm)	-117.3	-123.5	-129.3	-135.5	-143.7	
$\widetilde{P}_r$ (dBm)	-105.4	-104.6	-98.7	-99.4	-108.5	250 kHz
	-105.5	-104.5	-99.1	-103.3	-109.2	1 MHz
$\widetilde{G}_{QTR}$ (dB)	11.8	18.9	30.6	36.1	35.2	250 kHz
	11.7	18.95	30.2	32.5	34.4	1 MHz

By comparing the measured received power $\widetilde{P}_r$ and the power P_r expected by an ideal semi-passive tag, it is possible to measure the gain of the quantum tunneling tag $\widetilde{G}_{QTR}$ (Eq. 6.10). Through Eq. 2.1, the powers P_t impinging on the QTR were estimated and the $\widetilde{G}_{QTR}$ as function of P_t is shown in Fig. 6.10.

The data points obtained through the measurements campaign involving distance r be-

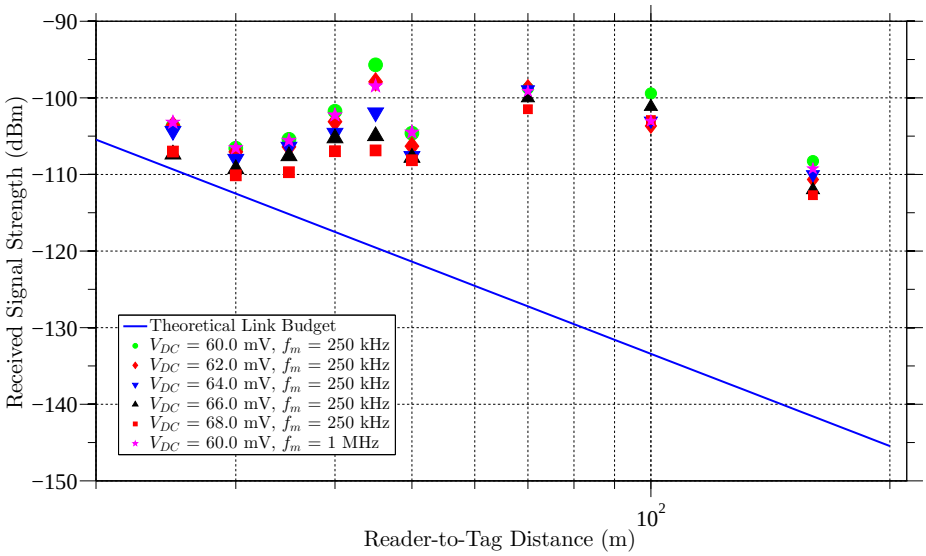

Figure 6.9: Received signal strengths $\widetilde{P}_r$ as function of distances r, biasing voltages V_{pp} and modulation speeds f_m using Setup I (6 dBm EIRP). Results are compared with an ideal semi-passive link (M = 1 and no quantum tunneling reflector) using the same configurations as in Setup I.

tween 25 m ant 160 m were used to extrapolate a mathematical model that best describes the QTR gains, G_{QTR}, for powers ranging between -80 dBm and -55 dBm:

$$G_{QTR} = a_1 e^{-\frac{(x-b_1)^2}{c_1}} + d_1 \tag{6.11}$$

with the coefficients $a_1 = 34.63$; $b_1 = -78.24$; $c_1 = 93.67$; $d_1 = 4$; and x being the power P_t, in dBm, impinging on the QTR. The constant d_1 compensates for the rapid decay of the expression for input powers above -60 dBm. In Fig. 6.10, both the experimental gains and the trend of Eq. 6.11 are compared; the abrupt increase of the QTR gain at low RF impinging powers can be identified.

6.5 Gain Model Validation and Modulation Errors

Setup II and III described in Tab. 6.1 were used to test the QTT modulation at a distance respectively of 650 m and 1.2 km from the transceiver. The received power $\widetilde{P}_r$ were extrapolated from the saved *.*bin* files and the gains $\widetilde{G}_{QTR}$ were retrieved through Eq. 6.10.

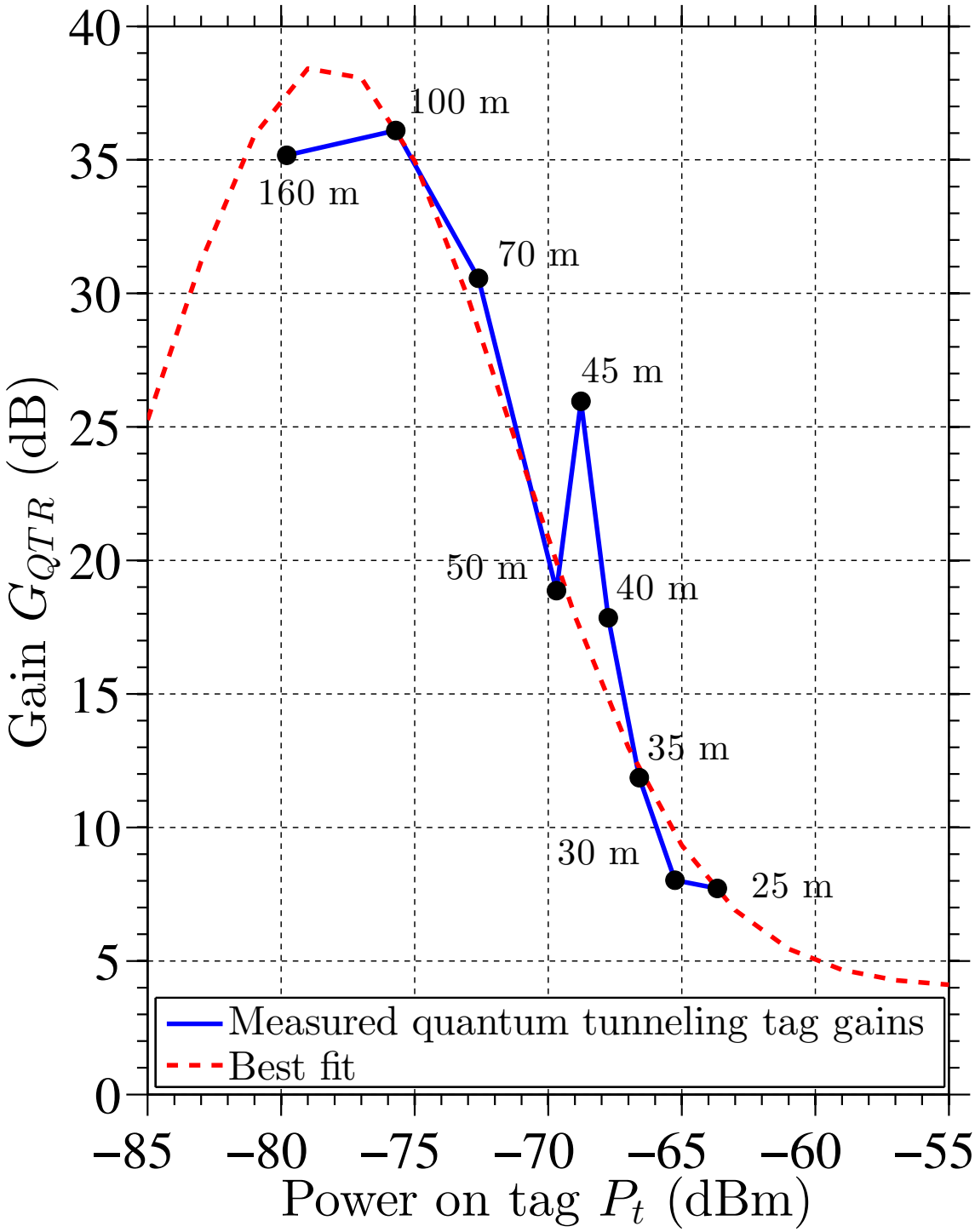

Figure 6.10: Comparing the measured quantum tunneling reflector gains, $\widetilde{G}_{QTR}$, with the gain model G_{QTR} expressed through Eq. 6.11 (valid for RF power on tag values P_t ranging between -80 dBm and -55 dBm).

The G_{QTR} gains were also computed through the mathematical model introduced in Eq. 6.11. Table 6.4 compares the gains and received powers both measured and estimated; the accuracy of the mathematical model in predicting the QTR gains is evident.

Table 6.4: Comparing gains: measures *vs* modeling

	Distance (m)	
	650	1200
1-way Path Loss (dB)	-67.8	-70.9
P_t (dBm)	-71.2	-58.5
$\widetilde{P}_r$ (dBm)	-121.8	-116.5
G_{QTR} (dB)	24.3	4.53
$\widetilde{G}_{QTR}$ (dB)	24.2	4.2

Finally, the MER defined in Eq. 6.6 was used to estimate the SNR of the communication link between the transceiver and the QTT; as shown in Fig. 6.13, this ratio is always above 10 dB.

6.6 A Link Budget Designer Tool

The successful measurement campaign described in the previous sections provided a valuable data set that both demonstrated the capabilities of a quantum tunneling RFID tag in achieving long communication ranges at 5.8 GHz, and allowed to develop a tool to assist a system engineer in designing free-space long-range backscattering communication link.

The tool was developed in MATLAB and it incorporates the QTT gain model of Eq. 6.11; its source code is available for use, test and improvement on Github [67]. A system engineer can set the desired link ranges and frequencies as input; the tool provides the required system variables that can establish the desired link when a quantum tunneling tag is used. Four system variables were identified as listed in Table 6.5. The tool selects all the possible combinations of the system parameters that would make the backscattering link possible.

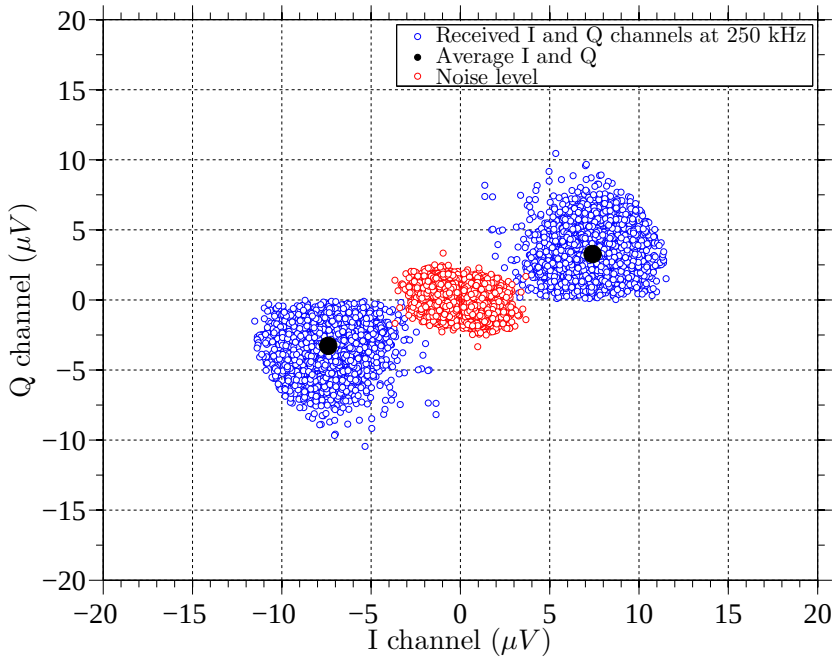

(a)

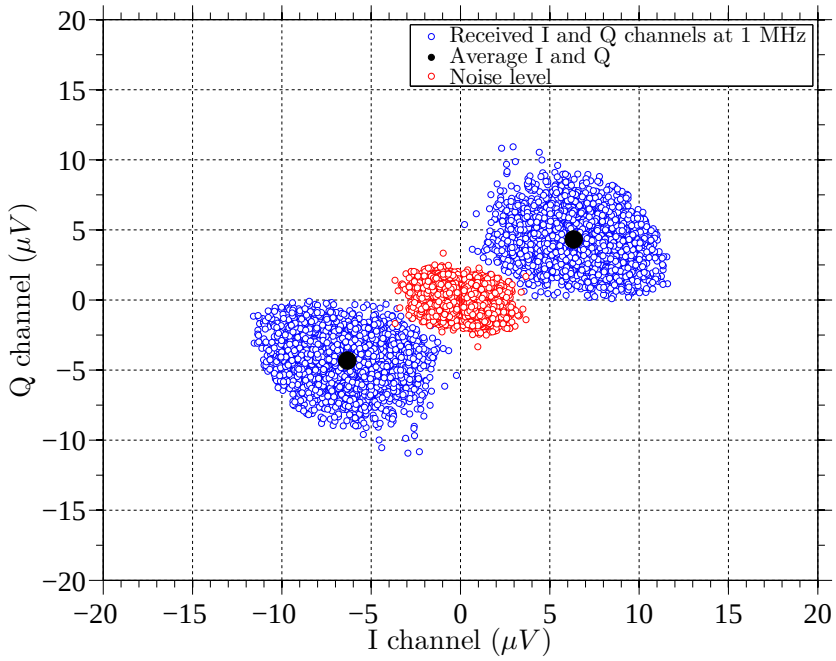

(b)

Figure 6.11: IQ diagrams for the received base-band backscattered signals on Setup II. V_{pp} = 60 mV, r = 650 m. a) f_m = 250 kHz; b) f_m = 1 MHz.

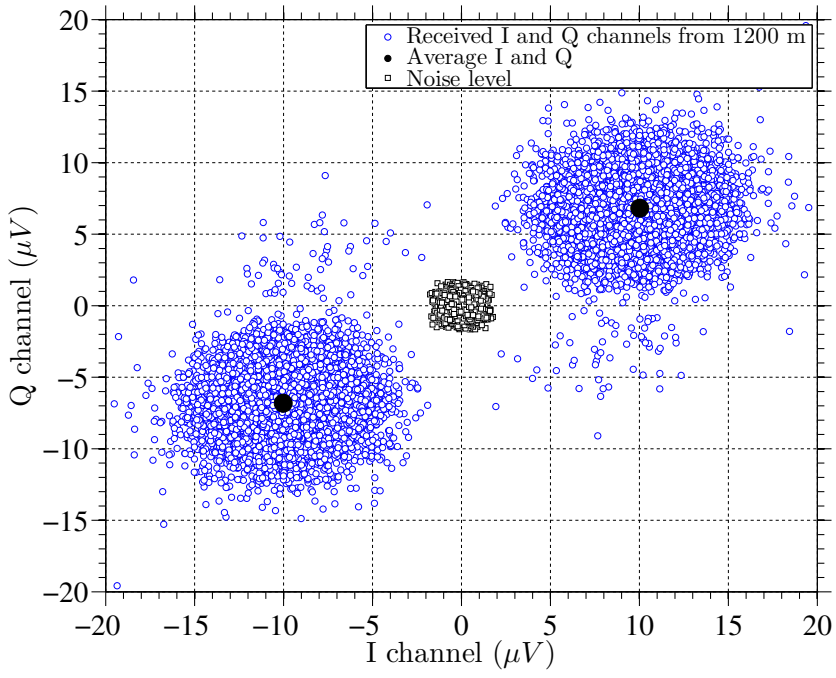

(a)

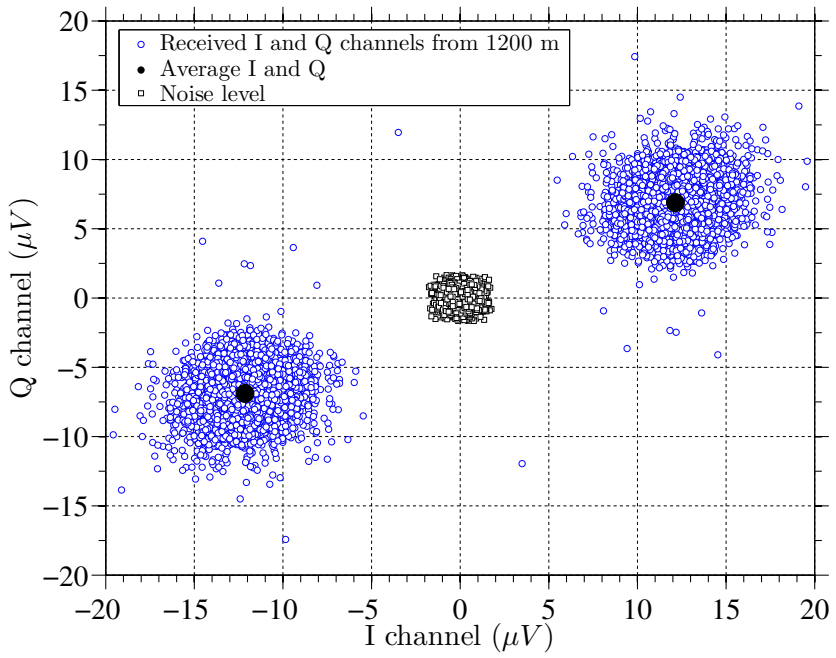

(b)

Figure 6.12: IQ diagrams for the received base-band backscattered signals on Setup III. V_{pp} = 60 mV, r = 1200 m. a) f_m = 1 MHz; b) f_m = 1.77 MHz.

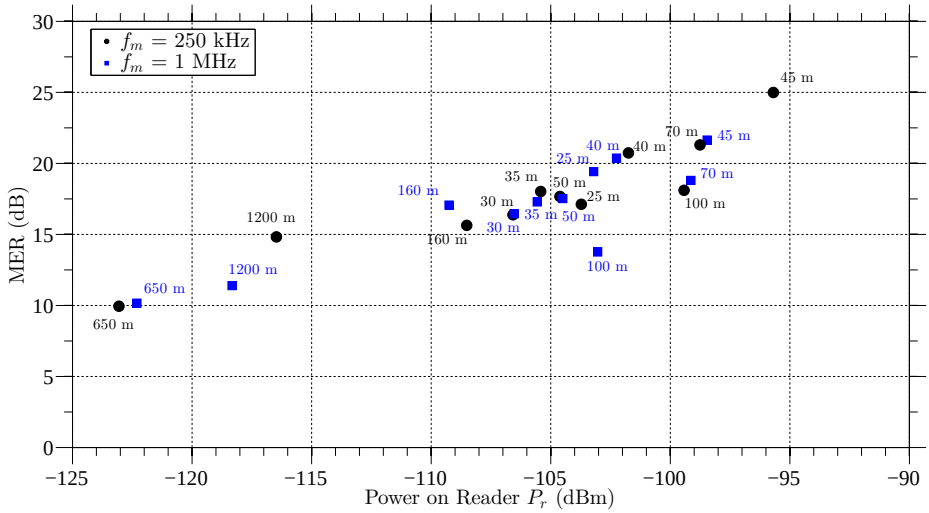

Figure 6.13: Modulation Error Ratios (MER) for each test of the measurement campaign.

Table 6.5: System variables of a backscattering communication link

Variable	Description	Ranges
P_T	Reader transmitted power	[-20, 30] (dBm)
G_{tx}	Reader transmitting antenna gain	[0, 6] (dBi)
G_{rx}	Reader receiving antenna gain	[0, 30] (dBi)
G_t	Quantum tunneling tag antenna gain	[1.76, 14] (dBi)

6.6.1 Testing Scenarios

To test the tool and to have an overview of the basckattering system requirements, several scenarios that would benefit from the use of a long range backscattering link were identified and listed in Table 6.6. On a football field, players wearing QTTs can be monitored by a transceiver suspended at the center of the field; QTTs on commercial products in a warehouse can assist employees (or drones) to quickly locate them for shipment; long range and low powered RFID tags would improve the efficiency and the flexibility of current and future precision agriculture applications suffering of poor technical solutions currently available. People, airplanes and vehicles could be easily monitored in airports, university campuses and cities. For every chosen scenario, the design tool was used to identify the best solutions.

Table 6.6: IoT scenarios for free space long range backscattering applications

Scenario	Est. Radius
Town House	20 m
Football field	50 m
Warehouse (e.g.: Amazon)	100 m
Skyscraper (e. g.: Empire State Building)	300 m
University campus (e. g.: Georgia Tech)	700 m
Crop field	1 km
Airport	1.5 km
City	2 km

6.6.2 Long Range Backscattering - Bistatic Configuration

In Table 6.7, the required design parameters are listed when a *co-located bistatic*[3] transceiver is used. The listed results were chosen among various possibilities using the following criteria: preferences were given to tag antennas with the lowest gains G_t (a short dipole 1.8 dBi; a half wave dipole 2.1 dBi; or a patch antenna 9 dBi) in order to reduce the tag size; a dipole was preferred as the transceiver transmitting antenna for its omnidirectional pattern that allows an uniform coverage of the entire area of interest; finally, a low transmitting power P_T was preferred to reduce the power consumption of the transceiver. Up to 300 m, the QTT requires a half wave dipole, while between 300 m and 1.5 km, a patch antenna would be enough to establish the link. The highest required transmitting power P_T is 21.4 dBm, about 8 dBm below the maximum power of 30 dBm allowed by the FCC regulations [23]. Finally, at 2 km, a higher gain antenna (11.7 dBi) is required on the tag. It is important to highlight that, for the longest range scenarios (university campus, crop field, airport and city), the use of more directive antennas would limit the coverage to 180-degree (or less) and therefore more than one receiving antenna on the transceiver might be required for a 360-degree coverage.

Figs. 6.14, 6.15, and 6.16 highlight the advantages of using a quantum tunneling tag ($M = G_{QTR}$) versus an ideal semi-passive tag ($M = 1$) for three free space scenarios (foot-

[3] A co-located bistatic configuration consists in using a transceiver with two distinct but close-by antennas for transmission and reception.

Table 6.7: Required system parameters for the scenarios listed in Table 6.6 when using a 5.8 GHz co-located bistatic transceiver

Location	EIRP (dBm)	P_T (dBm)	G_{tx} (dBi)	G_{rx} (dBi)	G_t (dBi)
Town house (20 m)	-7.8	-9.6	1.8	5	1.8
Football field (50 m)	0.8	-1	1.8	12	1.8
Warehouse (100 m)	7.7	5.9	1.8	19	1.8
Skyscraper (300 m)	16.8	15	1.8	28	1.8
University Campus (700 m)	16.3	14.5	1.8	28	9
Crop field (1 km)	19.7	17.9	1.8	31.5	9
Airport (1.5 km)	23.2	21.4	1.8	35	9
City (2 km)	23.2	21.4	1.8	35	11.7

ball field, university campus and city) when the backscattering link parameters of Table 6.7 and a transceiver with -110 dBm receiving sensitivity are used. In all cases, a range improvement of 1 order of magnitude can be observed.

The entire free space coverage of all listed scenarios is finally summarized in Fig. 6.17 for bistatic transceiver configurations having a receiving sensitivity of -110 dBm. It is important to stress out that, since the QTT model was proven to be valid for impinging RF powers, P_t, ranging between -55 dBm and -80 dBm, only distances at which correspond these power levels were taken into account. The benefit of a quantum tunneling tag is here evident: the added gain of the quantum tunneling reflector allows a significant range extension in scenarios where the use of 5.8 GHz backscattering communication would not be otherwise possible.

6.6.3 Long Range Backscattering - Monostatic Configuration

The designer tool also helps to identify the necessary system parameters when a monostatic transceiver ($G_{tx} = G_{rx} = G_x$) is available. Among the possible solutions, the ones requiring the lowest transmitting powers P_T were preferred. In this case, although all the scenarios are possible, the transceiver antenna requires a certain directivity that could affect a 360 degrees coverage of the system (Table 6.8). Another configuration could consist in using a transceiver antenna with lower gain (G_x) and a tag antenna with higher gain G_t

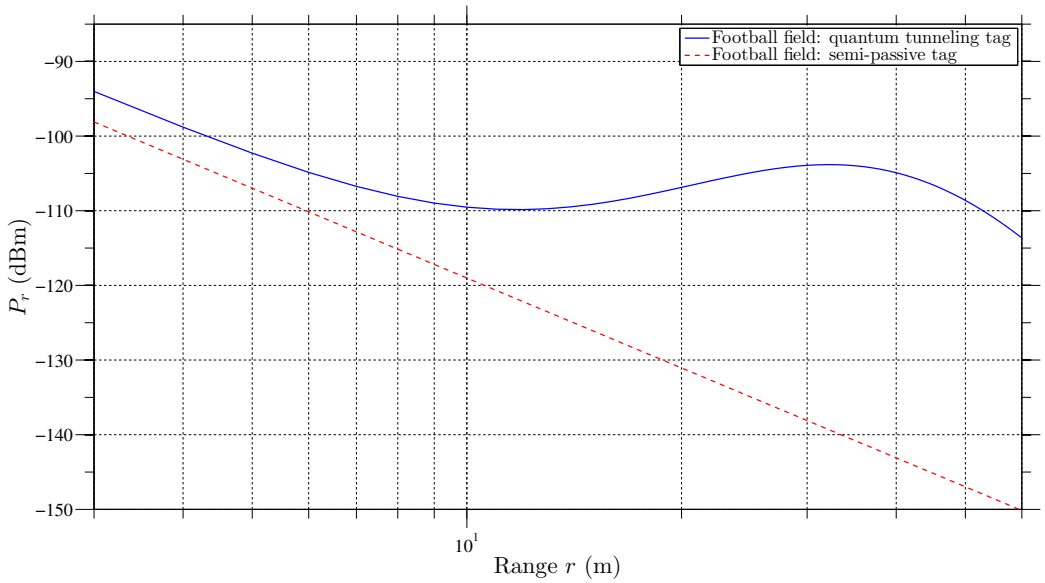

Figure 6.14: Comparing a 5.8 GHz backscattering link of 50 meter radius when an ideal semi-passive (M = 1) and a quantum tunneling tag ($M = G_{QTR}$) are used. Bistatic configuration, free space, and a -110 dBm receiving sensitivity are assumed.

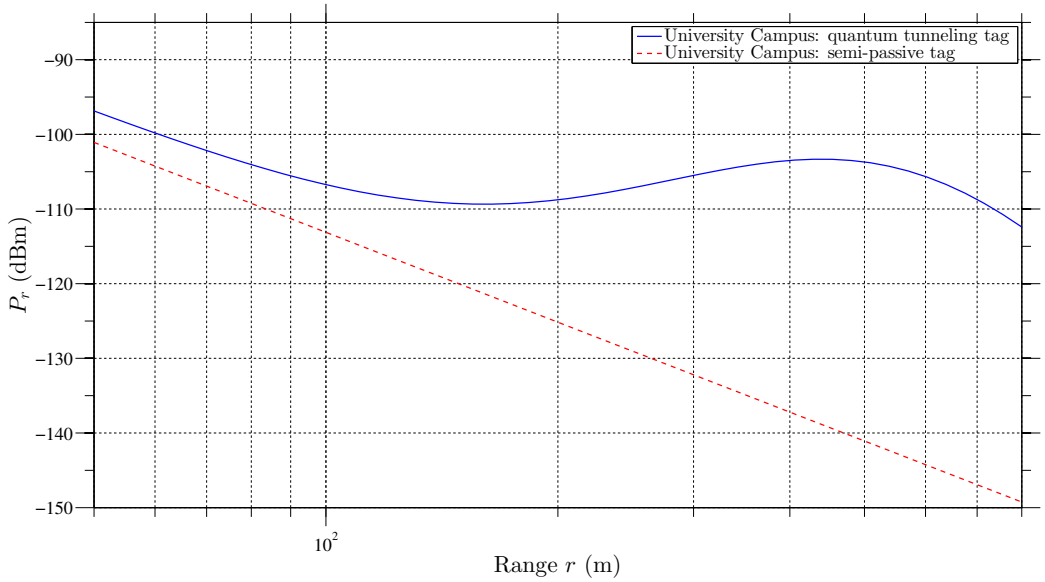

Figure 6.15: Comparing a 5.8 GHz backscattering link of 700 meter radius when an ideal semi-passive (M = 1) and a quantum tunneling tag ($M = G_{QTR}$) are used. Bistatic configuration, free space, and a -110 dBm receiving sensitivity are assumed.

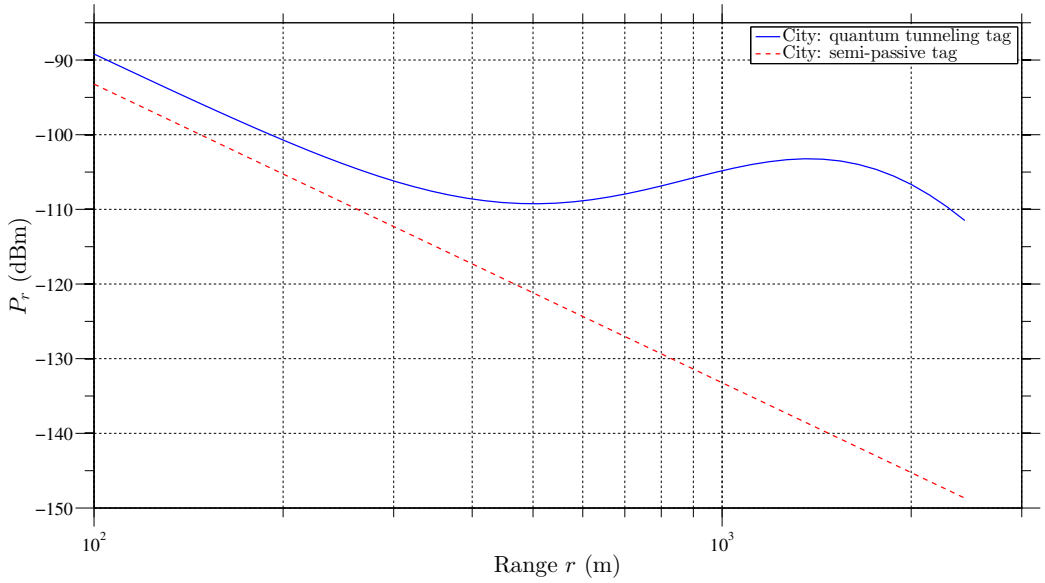

Figure 6.16: Comparing a 5.8 GHz backscattering link of 2000 meter radius when an ideal semi-passive (M = 1) and a quantum tunneling tag ($M = G_{QTR}$) are used. Bistatic configuration, free space, and a -110 dBm receiving sensitivity are assumed.

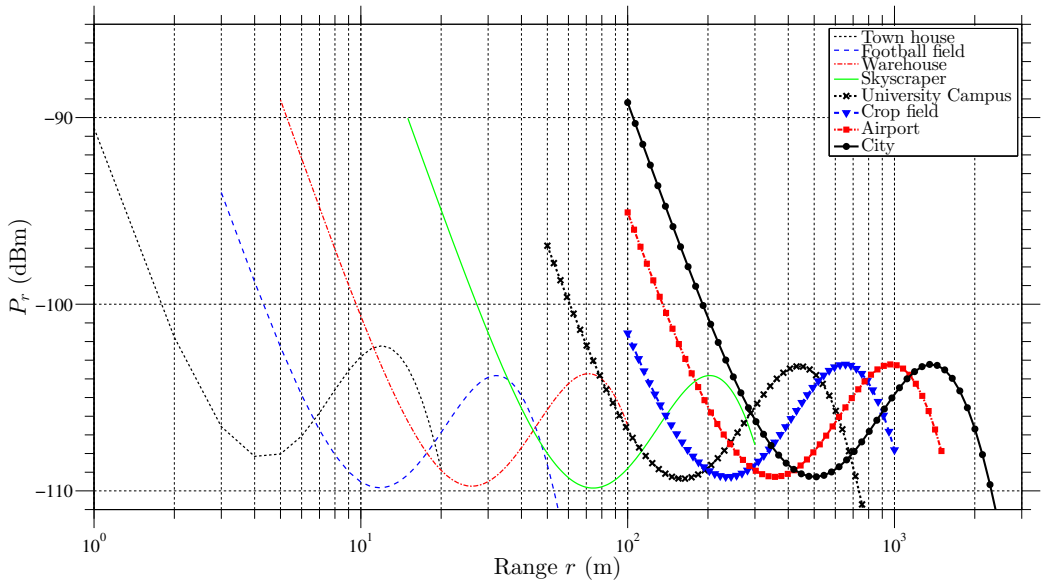

Figure 6.17: Whole coverage of different scenarios for the bistatic case, assuming free space and a -110 dBm receiving sensitivity.

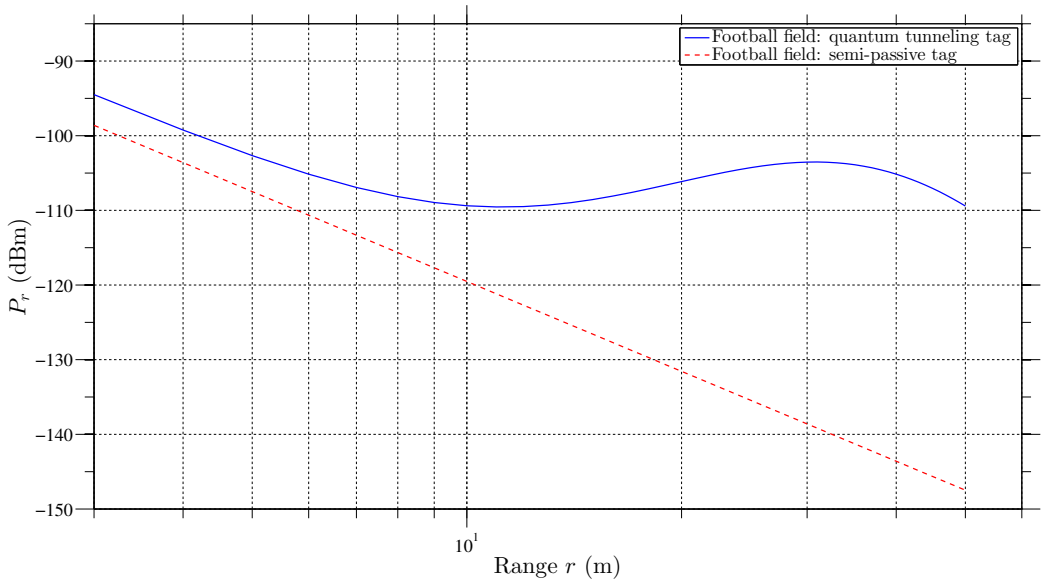

Figure 6.18: Comparing a 5.8 GHz backscattering link of 50 meter radius when an ideal semi-passive (M = 1) and a quantum tunneling tag ($M = G_{QTR}$) are used. Monostatic configuration, free space, and a -110 dBm receiving sensitivity are assumed.

whose omnidirectional properties would be preserved through a retrodirective structure.

Table 6.8: Required system parameters for the scenarios listed in Table 6.6 when using a 5.8 GHz monostatic transceiver

Location	EIRP (dBm)	P_T (dBm)	G_x (dBi)	G_t (dBi)
Town house (20 m)	-7.5	-11.5	4	1.8
Football field (50 m)	0.4	-11.5	11.9	1.8
Warehouse (100 m)	6.6	-11.5	18.1	1.8
Skyscraper (300 m)	16.2	-11.5	27.7	1.8
University Campus (700 m)	23.5	-11.5	35	1.8
Crop field (1 km)	21.8	-13.2	35	6
Airport (1.5 km)	22.5	-12.4	35	9
City (2 km)	23.5	-11.5	35	11

Figs. 6.18, 6.19, and 6.20 highlight the advantages of using a quantum tunneling tag ($M = G_{QTR}$) versus an ideal semi-passive tag (M = 1) for three free space scenarios (football field, university campus and city) when the backscattering link parameters of Table 6.8 and a transceiver with -110 dBm receiving sensitivity are used. As for the bistatic configuration cases, a range improvement of 1 order of magnitude can be observed.

The entire free space coverage of all listed scenarios is summarized in Fig. 6.21 for

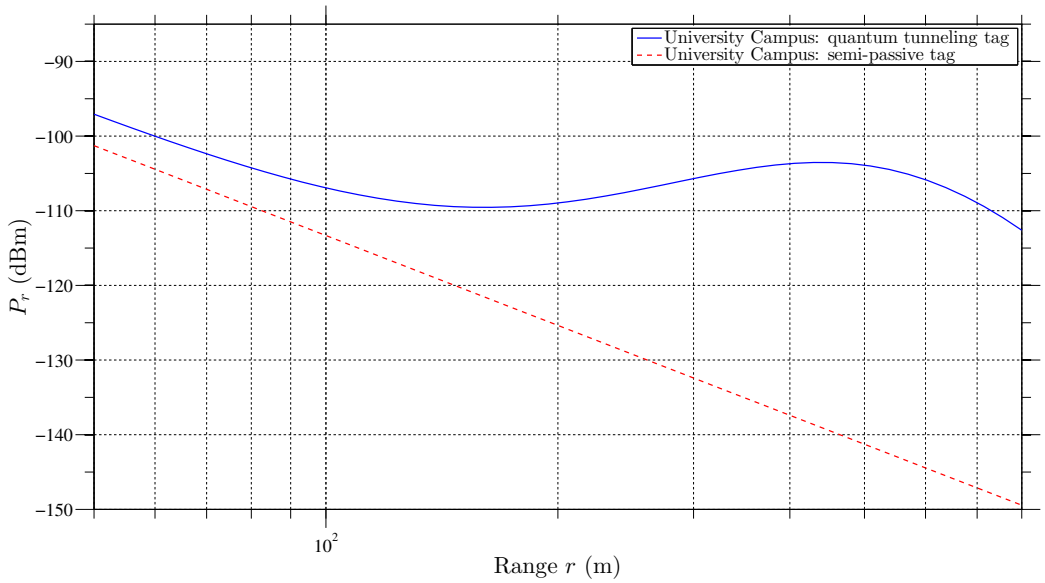

Figure 6.19: Comparing a 5.8 GHz backscattering link of 700 meter radius when an ideal semi-passive (M = 1) and a quantum tunneling tag ($M = G_{QTR}$) are used. Monostatic configuration, free space, and a -110 dBm receiving sensitivity are assumed.

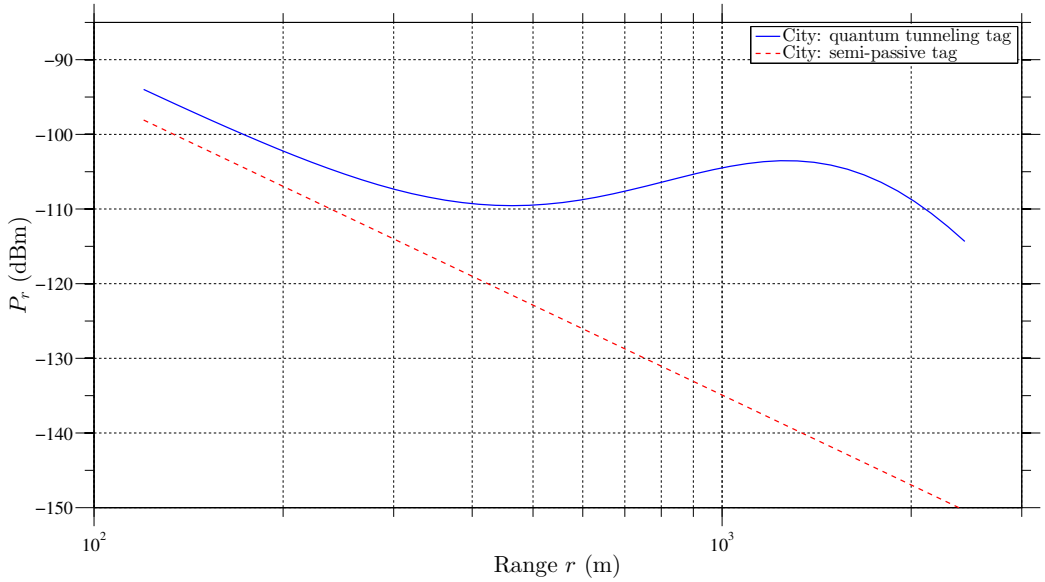

Figure 6.20: Comparing a 5.8 GHz backscattering link of 2000 meter radius when an ideal semi-passive (M = 1) and a quantum tunneling tag ($M = G_{QTR}$) are used. Monostatic configuration, free space, and a -110 dBm receiving sensitivity are assumed.

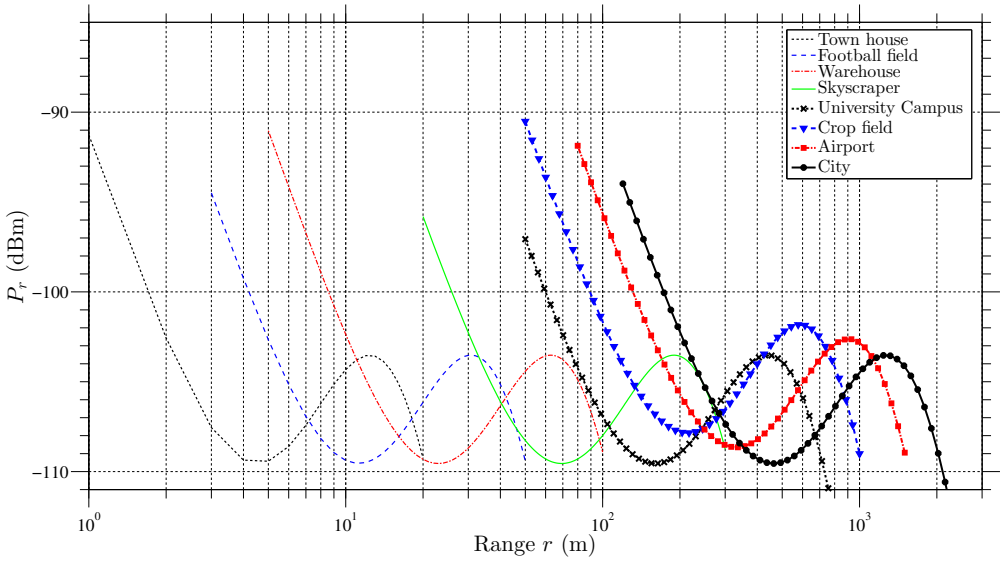

Figure 6.21: Whole coverage of different scenarios for the monostatic case, assuming free space and a -110 dBm receiving sensitivity.

monostatic transceiver configurations having a receiving sensitivity of -110 dBm. Also in this case, only distances at which correspond RF power levels on the QTT ranging between -55 dBm and -80 dBm were taken into account. Same as the bistatic case, a quantum tunneling tag allows a significant range extension in scenarios where the use of 5.8 GHz backscattering communication would not be otherwise possible.

6.7 Considerations on Power Consumption

The quantum tunneling tag prototype here presented requires a certain biasing power to properly work. This requirement does not identify the QTT as a passive transponder; nevertheless the required power is extremely small when compared to any other state-of-the-art RF wireless device. Hence, a passive QTT can be developed by adding a wireless energy harvesting module.

The required optimal biasing voltage (V_{DC} = 60 mV, I_{DC} = 340 μA) corresponds a total power of only 20.4 μW that could be easily collected through wireless power harvesting techniques. Moreover, since the modulation takes place by turning on and off the quantum

tunneling reflector, only a fraction of this power is really used. Finally, since high modulation speeds are possible (as shown in Chapter 5), the energy per bit requirements are much lower than any other currently available technology: a modulating frequency f_m of 250 kHz and 7 MHz require ($E = \frac{V_{DC} I_{DC}}{f_m}$) 81.2 μJ/bit and 2.9 pJ/bit, respectively.

Benefits for using a quantum tunneling tag are also shared by the transceiver units. Thanks to the high sensitivity of the device, low impinging RF power levels are enough to obtain backscattering modulation and amplification. The FCC regulations allow up to 36 dBm (4 W) EIRP for backscattering transceivers; nevertheless, the long range experimental results shown in this chapter have been obtained for transmitting EIRP as low as 6 dBm (4 mW) and the highest range of 1.2 km was achieved by transmitting only 28 dBm (0.6 W) EIRP.

The low powers required by the quantum tunneling tag will have several benefits for a future with billions of wireless connected devices from both an economical and environmental point of view.

6.8 Chapter Conclusions

A low powered backscattering communication link has been achieved at 1.2 km. The extensive measurements campaign allowed to: 1) validate the potential of a quantum tunneling tag in terms of low power requirements and long communication ranges; 2) achieve long communication ranges through backscattering modulation; 3) evaluate the quantum tunneling gains; and 4) foresee a set of possible scenarios that would benefit from the use of a QTT (such as office buildings, university campuses and cities). The examples provided have shown the possibility of increasing the backscattering range of a 5.8 GHz RFID tag by a factor of 10 when compared to an ideal semi-passive tag.

CHAPTER 7
CONCLUSION AND FUTURE WORK

7.1 Major Contributions

This dissertation has presented a low powered quantum tunneling tag achieving long range backscattering communications at 5.8 GHz. The RFID tag prototype has a sensitivity of -84 dBm and achieved the experimental backscattering range of 1.2 km. The measurement campaign held at and nearby the Georgia Tech campus allowed to collect enough data to model the quantum tunneling tag gain as a function of the impinging RF power. Through this model we have provided a tool to assist system engineers to design future long range backscattering systems. Examples of free space scenarios have shown the possibility of covering wide areas by simply using dipole or patch antennas, and the backscattering range of a 5.8 GHz RFID tag was increased by a factor of 10 when compared to an ideal semi-passive tag.

The required biasing powers of only 20.4 μW will widely contribute in the reduction of power consumption that is currently drastically affecting the expansion of pervasive wireless nodes. Modulation at 1 MHz was tested and modulations as fast at 7 MHz are possible. The low power requirements and the high modulation speeds allow an energy consumption of only 2.9 pJ/bit, 3 order of magnitude less than Bluetooth Low Energy. Finally, despite the non-linearity of tunnel diodes, the measured SNRs show a linear trend for increasing RF impinging powers. Because of its simple structure (p^+n^+), a tunnel diode can be easily manufactured by tweaking the fabrication process used for PN diode technologies and its production should be possible in the same foundries.

In Chapter 1, the problem was formulated. In Chapter 2, a solution to the limited range of backscattering systems was identified in the exploitation of the quantum tunneling effect

of some electronic devices. In Chapter 3 the quantum tunneling effect was analyzed and a state-of-the-art of the current reflection amplifier technology provided. The performances of a fabricated quantum tunneling reflector are reported in Chapter 4 and a study of the signal-to-noise ratio is outlined in Chapter 5. Finally, Chapter 6 provides the experimental results of a long range wireless backscattering link. It shows that 1.2 km ranges are achievable for extremely low biasing powers (20 μW) and for RF transmitting powers (4 mW) 1000 times lower than the power levels allowed by the FCC[1]. A 5.8 GHz backscattering link based on quantum tunneling tag performed 10 times better that a link using an ideal semi-passive tag. Considerations on the quantum tunneling tag gain, its power consumptions and use-case scenarios are also provided in this chapter.

To summarize, the original contributions of this thesis are:

- a state-of-the-art on reflection amplifiers;
- simulation and realization of two quantum tunneling reflector prototypes;
- characterization and performance analysis of the two prototypes;
- a study on the SNR of a quantum tunneling reflector;
- demonstration, for the first time, of a working long range backscattering transponder at 5.8 GHz;
- a 10 fold improvement of a 5.8 GHz backscattering link based on quantum tunnling tag when compared to a link using a semi-passive tag;
- collection of experimental results made publicly available for the research community;
- modelling of a quantum tunneling tag gain;

[1] 4 W is the maximum allowed EIRP

- development of a tool to assist system designers in setting up a long range backscattering communication link;

7.2 Future Work

This thesis lays out the basis for abundant future work that could branch out both in entrepreneurial and research activities. It shows potential for the development of a new microwave backscattering consumer product and for the dissemination of numerous research papers.

Several research activities can be undertaken; among them:

- design a quantum tunneling reflector where phase and magnitude of one or more tunnel diodes can be controlled independently to implement QAM modulation;
- make a power efficiency study of the quantum tunneling reflector to maximize the achievable reflective gains;
- combine the quantum tunneling reflector capabilities with a retro-directive antenna to further enhance the tag performances;
- develop a passive quantum tunneling tag that relays on wireless energy harvesting module to power up its RF front-end;
- design a 915 MHz quantum tunneling tag complaint with the current RFID Gen 2 standard.

7.3 Publications and Presentations

Much of the research presented in this dissertation has been published in, presented at, or submitted to refereed journals and conferences. The papers listed below are related to the research in this dissertation and include work from the authors research and MS degree.

7.3.1 Journals

- F. Amato, Peterson C. W., Akbar M. B., and Durgin G.D., "Quantum-Tunneling RFID Tags for Long-Range and Low-Power Microwave Applications," *IEEE Transactions of Microwave Theory and Techniques* (Accepted)

- F. Amato, H. M. Torun and G.D. Durgin, "A Designer Tool for the RFID System Engineer of the Future" *IEEE Transactions on Wireless Communications* (Under preparation)

7.3.2 Book Chapter

- G. Marrocco, C. Occhiuzzi, and F. Amato, "Sensor-Oriented Passive RFID," *The Internet of Things*, 2010

7.3.3 Conference Papers and Presentations

- F. Amato, H. M. Torun, and G. D. Durgin, "Beyond the Limits of Classic Backscattering Communications: a Quantum Tunneling RFID Tag," *IEEE International Conference on RFID, 2017* (submitted).

- F. Amato and G. D. Durgin, "Signal-to-Noise Ratio Measurements for IoT Communications Using Tunneling Reflectors," *IEEE 3rd World Forum on IoT*, Washington D. C., December 2016.

- M. B. Akbar, F. Amato, A. Classen, and G. D. Durgin, "Broadband Backscatter Based Technique to Identify the Presence of Skimming Electronics on Payment Terminals", *IEEE Radio and Wireless Symposium*, Austin, TX, January 2016, pp. 141-144.

- F. Amato, C. M. Beaulieu, A. T. Haile, J. Liang, K. M. Mairena, H. Murali, G. O. Udeochu, I. C. Uzoije, P. J. Wolfe, and G. D. Durgin, "5.8 GHz Energy Harvesting of

Space Based Solar Power Using Inkjet Printed Circuits on a Transparent Substrate," *2015 IEEE International Conference on Wireless for Space and Extreme Environments WiSEE*, Orlando, FL, December 2015, pp. 1-3.

- F. Amato, C. W. Peterson, M. B. Akbar, and G. D. Durgin, "Long Range and Low Powered RFID Tags with Tunnel Diode," *IEEE International Conference on RFID-Technologies and Applications (RFID-TA),* Tokyo, Japan, September 2015, pp. 182-187 **Best Paper Award**.

- M. B. Akbar, F. Amato, G. D. Durgin, G. Pisharody, and S-Y. Suh, "RFID Tag Load Impedance Measurement Using Backscattered Signal," *2015 IEEE International Symposium on Antennas and Propagation USNC/URSI National Radio Science Meeting,* Vancouver, Canada, July 2015, pp. 1762-1763.

- F. Amato, C. W. Peterson, B. P. Degnan, and G. D. Durgin, "A 45 μW Bias Power; 34 dB Gain Reflection Amplifier Exploiting the Tunneling Effect for RFID Applications," *IEEE International Conference on RFID (RFID),* San Diego, CA, April 2015, pp. 137-144.

- J. Grotz, A. Braun-Lois, T. Coutelier, E. Guedin, F. Amato, T. Abraham, D. Roche, K. Kegel, D. H. Caner, F. Roelens, and E. van der Wal, "Multi Input LNB-Demonstrator of a Reflector Feed Array Receiver for Satellite Broadcast Reception," *34th ESA Antenna Workshop and 2nd Evolutions in Satellite Telecommunication Ground Segments Workshop on Satcom User Terminal Antennas,*, October 2012.

- G. Marrocco, and F. Amato, "Self-sensing Passive RFID: From Theory to Tag Design and Experimentation," *IEEE European Microwave Conference; EuMC,* Roma, Italy, September 2009, pp. 1-4.

7.3.4 Poster Presentations

- F. Amato, C. W. Peterson, B. P. Degnan, and G. D. Durgin, "A 45 μW Bias Power; 34 dB Gain Reflection Amplifier Exploiting the Tunneling Effect for RFID Applications," *IEEE International Conference on RFID (RFID),* San Diego, CA, April 2015.

- F. Amato, C. W. Peterson, M. B. Akbar, and G. D. Durgin, "Long Range and Low Powered RFID Tags with Tunnel Diode," *IEEE International Conference on RFID-Technologies and Applications (RFID-TA),* Tokyo, Japan, September 2015.

- F. Amato, C. W. Peterson, B. R. Marshall, and M. M. Morys, "Reflective Sensing with Tunnel Diodes Exploiting Tunneling Effect," *Career; Research; Innovation and Development Conference (CRIDC)*, March 2015 **(Research Travel Grant Award)**.

- F. Amato F. and S. P. Rodrigues, "The Engineering Club; a Project Based Learning Experience at Meadowcreek High School", *Celebrating Teaching Day at Georgia Tech*, March 2015.

- F. Amato and G. D. Durgin, "A Tunnel Diode Reflection Amplifier for RFID Antennas," *IEEE International Conference on RFID*, April 2013.

7.3.5 Master Thesis

- F. Amato, "Setup Sperimentale per la Caratterizzazione di Radio Sensori RFID", *Master Thesis*.

7.3.6 Technical Reports

- M.B. Akbar, F. Amato, and G.D. Durgin, "Electromagnetic Integrity and Security Assay (ELISA)" *Georgia Tech and NCR Corporation*, May 2015.

- M.B. Akbar, F. Amato, and G.D. Durgin, "Intel RFID Toll Tag Project: Phase I Final Report", *Georgia Tech and Intel Corporation*, May 2014.

Appendices

APPENDIX A

CONTENT OF THE GITHUB REPOSITORY

The **.bin* data discussed in Chapter 6 have been acquired during the measurement campaign held at the Georgia Institute of Technology during the Fall 2016 semester. They are publicly available on the Github repository [67]. For questions and assistance please send an email to: f.amato@gatech.edu.

Several experimental setups and settings have been used:

- Setup I: Transmitted power: P_T = 0 dBm; transmitting antenna gain: G_{tx} = 6 dBi; receiving antenna gain: G_{rx} = 24 dBi QTT antenna gain: G_t = 6 dBi; receiver gain: G_{LNA} = 15 dB; cable losses L_1 = 1.2 dB and L_2 = 0.9 dB;
- Setup II: Transmitted power: P_T = 22 dBm; transmitting antenna gain: G_{tx} = 6 dBi; receiving antenna gain: G_{rx} = 24 dBi QTT antenna gain: G_t = 6 dBi; receiver gain: G_{LNA} = 30 dB; cable losses L_1 = 1.2 dB and L_2 = 0.9 dB;
- Setup III: Transmitted power: P_T = 22 dBm; transmitting antenna gain: G_{tx} = 6 dBi; receiving antenna gain: G_{rx} = 24 dBi QTT antenna gain: G_t = 24 dBi; receiver gain: G_{LNA} = 30 dB; cable losses L_1 = 1.2 dB and L_2 = 0.9 dB.

The repository has the following folders:

- 25TO50m: this folder contains all the **.bin* files directly acquired from the transceiver (Setup I) during the field measurements held on the Van Leer rooftop at the Georgia Institute of Technology the 19th of October 2016. The **.m* files to process and plot these data are also located here. The file names structure is the following: distance_bias_modulation.bin. For example, the wireless measurement taken at 45 meters away from the reader with the QTT being biased at 62 mV and modulated at 250 kHz is saved as 45m_62mv_250khz.bin;

- 70TO160m: this folder contains all the ***.bin** files directly acquired from the transceiver (Setup I) during the field measurements held on the Tech Green at the Georgia Institute of Technology the 20th of October 2016. The file names structure is the following: distance_bias_modulation.bin. For example, the wireless measurement taken at 70 meters away from the reader with the QTT being biased at 60 mV and modulated at 1 MHz is saved as 70m_60mv_1Mhz.bin;

- 650m: this folder contains all the ***.bin** files directly acquired from the transceiver (Setup II) during the field measurements held on the Georgia Tech Professional Education (GTPE) parking lot the 2nd of November 2016;

- 1200m: this folder contains all the ***.bin** files directly acquired from the transceiver (Setup III) during the field measurements held at the Viewpoint building in Midtown the 16th of November 2016.

- design_tool: this folder contains the **.m* file usable as tool to assist a system engineer to design a long range low powered backscattering system based on quantum tunneling tags.

APPENDIX B
MAGNETRON

The use of a 5.8 GHz magnetron was forecast to run long range backscattering tests involving above-100 m distances between a transceiver and a backscattering transponder. Nevertheless, due to the high sensitivities of the quantum tunneling tag, the 700 W 5.8 GHz CW generated by the magnetron system has not been necessary. Moreover, the signal spectrum of the assembled magnetron resulted to be noisy and not currently appropriate for the envisioned backscattering experiments.

The magnetron system has been used to conduct experimental work in microwave wireless harvesting techniques. This appendix summarizes the knowledge acquired about the system during its assembly phase and it is meant to be an useful reference for future system upgrades.

B.1 Magnetron Transmitter for Backscattering Applications

The assembled high power magnetron is shown in Fig. B.1. It has been assembled at the Propagation Group Laboratory at Georgia Institute of Technology; it consists of the following elements:

- CM358F (Tab. B.1);
- Filament transformer FIL35F;
- Magnetron head M5801;
- WR159 waveguide (4.9 GHz to 7.05 GHz) with CPR flanges;
- E-plane elbow with CPR to CMR-159 flanges;

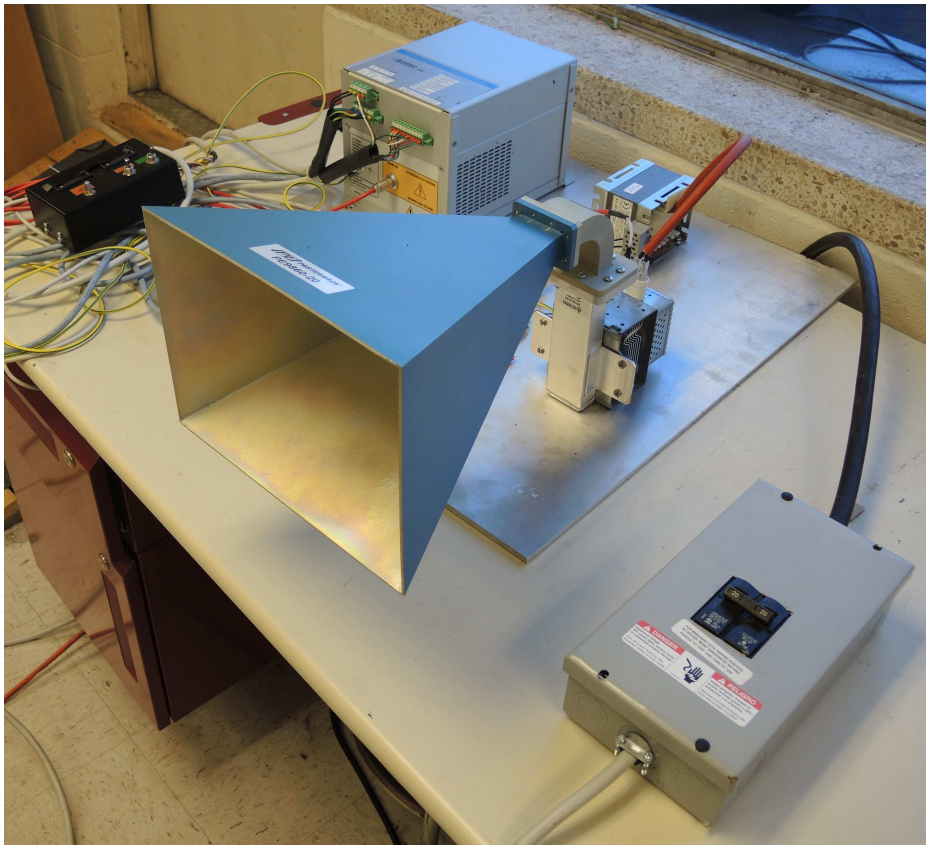

Figure B.1: The high power 5.8 GHz magnetron system.

- Control box;
- Horn antenna PE9860-20, 20 dBi gain (with CMR-159 flange);
- Horn antenna PE0860-15, 15 dBi gain (with CMR-159 flange);
- Circuit breaker;
- NEMA-L15-20 connector;
- Metal plate (ground plane);

B.1.1 The CM358F

The entire measurement system is controlled by the CM358 that, through three different connectors, is interfaced respectively with the power supply, a control box and the filament transformer. The CM358 is also equipped with an output port providing high voltage power (4 kV) to the magnetron filament. It is in charge of different functions such as: monitoring the magnetron temperature, cutting out the power in case of malfunction and displaying alarms by means of LEDs. The CM358 also provides a internal analog signal of 10 V that is used in this setup to regulate the magnetron output power through the use of the control box. Once powered by 230 V coming through the circuit breaker, the CM358 starts a 14 seconds internal timer to allow the preheating of the magnetrons filament.

B.1.2 The Filament Transformer

The filament transformer (Fig. B.2a) is used to power up the magnetron head; the primary receives a variable tension from the CM358 ranging between 100 and 200 V; the secondary is connected to the magnetron fast-ons and feeds the filament with a tension going from 4 V to 0 V. The maximum tension of the secondary corresponds to the stand-by state of the magnetron during which the filament is ready, but the magnetron does not emit any microwave energy yet. Once the emission of microwave energy is requested through the

Table B.1: CM358F parameters

Input voltage	230 Vac
Absolute max input voltage	265 Vac
Line frequency	50/60 Hz
RMS current (at 230 Vac)	9 A
Average current (@ 230 Vac)	6 A
Power factor	0.66
Output power	1300 W
Max output current at $40°$ C	300 mA
Filament preheating delay	14 s
Analog reference signal	10 V
Measuring output current signal	1 V = 100 mA (Z = 250 Ω)
Transient over-voltage	

control box, the CM358 controls the transformer with a *fold back curve* through which the filament tension is slowly reduced until it reaches 0 V.

B.1.3 The Magnetron Head

The secondary output of the filament transformer is connected to the male fast-ons of the magnetron. One of them is also connected to the high tension cable coming directly from the CM358F; by doing this, the magnetron will be fed at low tension among its ends, but will be at high potential respect to ground (about 4500 V). The CM358F is designed so that the magnetron has no duty cycle; in fact its output is a continuous microwave signal at 5.8 GHz. The amount of output power is regulated through the control box.

B.1.4 The Control Box

The control box has two safety switches, a nob and two displays. The switches turn the magnetron on and activate the *fold back curve procedure* that allows the CM358F to warm up the filament through the transformer. The nob is used to control the anodic current that regulates the output power of the magnetron. The two displays measure respectively the *control voltage*, used to regulate the magnetron output power, and the *output voltage*, indicating the amount of power being transmitted.

B.1.5 The Circuit Breaker

The circuit breaker connects the whole system to the power plug (NEMA-L15-20). The plug provides three phases and a neutral. Each phase corresponds to 120 V. As shown in Fig. B.2b, two phases (black and red cable in the figure) are connected together to obtain the 240 Vac necessary to power up the CM358F, the neutral (yellow cable) is short circuited to ground and the third phase (green cable) is left unconnected and covered with a plastic cap for safety reasons. Cable 1 and 2 of connector #3 from the CM358F reach the circuit breaker.

B.2 Regulatory Considerations

The magnetron system is meant to be used outdoor to radiate receiving antennas at 100 m distance from it. Since humans could accidentally be hit by the magnetron radiated power, a study has been held to validate the safety of the operations.

FCC regulations ([71], table B, page 72) do not state any limits to the electric and magnetic field strengths in the frequency range 1.5 - 100 GHz, but, they specify that, for uncontrolled population, the exposure to the power density, S, should not exceed 1.0 mW per cm^2 and the time of exposure should be less than 30 minutes. The power density is expressed as:

$$S = \frac{\mathcal{E}^2}{3770} \qquad \frac{mW}{cm^2}; \tag{B.1}$$

with $\mathcal{E}$ being the electric field strength expressed in V/m.

The magnetron system transmits 700 W of peak power and it is connected to a 20 dBi horn antenna therefore, the maximum average power density at 100 meters of distance from the magnetron is:

$$|S(r,\phi,\theta)| = \frac{D(\theta,\phi)P_T}{4\pi r^2} = \frac{10^2 700^3}{4\pi 10000^4} = 0.557 \quad .\frac{mW}{cm^2} \tag{B.2}$$

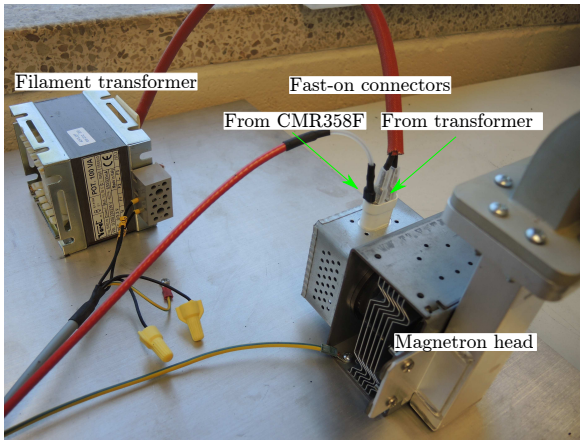

(a)

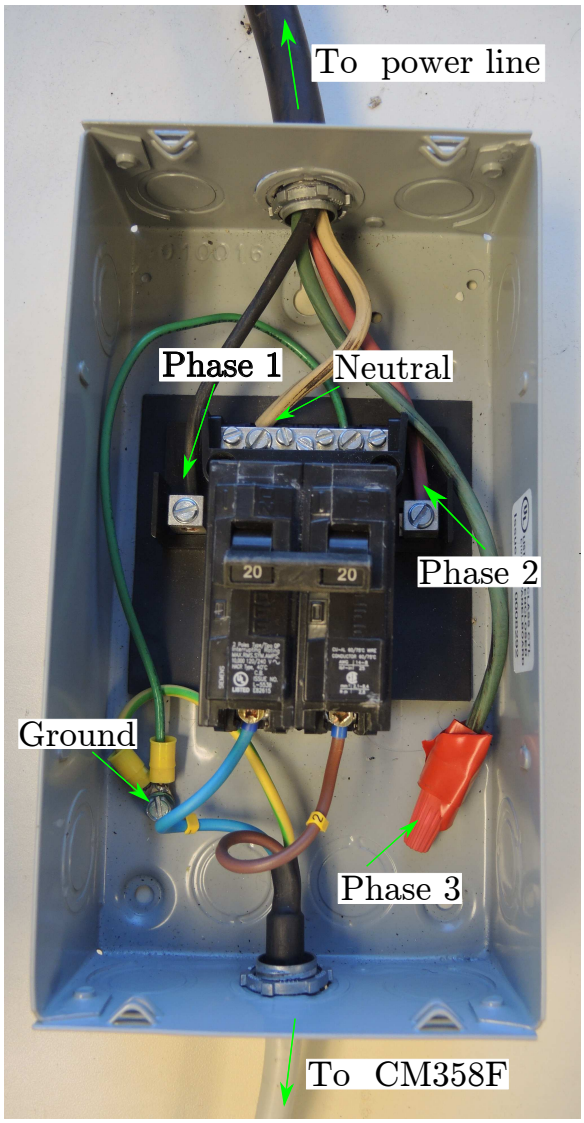

(b)

Figure B.2: a) the filament transformer and the fast-on connectors; b) the circuit breaker.

By being less than 1.0 mW per cm^2, the long range measurements do not exceed the FCC regulations.

REFERENCES

[1] IDC, *Intel*, United Nations.

[2] McKinsey Global Institute, "Strategy analytics M2M strategies advisory service," NYTimes.com.

[3] ATMEL, *Samb11*. [Online]. Available: http://www.atmel.com/Images/Atmel-42426-SmartConnect-SAMB11-SOC_Datasheet.pdf (visited on 12/20/2016).

[4] Empire State Realty Trust, *Empire State building fact sheet*. [Online]. Available: http://www.esbnyc.com/sites/default/files/esb_fact_sheet_4_9_14_4.pdf (visited on 12/20/2016).

[5] Y. Zeng, P. H. Pathak, and P. Mohapatra, "A first look at 802.11ac in action: Energy efficiency and interference characterization," in *2014 IFIP Networking Conference*, Jun. 2014, pp. 1–9.

[6] LoRa Alliance, *LoRa Alliance, Wide Area Networks for IoT*. [Online]. Available: https://www.lora-alliance.org/ (visited on 12/20/2016).

[7] TriQuint, *TQL9066*. [Online]. Available: http://www.triquint.com/products/p/TQL9066 (visited on 12/20/2016).

[8] Analog Devices, *HMC902*. [Online]. Available: http://www.analog.com/media/en/technical-documentation/data-sheets/hmc902.pdf (visited on 12/20/2016).

[9] TriQuint, *TQP369180*. [Online]. Available: http://www.triquint.com/products/p/TQP369180 (visited on 12/20/2016).

[10] Analog Devices, *HMC415*. [Online]. Available: http://www.analog.com/media/en/technical-documentation/data-sheets/hmc415.pdf (visited on 12/20/2016).

[11] Anadigics, *AWL9581*. [Online]. Available: http://www.admiral-microwaves.co.uk/pdf/anadigics/AWL9581_Rev_2.1.pdf (visited on 12/20/2016).

[12] K. Smiljkovikj and L. Gavrilovska, "Wireless personal communications," 2014.

[13] *Smart agriculture project in Galicia to monitor vineyards with Waspmote*. [Online]. Available: http://www.libelium.com/smart_agriculture_vineyard_sensors_waspmote (visited on 12/20/2016).

[14] Impinj, *Monza R6 RFID tag chip*. [Online]. Available: http://www.impinj.com/products/tag-chips/monza-r6/ (visited on 12/20/2016).

[15] S. J. Thomas, E. Wheeler, J. Teizer, and M. S. Reynolds, "Quadrature amplitude modulated backscatter in passive and semipassive uhf rfid systems," *IEEE Transactions on Microwave Theory and Techniques*, vol. 60, no. 4, pp. 1175–1182, Apr. 2012.

[16] D. Miorandi, S. Sicari, F. De Pellegrini, and I. Chlamtac, "Internet of things: Vision, applications and research challenges," *Ad Hoc Netw.*, vol. 10, pp. 1497–1516, 2012.

[17] J. F. Ensworth and M. S. Reynolds, "Every smart phone is a backscatter reader: Modulated backscatter compatibility with bluetooth 4.0 low energy (ble) devices," in *2015 IEEE International Conference on RFID (RFID)*, Apr. 2015, pp. 78–85.

[18] J. Griffin and G. Durgin, "Complete link budgets for backscatter-radio and RFID systems," *Antennas and Propag. Magazine, IEEE*, vol. 51, no. 2, pp. 11–25, Apr. 2009.

[19] C. A. Balanis, *Antenna Theory: Analysis and Design*, 2nd Ed. New York: Wiley, 1997.

[20] P. V. Nikitin and K. V. S. Rao, "Performance limitations of passive uhf rfid systems," in *2006 IEEE Antennas and Propagation Society International Symposium*, Jul. 2006, pp. 1011–1014.

[21] S. Hemour and K. Wu, "Radio-frequency rectifier for electromagnetic energy harvesting: Development path and future outlook," *Proc. of the IEEE*, vol. 102, no. 11, pp. 1667–1691, Nov. 2014.

[22] "IEEE standard for definitions of terms for antennas," *IEEE Std 145-2013 (Revision of IEEE Std 145-1993)*, pp. 1–50, Mar. 2014. DOI: 10.1109/IEEESTD.2014.6758443.

[23] U.S. government publishing office, "Code of federal regulations," *FCC regulations, Title 47, Chapter 1, subchapter A*, vol. Part 15, Subpart C, no. 2, par.15.247, Oct. 2014.

[24] Motorola, *Zebra fx9500 fixed RFID reader*. [Online]. Available: https://www.zebra.com/us/en/products/spec-sheets-latest/rfid/rfid-readers/fx9500-spec-sheet-en.html (visited on 12/20/2016).

[25] J. T. Prothro and G. D. Durgin, "Improved performance of a radio frequency identification tag antenna on a metal ground plane," Master's thesis, Georgia Institute of Technology, Atlanta, 2007.

[26] P. V. Nikitin, K. V. S. Rao, and R. D. Martinez, "Differential rcs of rfid tag," *Electronics Letters*, vol. 43, no. 8, pp. 431–432, Apr. 2007.

[27] D. M. Pozar, *Microwave engineering*. New York: Wiley, 2011.

[28] F. Amato and G. D. Durgin, *A tunnel diode reflection amplifier for RFID antennas*, Poster presentation, Orlando FL, Apr. 2013.

[29] B. Smida and S. Islam, "Full-duplex wireless communication based on backscatter amplifier," in *Proc. IEEE Comm. Workshops (ICC) Int. Conf.*, Jun. 2014, pp. 91–95.

[30] K. Chang, *Microwave Solid-State Circuits and Applications*. John Wiley and Sons, 1994.

[31] W. T. Read, *A Proposed High-Frequency Negative Resistance Diode*. Bell System Technical Journal, Mar. 1958, vol. 37, pp. 401–446.

[32] R. L. Johnston, D. B. C. Jr., and C. B. G., *A Silicon Diode Microwave Oscillator*. Bell System Technical Journal, Feb. 1965, vol. 44, pp. 369–372.

[33] S. Chung, S. Chen, and Y. Lee, "Microwave oscillators of current in III-V semiconductors," *Solid-State Comm.*, vol. 1, pp. 89–91, Sep. 1963.

[34] B. K. Ridley and T. B. Watkins, "The possibility of negative resistance effects in semiconductors," *Proc. of the Physical Society*, vol. 78, no. 2, p. 293, 1961.

[35] C. Hilsum, "Transferred electron amplifiers and oscillators," *Proc. of the IRE*, vol. 50, no. 2, pp. 185–189, Feb. 1962.

[36] L. Esaki, "New phenomenon in narrow germanium p-n junctions," *Phys. Rev.*, vol. 109, pp. 603–604, 2. [Online]. Available: http://link.aps.org/doi/10.1103/PhysRev.109.603 (visited on 12/20/2016).

[37] ——, "Long journey into tunneling," *Proc. of the IEEE*, vol. 62, no. 6, pp. 825–831, Jun. 1974.

[38] A. Seabaugh, X. Deng, T. Blake, B. Brar, T. Broekaert, R. Lake, F. Morris, and G. Frazier, "Transistors and tunnel diodes for analog/mixed-signal circuits and embedded memory," in *Int. Tech. Digest Electron Devices Meeting*, Dec. 1998, pp. 429–432. DOI: 10.1109/IEDM.1998.746390.

[39] G. N. Roberts, "Tunnel diodes operation and application," *Electronic Tech.*, vol. 37, no. 6, pp. 217–222, Jun. 1960.

[40] H. S. and W. K., "Radio-frequency rectifier for electromagnetic energy harvesting: Development path and future outlook," *Proceedings of the IEEE*, vol. 102, no. 11, pp. 1667–1691, Nov. 2014.

[41] C. H. P. Lorenz, S. Hemour, W. Li, Y. Xie, J. Gauthier, P. Fay, and K. Wu, "Breaking the efficiency barrier for ambient microwave power harvesting with heterojunction backward tunnel diodes," *IEEE Transactions on Microwave Theory and Techniques*, vol. 63, no. 12, pp. 4544–4555, Dec. 2015. DOI: 10.1109/TMTT.2015.2495356.

[42] A. C. Seabaugh and Q. Zhang, "Low-voltage tunnel transistors for beyond cmos logic," *Proceedings of the IEEE*, vol. 98, no. 12, pp. 2095–2110, Dec. 2010.

[43] L. L. D. and L. E. M., *Quantum Mechanics*. Reading, Massachusetts: Addison-Wesley, 1958, 174.

[44] F. Amato, C. W. Peterson, M. Akbar, and G. Durgin, "Long range and low powered RFID tags with tunnel diode," in *Proc. IEEE Int. Conf. RFID-Tech. and Appl. (RFID-TA)*, Sep. 2015, pp. 137–144.

[45] F. Amato, C. Peterson, B. Degnan, and G. Durgin, "A 45 μW bias power, 34 dB gain reflection amplifier exploiting the tunneling effect for RFID applications," in *Proc. IEEE RFID Int. Conf.*, Apr. 2015, pp. 137–144.

[46] V. Vesterinen, J. Hassel, and H. Seppa, "Tunable impedance matching for josephson junction reflection amplifier," *IEEE Trans. Applied Superconductivity*, vol. 23, no. 3, pp. 1 500 104–1 500 104, Jun. 2013.

[47] J.-F. Bousquet, S. Magierowski, and G. Messier, "A 4-GHz active scatterer in 130-nm CMOS for phase sweep amplify-and-forward," *IEEE Trans. Circuits and Systems I: Regular Papers*, vol. 59, no. 3, pp. 529–540, Mar. 2012.

[48] J. Kimionis, A. Georgiadis, S. Kim, A. Collado, K. Niotaki, and M. Tentzeris, "An enhanced-range RFID tag using an ambient energy powered reflection amplifier," in *IEEE MTT-S Int. Microw. Symp. (IMS)*, Jun. 2014, pp. 1–4.

[49] P. Chan and V. Fusco, "Full duplex reflection amplifier tag," *IET Microw., Antennas Propag.*, vol. 7, no. 6, pp. 415–420, Apr. 2013.

[50] P. Chan and V. Fusco, "Bi-static 5.8 GHz RFID range enhancement using retrodirective techniques," in *IEEE Eur. Microw. Conf. (EuMC)*, Oct. 2011, pp. 976–979.

[51] G. Dalman, F. Zappert, and C. Lee, "Relaxing-avalanche-mode reflection amplifier," *Electronics Lett.*, vol. 8, no. 9, pp. 243–244, May 1972.

[52] A. Lazaro, A. Ramos, R. Villarino, and D. Girbau, "Time-domain UWB RFID tag based on reflection amplifier," *IEEE Antennas and Wireless Propag. Lett.*, vol. 12, pp. 520–523, 2013.

[53] H. Cantu, V. Fusco, and S. Simms, "Microwave reflection amplifier for detection and tagging applications," *IET Microw., Antennas Propag.*, vol. 2, no. 2, pp. 115–119, Mar. 2008.

[54] H. Cantu and V. Fusco, "A 21 GHz reflection amplifier MMIC for retro-directive antenna and RFID applications," in *Inst. of Engineering and Tech. Seminar MM-Wave Products Tech.*, Nov. 2006, pp. 66–70.

[55] S. Chung, S. Chen, and Y. Lee, "A novel bi-directional amplifier with applications in active van atta retrodirective arrays," *IEEE Trans. Microw. Theory Tech.*, vol. 51, no. 2, Feb. 2003.

[56] P. Gardner and D. Paul, "Aspects of the design of low noise, negative resistance, reflection mode transistor amplifiers," *IEEE Trans. Microw. Theory Tech.*, vol. 39, no. 11, pp. 1869–1875, Nov. 1991.

[57] S. Nicotra, "13 GHz FET negative resistance 0.5 W amplifier," in *IEEE Eur. Microw. Conf.*, Sep. 1979, pp. 303–307.

[58] M. McPhun, "U.H.F. tunnel-diode amplifier," *Inst. of Electrical Engineers*, vol. 114, no. 4, pp. 428–434, Apr. 1967.

[59] F. Amato, C. W. Peterson, M. Akbar, and G. Durgin, "Quantum-tunneling rfid tags for long-range and low-power microwave applications," *IEEE Transactions on Microwave Theory and Techniques*, 2017, accepted.

[60] R. Adler, "A study of locking phenomena in oscillators," *Proceedings of the IEEE*, vol. 61, no. 10, pp. 1380–1385, Oct. 1973. DOI: 10.1109/PROC.1973.9292.

[61] B. Razavi, "A study of injection locking and pulling in oscillators," *IEEE Journal of Solid-State Circuits*, vol. 39, no. 9, pp. 1415–1424, Sep. 2004. DOI: 10.1109/JSSC.2004.831608.

[62] RFMW, *Planar back (tunnel) diodes MBD series*. [Online]. Available: https://www.rfmw.com/ProductDetail/MBD5057E28-metelics/472882/ (visited on 12/20/2016).

[63] OshPark, *4 layer prototype service*. [Online]. Available: http://docs.oshpark.com/services/four-layer/ (visited on 12/20/2016).

[64] Isola, *FR408 high performance laminate and prepreg*, 2014 (Accessed July 26, 2016). [Online]. Available: http://docs.oshpark.com/resources/FR408-High-Performance-Laminate-and-Prepreg-Data-Sheet.pdf.

[65] F. Amato and G. D. Durgin, "Signal-to-Noise Ratio measurements for IoT communications with quantum tunneling reflectors," in *2016 IEEE World Forum on IoT*, Dec. 2016.

[66] F. Amato, H. M. Torun, and G. D. Durgin, "Beyond the limits of classic backscattering communications: A quantum tunneling RFID tag," in *IEEE International Conference on RFID*, submitted, 2017.

[67] F. Amato and H. M. Torun. (). 1kmRFID, [Online]. Available: https://github.com/francuz/1kmRFID (visited on 12/20/2016).

[68] J. Griffin, "High-frequency modulated-backscatter communication using multiple antennas," PhD thesis, Georgia Institute of Technology, Atlanta, 2009.

[69] Ettus Research, "USRP N200," [Online]. Available: https://www.ettus.com/product/details/UN200-KIT (visited on 12/20/2016).

[70] M. B. Akbar, M. M. Morys, and G. D Durgin, "FDI-embedded microwave RFID-based skimmer detection system," Georgia Institute of Technology, Atlanta, Tech. Rep., 2013.

[71] FCC. (Jun. 2016). Evaluating compliance with FCC guidelines for human exposure to radiofrequency electromagnetic fields, [Online]. Available: http://transition.fcc.gov/Bureaus/Engineering_Technology/Documents/bulletins/oet65/oet65.pdf (visited on 12/20/2016).

VITA

Francesco Amato received his his M.Sc. in Telecommunication Engineering from Tor Vergata University in February 2009 and his Ph.D degree in Electrical and Computer Engineering from the Georgia Institute of Technology in January 2017. In 2009 he started working at the satellite operator SES, Luxembourg, as ground system engineer. In 2012 he joined The Propagation Group at the Georgia Institute of Technology as Fulbright scholar.

He has been the recipient of numerous honors and awards including the 2015 *William Brown* fellowship, the 2015 RFID-TA best student paper award, the 2014 and 2013 *GoStem* fellowships, two *Georgia Tech Research and Innovation* graduate student awards and the Master thesis prize *Sebastiano e Rita Raeli* in 2009. While pursuing his doctorate degree he worked at Intel Labs in Santa Clara, California, during summer 2015 and was the instructor of record for ECE3710 during spring and summer 2016. He has been on the organizing committee for IEEE GLOBECOM in 2013 and for the IEEE international conference on RFID in 2017.

His research interests include wireless power transfer and energy harvesting, antenna design for RFID sensing, wireless channel modelling, nonlinear devices, and low-power microwave for enhancing backscattering communications.